THE UNIVERSITY OF CALGARY

Study of Bubble Flow in Gas-Solid Fluidized Beds

by

Fan Li

A THESIS

SUBMITTED TO THE FACULTY OF GRADUATE STUDIES

IN PARTIAL FULFILLMENT OF THE REQUIREMENTS FOR THE

DEGREE OF MASTER OF SCIENCE

DEPARTMENT OF CHEMICAL AND PETROLEUM ENGINEERING

CALGARY, ALBERTA

JUNE, 2000

0-612-55262-4

ABSTRACT

Studies on bubble size, velocity, flow pattern, occurrence frequency and volume fraction are important for modeling and design of fluidized beds. In this research work, experiments were carried out in a 10 cm diameter fluidized bed with a porous plate distributor. The particles used as solid phase include narrow size distribution polyethylene (NPE), wide size distribution polyethylene (WPE) and narrow size distribution sand (NS) particles. Air was the gas phase. A medical X-ray fluoroscopy system (GE MPX-100) was employed to capture the fluidized bed images at superficial gas velocities ranging from $1.5\times U_{mf}$ to $3.0\times U_{mf}$ for the three gas-solid systems. The images were video-recorded and used for digitizing and image processing. In order to determine the superficial gas velocities to be used for the imaging experiments, minimum fluidization measurements were also conducted for the three systems. To provide bubble flow information with good statistics, an image processing software package has been developed for analysis of the digitized images captured at 30 frames/s. In total, 12 image data sets were processed. Bubble diameter, vertical and horizontal velocity, occurrence frequency and bubble volume fraction were extracted. It was found that bubble size increases with increase in superficial gas velocity and bed height for all three gas-solid systems investigated. Bubble rising velocity increases slightly with an increase in superficial gas velocity and bed height. It was also observed that bubble flow is mainly around the centerline of the bed for NPE-air and WPE-air systems while it is distributed across the whole cross-section of the bed for the NS-air system. Asymmetric bubble flow was present in the column at low U/U_{mf}. Increased superficial gas velocity leads to increased bubble occurrence frequency and bubble volume fraction in the bed. A correlation for bubble diameter proposed by Mori and Wen (1975) and a correlation for bubble rising velocity proposed by Kunii and Levenspiel (1991) were employed to predict bubble diameter and rising velocity. It was found that the predicted bubble sizes by Mori and Wen's correlation are higher than those obtained from image processing in this work. Kunii and Levenspiel's correlation provides good prediction on bubble rising velocity on condition that the bubble size used in the correlation is properly estimated or measured.

ACKNOWLEDGMENTS

This thesis has benefited from the advice, encouragement and supplemental efforts of several individuals. The time is ripe for me to express my appreciation to these people.

I am thankful to Dr. Apostolos Kantzas for having initiated me into the fluidized bed research area and giving me the opportunity to come to the University of Calgary. As my supervisor his advice and support have enabled me to bring this research to its final form. My appreciation also goes to Dr. Caroline Hyndman for providing useful suggestions and support.

It would be no exaggeration if I say that I had a third supervisor in Dr. Doug Phillips. To him I owe much of what I learned especially in the area of image processing. I express my gratitude and appreciation to Dr. Phillips for his very helpful advice. The experimental work involved in this study could not be done by myself due to the complicated operation of the X-ray imaging system. I need to acknowledge Ms. Kelly Hamilton, a technologist in the TIPM lab for assistance in setting up the fluidized beds and operating the fluoroscopy system.

Over the past two years many people have been in and out of this department. I express my thanks to all my friends for making my presence here pleasant and enjoyable. Finally, I wish to express my thanks to my husband, Jinwen for his love and support through the ups and downs of the past two years. When things were not going well it was his words that provided solace. In addition, his suggestions have helped me a lot in this research work.

This work was supported by NOVA Chemicals and NSERC. Their financial support is gratefully acknowledged.

TABLE OF CONTENTS

LIST OF FIGURES

LIST OF TABLES

NOMENCLATURE

A	bed cross-sectional area, m^2
A_r	Archimedes Number (Kunii and Levenspiel, 1991), dimensionless
A_t	cross-sectional area of a bed, m^2
D	fluidized bed column diameter in L/D
d_b	bubble diameter in a fluidized bed, cm
d_{b0}	bubble diameter at distributor, cm or m
d_{bm}	the limiting size of bubble expected in a very deep bed, cm
$d_{b,eq}$	equilibrium bubble diameter, m
d_p	fluidized bed particle diameter, cm
d_t	fluidized bed diameter, cm
f_s^*	splitting frequency of a single bubble, 1/s
$f(x, y)$	two dimensional image light intensity function
$f'(r, \theta)$	two dimensional image light intensity function in polar coordinates
f	bubble occurrence frequency, 1/s
f_v	bubble volume fraction, dimensionless
g	gravity acceleration, m/s^2
$g(x, y)$	two dimensional image intensity function for smoothed image
h	fluidized bed height, cm
I	transmitted X-ray intensity
I_0	incident X-ray intensity
L	static fluidized bed height in L/D
L	path length, m
M	number of columns in an image frame
N	total number of new bubbles counted in image processing, number of rows in an image frame
N_0	number of orifices on distributor plate
N	number of frames tracked
r	frame rate (30 frames/s in this work)

$Re_{p,mf}$	particle Reynolds number, dimensionless
T	time period tracked, s
T0 (T0*)	transducer position
T1 (T1*)	transducer position
T2 (T2*)	transducer position
T3 (T3*)	transducer position
U	superficial gas velocity, cm/s
$\mathrm{U_{mf}}$	minimum fluidization velocity, cm/s
U	superficial gas velocity, cm/s
U_{mf}	minimum fluidization velocity, cm/s
U	superficial gas velocity, m/s
u_{mf}	minimum fluidization velocity, m/s
u_b	bubble rising velocity through a bed, m/s
u_{br}	bubble rising velocity with respect to the emulsion phase, m/s
V_{bubble}	total bubble volume in fluidized bed, cm^3
V_{bed}	the volume of fluidized bed in frames, cm^3
z	height above distributor, cm or m
z_0	height of initial bubble formation, m

Greek Symbols

α	parameter in Equation (2.13)
γ_M	parameter in Equation (2.8)
δ	parameter in Equation (2.7)
ε_g	gas voidage in the fluidized bed
η	parameter in Equation (2.7)
μ	attenuation coefficient of the material
ρ	density of the material, g/cm^3

Acronyms

CT	Computed Tomography
FCC	Fluid Catalytic Cracking

NPE	Narrow size distribution Polyethylene particles
NS	Narrow size distribution Sand particles
PSD	Particle Size Distribution
TV	Television
WPE	Wide size distribution Polyethylene particles
2-D	two dimensional
3-D	three dimensional

CHAPTER 1
INTRODUCTION

Gas-solid fluidized beds are preferred reactors for several processes in chemical industry. Gas phase characteristics in fluidized beds, such as bubble size, shape, bubble velocity, bubble flow pattern and bubble generation frequency, are the important factors in determining the behavior of a gas-solid fluidized bed. Therefore, measurement and prediction of bubble properties in fluidized beds have been a major research subject since the 1940's when the fluid catalytic cracking (FCC) process was first introduced. Earlier research work focused on fluidization characteristics of fine particles with mean diameter of about 100 μm, such as those used in the FCC process. Later on, studies were extended to coarser materials such as sand and glass powders. However, not many studies on light coarser particles for polymerization have been reported in open literature.

The first theory to interpret the gas phase flow in a fluidized bed, which is still widely used today, is called the "two-phase" theory proposed by Toomey and Johnstone (1952). It is assumed that once the velocity of gas flowing through a bed of powder exceeds the minimum velocity needed to just fluidize the bed, any excess flow passes through the bed in the form of gas bubbles which behave in a manner similar to air bubbles rising through a column of water. It is those bubbles in fluidized beds that are responsible for many of the advantages and disadvantages of fluid bed operation. The high degree of mixing of the bed solids is found to be the result of the vertical movement of particles carried in the wake region behind bubbles. This gives rise to the excellent heat transfer properties of the bed. On the other hand, gas flowing inside bubbles is found to have little contact with the bed solids, and this bypassing effect in some cases severely limits the extent of the gas - solid reaction that could be achieved.

The first satisfactory theory of bubble motion in fluidized beds was proposed by Davidson (1961) and was later developed by Davidson and Harrison (1963), Jackson (1963a, b), Murray (1965a, b) and others. The Davidson theory has been described as "the important concept that guided research and advanced understanding of dense bubbling fluidized beds" (Kunii and Levenspiel, 1991). It led to the development of many diverse experimental techniques, which were designed to probe the properties and behavior of bubbles and to study the effects resulting from their flow.

The second generalization of considerable utility was introduced by Geldart (1973), in which he separated fluidized solids into four groups, A, B, C, and D, according to the size and density of their component particles. Group A particles are materials such as the FCC catalyst, having a small mean particle size and low particle density (<1.4 g/cm^3). These solids fluidize easily, with smooth fluidization at low gas velocity and controlled bubbling with small bubbles at higher gas velocities. Group B particles, such as coarse sand, form bubbles as soon as the minimum fluidization velocity, U_{mf} is exceeded. Solids of group C are very fine powders. Normal fluidization is extremely difficult for these solids because inter-particle forces are greater than those resulting from the action of gas. They are cohesive materials such as starch, flour and cement. Group D particles are large and dense and prone to spouting rather than fluidizing. Geldart's classification is easy to use and is readily displayed in Figure 1.1 (Kunii and Levenspiel, 1991) for air fluidization at ambient conditions and for superficial gas velocity, U, less than about $10\times U_{mf}$. For any solid of known density ρ_s and mean particle size $\bar{d}_p$, this graph shows the type of fluidization to be expected.

Due to the fact that bubbles inside a 3-D cylindrical fluidized bed are not directly observable, early experimental studies on gas phase dynamics in fluidized beds were mostly conducted in beds which are constructed from two flat parallel-sided transparent plates separated by a small distance (about 1 cm) (Rowe, 1971). Bubbles rising through

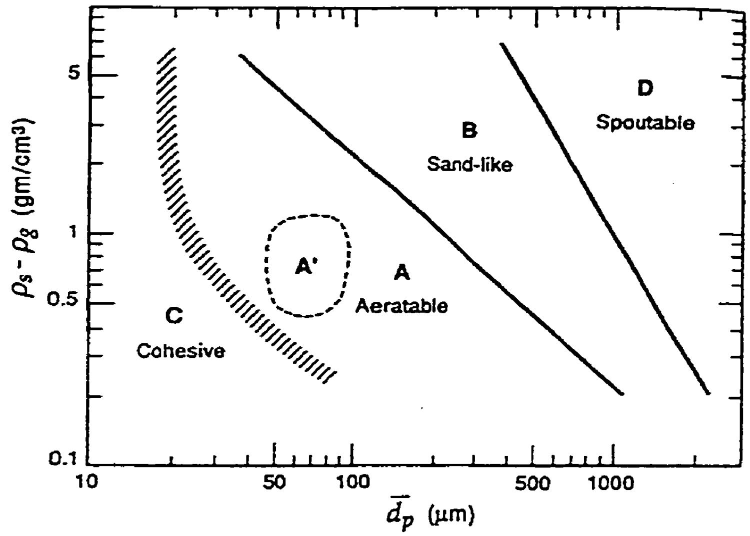

Figure 1.1. The Geldart classification of particles for air at ambient conditions (Kunii and Levenspiel, 1991)

such beds rapidly grow big enough through coalescence to span the distance between the plates and become visible to naked eyes. Beds with such configuration are called "two dimensional beds" or "2-D beds" although they represent a vertical slice through a truly 3-D system. Ciné photography or video imaging may be used to record the flow of bubbles and the images obtained can be analyzed to give quantitative information on bubble dynamics. A recent application of such a system was reported by Hailu *et al.* (1993) to measure bubble rising velocity in fluidized beds.

Despite the usefulness of 2-D fluidized beds, there is always an argument as to whether the behavior observed in 2-D beds can be directly extrapolated to 3-D beds. Therefore, a number of techniques and methods have been developed to deal with gas flow in real 3-D systems which will be discussed in detail in the following chapter.

In previous studies, bubble dynamic information in 2-D and 3-D fluidized beds was obtained by analyzing very limited numbers of bubbles because data analysis and image processing were mostly manually conducted, which is time and labor consuming. It is quite questionable whether the bubble properties obtained this way are statistically representative. Therefore, not only bubble dynamic properties with good statistics (the number of bubbles is large enough) are important and essential, but software that can automatically process bubble images to get these properties is necessary to obtain the reliable bubble flow information in fluidized beds. In addition, studies on fluidized beds with polyethylene-air system have not been found in open literature. Therefore, such a study on this system is of interest to the research area of bubble flow in fluidized beds.

This study will focus on investigating bubble size, bubble velocity, bubble flow pattern, bubble occurrence frequency and bubble volume fraction in a 3-D fluidized bed to provide detailed statistically representative information on bubble dynamics with polyethylene as the solid phase and air as the gas phase. For comparison, a study on sand particles and air system is also necessary. In addition, a computer software package was developed for automatic on-line image processing to extract the bubble dynamic information from the images recorded with an X-ray imaging system.

CHAPTER 2
LITERATURE REVIEW

The techniques available for measuring bubble dynamic properties in 3-D fluidized beds may be divided into two broad groups. One is the use of various types of probes immersed in the bed, and the other is based on non-invasive measurements such as X-ray or γ-ray attenuation and capacitance imaging. Although probe-based methods are generally cheaper and more convenient there is always some uncertainty about the extent to which immersed objects influence the hydrodynamics of fluidized beds (Rowe and Masson, 1981) so that despite their drawbacks, the non-invasive techniques are to be preferred for the accurate measurement of fluidized beds. Of the three non-invasive methods mentioned above, γ-ray attenuation is limited to producing time-averaged tomographic images (Simons *et al.* 1993). Operated in the pulsed mode both X-ray attenuation and capacitance imaging are capable of producing real-time speed values of bubble size, velocities, frequency and bubble volume fractions. This chapter gives a brief review of the application of the two groups of techniques. Correlations for predicting bubble dynamic properties will also be discussed in this chapter.

2.1. Sensor Based Methods for Bubble Property Measurements

2.1.1 Optical Sensors

One of the earliest reports using optical sensors was that by Yasui and Johanson (1958). Their methodology has formed the basis of many subsequent studies. In their pioneering work, a light source which consisted of a 3.175 mm diameter tungsten filament lamp coupled to a 2.38 mm outside diameter metal tube was used. Facing the lamp was a small mirrored glass prism cemented to one end of a clear quartz tube with 4 mm diameter, which was wrapped with an aluminum foil. Two such probes separated by a short variable distance were positioned one above the other and the assembly was immersed in a fluidized bed of powder. When a bubble filled the space between the lamp and the prism, light was transmitted to the prism and reflected out through the quartz rod into a vacuum phototube. Here, the light pulse was converted into an electrical signal which was amplified and recorded on the moving chart of an oscillograph. The bubble rise velocity was then estimated from the time lag between the signals from the two probes and from their known distance apart. The system was not able to provide information on bubble volumes, but the results clearly showed that bubbles increase in size and velocity as they rise in the bed and also with increase in the particle size of the bed materials. It was also shown that the bubble velocity increases with increasing the fluidizing gas velocity.

Whitehead and Young (1967) designed a device, based on the same principles as that of Yasui and Johanson (1958), to analyze bed behavior and bubble properties over a wide range of operating conditions. The device consisted of a 14×14 array of probes covering an area of 0.68 m^2. Although the scale of scrutiny of individual probes was quite coarse, the array did provide useful information on the behavior of large beds and, particularly, on the formation and location of preferred bubble tracks within the bed.

Put *et al.* (1973) used a single light source situated a variable distance opposite a photodiode detector to monitor bubble flow in a freely bubbling bed. The number of bubbles flowing through the probe was counted over a period of 21 minutes and from the known distance of separation of the source and the detector the cumulative density function of bubble width was obtained. The results were in substantial agreement with those obtained by Yasui and Johanson (1958).

A small optical fiber probe developed by Okhi and Shirai (1976) consisted of three fibers bound together such that the fiber at the center of the bundle provided the illumination that was detected by the other two. The probe was designed primarily to study the movement of solid particles in a bed but it was adapted to investigate bubble flow. Yoshida *et al.* (1978) used laser light and optical fibers to measure the size distribution of bubbles in gas fluidized beds at positions from close to the distributor to the bed surface.

The distributions were found to be bimodal, which was in contrast to those of other workers using less invasive techniques of observation.

Light sensors, in general, have not proved as effective as other techniques for measuring local properties of bubbling fluidized beds. One obvious source of uncertainty is the extent to which some of the probes interfere with the flow of gas and bubbles. The interpretation of electrical signals generated by the probes is another potential source of problems. Optical probes have, however, been applied with greater success in the study of the movement of solid particles, particularly in high-velocity circulating beds. This application is beyond the scope of this review and is not discussed here.

2.1.2 Capacitance Probes

The principle of this method is that the capacitance of a gas-solid mixture, such as the emulsion phase of a fluidized bed, is a strong function of the concentration of solids in the mixture. A probe inserted into a bed to measure a local value of capacitance will thus respond to a change in the local concentration of solids, such as that occurs when a gas bubble engulfs the probe. Particles used in fluidized beds are typically electrical insulators (such as silica, sands and polymer resins) and hence capacitance is a more appropriate property to measure than electrical resistance or conductivity, although such properties have also been investigated.

The first application of capacitance probes in fluidization measurements was reported by Morse and Ballou (1951) who investigated the "uniformity of fluidization" of a bed with fine particles. Later, Lanneau (1960) used the same technique to obtained more comprehensive data with alumina particles with mean diameter of about 80 μm in a gas fluidized bed 7.5 cm in diameter and 10 m in height. The probes used in the measurement were parallel-plate condensers connected to an oscillator and then to an oscillograph. The probes were positioned horizontally so that the tips were at the center of the bed. The responses of the probes were claimed to be in linear variation with the solid concentration at the tip.

The problems inherent in interpreting the results of capacitance probe measurements were discussed in detail by Geldart and Kelsey (1972). The design of the capacitance probes they used was similar to those used by Lanneau (1960). It consisted of two parallel rectangular plates of size 1.5 cm× 0.5 cm, separated by a gap of 0.5 cm. The probe was first tested in a 2-D fluidized bed of sand and then applied to a 3-D bed. They concluded that it is necessary to calibrate the probe, preferably using a non-invasive technique such as X-ray ciné photography, otherwise an error up to a factor of 10 might be introduced. Gunn and Al-Doori (1985) also stressed the importance of proper calibration of probes and of allowing for the stochastic interaction between the bubble interface and the probe.

Werther and Molerus (1973a, b) conducted a meticulous study on the design and use of capacitance probes, which has been the touchstone for subsequent work in this research area. They identified the essential features of a probe suitable to determine local values of bubble gas flow, bubble volume fraction, mean pierced bubble length and mean bubble rise velocity. Such a probe should:

- disturb the bed as little as possible;
- measure local variations;
- have a rapid response to change in voidage;
- have adequate mechanical strength;
- be moveable within the bed;
- be compatible with the bed solids.

With these considerations, a miniature capacitance probe was designed and developed. The probe was shaped in the form of a spike with a central protruding needle forming one pole and the enclosing metal tube the other pole of the capacitor. By processing the signals properly and by using the cross-correlation of two signals obtained from two probes separated by a distance, Werther and Molerus, (1973a, b) obtained bubble size and rising velocity.

2.1.3 Pressure Sensors

Pressure measurements have always been used in research work on fluidized beds. Measurement of the overall bed pressure drop as a function of the gas flow velocity through the bed is used to determine the minimum fluidization velocity of the bed material. Also, time averaged values of pressure difference between two locations are routinely used in industrial units to give an estimation of bed height.

More detailed information on flow hydrodynamics can, however, be obtained from the study of pressure fluctuations within the beds. These fluctuations are generally considered as the consequence of bubble flow, but the exact details of causes and effects have been the source of much discussion. The eruption of bubbles at the bed surface could cause pressure waves that travel back down in the bed. The coalescence of bubbles below the bed surface and bubble formation at the distributor are also considered to lead to pressure variations. Early works were reported by Winter (1968) and Taylor *et al.* (1973) who used pressure sensors to investigate the quality of fluidization.

Littman and Homolka (1970) observed that when a single bubble passes through a pressure sensor a pressure peak is registered as the bubble roof touches the tap and a pressure trough as the bubble floor reaches the tap. Fan *et al.* (1981) found that the cross-correlation of the signals from two tapping points separated by a distance of 10 cm indicated that the signal from the upper tap had a time delay of 0.101 s compared to that from the lower tap. The authors concluded that the time delay is caused by the passing of a bubble. The bubble or slug velocity could be calculated by dividing the distance by the time delay when the bed is operated in a bubbling or slugging regime. However, if the bed is operated in a turbulent regime, the velocity is considered to be the velocity of the fluctuation waveforms (Fan *et al.*, 1983). Studies on gas phase dynamics in fluidized beds using pressure measurements were also reported by Gibilaro *et al.* (1988), Roy *et al.* (1990), Musmarra *et al.* (1992) and Kantzas *et al.* (2000).

Kantzas *et al.* (2000) provided the details of the research work on pressure fluctuation measurements in the Tomographic Imaging and Porous Media (TIPM) laboratory. Experiments were performed to measure the mean pressure and pressure fluctuation in a 20 cm diameter fluidized bed with polyethylene resins and sand as the solid phase and air as the gas phase. The relationship between the air velocity and the standard deviation of the pressure signal was examined to estimate relative bubble size. The frequency of the fluctuation of the pressure signal was also analyzed to quantify bubbling and slugging frequency. It was found that a narrow particle size distribution causes an immediate drop in the fluctuation frequency at minimum fluidization, while a wide particle size distribution leads to a gradual drop in fluctuation frequency from the minimum fluidization velocity to the velocity at which the transition from low bubbling to vigorous bubbling occurs. Above this velocity, in all cases, the fluctuation frequency decreases gradually and linearly with gas velocity. It was concluded that there is a significant difference in the nature of the bubbles between these two regimes with many small bubbles at low bubbling conditions and fewer large bubbles at vigorous bubbling conditions.

It is worth mentioning that caution should be executed with the use of immersed probes or sensors for examining bubble dynamics due to the fact that various probes or sensors always disturb the bubbles to some degree. Rowe and Masson (1981) conducted a study in which an X-ray ciné photography was employed to view the interior of a fluidized bed containing various probes of different size and shape. They concluded that all probes affect bubble behavior to a greater or less extent and that bubbles tend to accelerate, elongate and deviate so that they climb the probe stem. To overcome the disturbing effect and limitation of various probes, non-invasive methods have been developed and used in the quantification of gas phase dynamics in fluidized beds in the last 30 years. A brief review is given in the following section.

2.2. Non-Invasive Imaging Methods for Bubble Property Measurements

Techniques have been developed to utilize the attenuation of a transmitted energy beam to produce an image for a fluidized system. Compared to other methods the major advantage of those techniques is obvious-being totally non-invasive and insignificantly affected by harsh conditions, such as high temperatures and pressures.

The basis of energy attenuation based methods is the well-known Beer-Lambert law:

$$I = I_0 \exp(-\mu\rho l) \tag{2.1}$$

where

I = the transmitted intensity

I_0 = the incident intensity

μ = the attenuation coefficient of the material

ρ = the density of the material

l = the path length

For a gas solid fluidized bed, Equation (2.1) is written as:

$$I = I_0 \exp[-(\mu_g \rho_g \varepsilon_g + \mu_s \rho_s (1-\varepsilon_g))l] \tag{2.2}$$

where ε_g is gas voidage in the fluidized bed. The subscripts g and s indicate gas phase and solid phase.

For a given imaging system and a given fluidized bed, the incident intensity and the path length are fixed, so that the transmitted intensity is a function of density and holdup of the individual phase. By measuring transmitted intensity in the horizontal direction, individual phase holdup can be obtained by employing a reconstruction algorithm, which is well known as computed tomography (CT). With a video camera that is operated at a certain frequency, say 30 frames/s, measurements of transmitted intensity in vertical direction yield images of the bed with different colors or gray scales. These different colors and gray scales represent different transmitted intensities and therefore different values of gas voidage. Bubbles in the images can be readily distinguished from the surrounding emulsion phase. The acquired images can then be processed to obtain the bubble size, shape, velocity, generation frequency, bubble volume fraction and other dynamic properties either by manual measurements or by computer programming after being properly digitized.

2.2.1 X-ray Imaging

Generally there are two different kinds of systems using X-ray imaging, X-ray radiography and X-ray tomography. Backed by the physics as discussed above, X-ray radiography provides images in a vertical plane while X-ray tomography gives images in a cross-sectional plane.

In X-ray radiography, the attenuation of the beam emitted by an X-ray source is registered by sheets of film or an image-intensifier camera. The registered images are then recorded on a ciné camera or a video-recorder for processing either manually or with a computer program. This technique has been used for many years to view the interior of fluidized beds and to monitor bubble motion.

The first reported application of X-ray radiography in study of fluidized beds was by Grohse (1955), who measured the density variation of a silicon powder bed as a function of the fluidizing gas velocity. Romero and Smith (1965) used flash X-ray radiography to study the internal structure of fluidized beds. Data on bed density distribution, and the shape, size and rising velocity of bubbles were obtained in a 3"×3" square bed with sand as the solid phase and air as the gas phase. Since the X-ray facilities used by Romero and Smith (1965) could not be operated in a continuous mode with a high sampling frequency, two flash X-ray units, one of which was operated at 300 kV and the other at 600 kV, were used to measure the bubble velocity. The two X-ray units were mounted with a fixed vertical distance and fired sequentially with a time delay of a few tenths of a second. Bubble velocity can be readily determined with the distance that the bubble travels and the time interval.

A lot of work on fluidized systems using X-ray radiography has been conducted by Rowe, Yates and co-workers at University College London. Bubble dynamic properties such as bubble growth, bubble splitting, the effects of gas distribution, elevated temperature and pressures and co-axial nozzles have been studied via X-ray imaging since the mid-sixties (Rowe and Partridge, 1965,1997). Initially, images of the bubbles in fluidized beds were projected from ciné film negatives on a screen and a circle was drawn by hand around the edge of each bubble to find the bubble diameters. Bubble velocity measurements were conducted by following each bubble over a few centimeters of travel and measuring the movement of the center of the fitted circle from a datum line on the photograph. This technique was later improved (Rowe and Everett, 1972 a-c; Rowe and Yacono, 1976) by introducing a Hewlett Packard 9874A digitizer coupled to a computer which converted the bubble silhouettes from the digitized co-ordinates to population statistics of averaged bubble diameter, volume and velocity etc. More innovations (Yates and Cheesman, 1992, Yates *et al.*, 1994) have been made to establish an image analysis system. In the work of Yates *et al.* (1994), the registered images were recorded by a JVC video recorder at an equivalent speed of 25 frames/s and transferred off-line for processing and analysis using Bioscan's Optimas software. It was claimed that the system is able to visualize the regions close to the boundaries of the rising bubbles in gas-solid fluidized beds (Yates, 1997).

Radiography techniques were also employed by Gambin *et al.* (1993) to characterize flow patterns above the air ring nozzles in a FCC regenerator and by Weinstein *et al.* (1992) to study gas solid flow behavior in fast fluidized beds.

Banholzer *et al.* (1987) conducted a feasibility study for direct imaging of time-averaged flow patterns in a model fluidized bed using a medical X-ray CT scanner. The CT scanner consisted of an 88 kV X-ray tube, placed to one side of the reactor, and an array of 517 gas-filled detectors on the opposite side.

A fourth generation medical X-ray CT scanner has been used for the study of gas fluidized beds and trickle beds (Kantzas, 1994). The CT scanner (EMI7070) was modified to perform scans in both vertical and horizontal directions. Objects with diameters up to 32 cm could be scanned using X-rays with energies between 100 and 140 kV. Images can be generated in 3 s with a spatial resolution of 0.04 cm×0.04 cm ×0.5 cm. Experiments were conducted with glass bead particles (0.05-0.08 cm) and polyethylene particles (0.04 cm) as bed materials in a 10 cm diameter fluidized bed. From the images generated, cross sectional distribution of gas holdup (voidage) can be computed using a calibration curve. The calibration correlates X-ray absorption to material density that is then linearly proportional to voidage. The same facility was further used to monitor the fluidization characteristics of polyolefin resins in a 10 cm diameter fluidized bed (Kantzas and Kalogerakis, 1996). Furthermore, the facility was employed for quantification of channeling in a 10 cm diameter polyethylene resin fluid bed (Kantzas *et al.*, 1997). With hundreds of images collected at different positions along the bed and at different time, the formation and propagation of gas channels were determined in both spatial and temporal domains.

Some preliminary experiments have been conducted in the TIPM lab using an X-ray fluoroscopy system (GE MPX-100) to obtain images in gas-solid fluidized beds (Li *et al.*, 1999). The application of this system in fluidized beds to gain detailed information of bubble dynamic properties is the subject of this study.

2.2.2 γ-Ray Imaging

Investigations on laboratory-scale fluidized beds using gamma-ray attenuation techniques have been widely reported. Baumgarten and Pigford (1960), Bloore and Botterill (1961) and Clough and Weimer (1985) all measured gas-bubble sizes and frequencies under different operating conditions with density gauge-type devices which could travel vertically up and down along the fluidized bed vessels. Orcutt & Carpenter (1971) used a similar device to study bubble coalescence. The physics behind such gauges is that the ionization of gas in a radiation detector is a function of the amount of radiation received.

By proper calibration, therefore, the output signal is directly related to the voidage between the radiation source and the detector. Weimer *et al.* (1985) have conducted a comprehensive study on the use of gamma-ray attenuation gauges on fluidized bed systems. They used a modified, off-the-shelf, density gauge (500 mCi point source of Cs^{137}) to measure the two phase properties in both a 29.2 cm diameter bed, operated at ambient temperature and pressure, and a 12.8 cm diameter bed, operated at pressures as high as 8300 kPa. The solids were either silica sand (mean diameter about 0.0287 cm), fluidized by air, or activated carbon (mean diameter about 0.0066 cm), fluidized by a synthesis gas mixture. In their paper, Weimer *et al.* (1985) discussed the requirements of beam diameter, the balance between detection noise and scan duration and the difficulties in data interpretation. They concluded that gamma-ray density gauges are suitable for relatively accurate measurements of phenomena such as expanded bed height, dense phase voidage, and centerline bubble phase volume fraction. However, the measurement of bubble size is, at best, approximate.

Seville *et al.* (1986) pioneered the use of a rather primitive gamma-ray technique to generate tomographic images (tomograms) of the voidage distribution in the jet region above various gas distributors under different operating conditions. The bed they used was 5.1 cm in diameter and 20 cm in height with two different types of distributors. The solid used in the experiments were spherical soda glass ballotini (0.021-0.025 cm) and angular quartz sand (0.0300-0.0355 cm). The principal objectives of the study were to examine the effects of both background fluidization and particle shape on the axial and radial bed voidage profiles.

A recent application of gamma-ray tomography was reported by Simons *et al.* (1993) to produce reconstructed images of higher resolution at shorter scan times and with larger diameter vessels than those described by Seville *et al.* (1986). The "scanner" employed an array of 6 Gd^{153} sources in conjunction with 6 collimated CsI scintillation detectors. The bed used was 10 cm in diameter and the bed material was activated carbon (mean diameter = 0.0906 cm). The bed was operated in a slugging regime with a superficial gas velocity of 37 cm/s (gas bubble diameters are comparable to the diameter of the bed) to provide images of the cone/jet and bubble/slugging regimes.

2.2.3 Capacitance Imaging

The principle of capacitance measurement in gas-solid systems is quite straightforward and understandable. The capacitance of the bed varies with the solid materials and their concentration. However, the capacitance probes may interfere with the flow structure in the bed when mounted inside of the column. Many workers have made efforts to resolve this problem, notable contributions being those of Ormiston *et al.* (1965), and Halow and Nicoletti (1992). Ormiston *et al.* (1965) attached two sets of capacitor plates to the outside of perspex columns of various diameters (2.5-14 cm) with a vertical distance of 2.5 cm. Sand particles were used as the solid material. The change in capacitance between the plates due to the passage of bubbles was monitored by proximity meters. The first capacitance imaging system was reported by Halow *et al.* (1990) to study flow behaviors in gas-solid fluidized beds. The system was later modified by Halow and Nicoletti (1992) and Halow *et al.* (1993). It is reported that the more sophisticated system can provide images of the voidage distribution in three dimensions within fluidized beds at rates of 60-100 frames/s. The capacitance imaging system is comprised of 4 sets of 32 electrodes mounted at various positions along the vertical height of a 15.2 cm diameter column. The images obtained allow the direct observation of bubble coalescence phenomena and the interpretation of data such as bubble rising velocities, bubble size and voidage distributions in the emulsion phase.

Capacitance imaging technique has higher temporaral resolution (high speed of data collection) than X-ray and γ-ray imaging techniques. It allows the study of highly evanescent phenomena such as the bubble rising velocity and bubble diameter, the formation of voids near minimum fluidization, and the behavior of a gas jet in the entrance region of a fluidized bed.

However, Halow *et al.* (1992) pointed out that there are significant limitations to this technique, leading to an uncertainty in the exact values of voidage calculated from the imaging data. The main limitation of the technique is the poor spatial resolution. In the horizontal direction, the pixel size is in the order of 1.0 cm while in the vertical the pixel size is 2.5 cm. The application of capacitance image technique in gas-solid fluidized beds was summarized by Halow *et al.* (1997).

2.3. Correlations for Predicting Dynamic Bubble Properties

2.3.1 Correlations for Predicting Bubble Size

As mentioned before, bubble size is one of the most important parameters in determining hydrodynamics of bubbling fluidized beds. Kunii and Levenspiel (1991) pointed out that bubbles reach a small limiting size in fine particle systems and are larger in large particle systems. In literature, a number of correlations for predicting bubble diameter have been proposed (Yasui and Johanson,1958; Geldart, 1970-1971; Mori and Wen, 1975; Rowe, 1976; Darton *et al.,* 1977; Werther, 1978; Horio and Nonaka, 1987; Choi *et al.,* 1988, 1998). However, caution should be observed when one is using these correlations because each correlation has its own applicable range of bed materials and operating conditions.

Mori and Wen (1975) proposed that for Geldart B and Geldart D solids, the bubble size d_b at any height z in the bed is given as:

$$\frac{d_{bm} - d_b}{d_{bm} - d_{b0}} = e^{-0.3z/d_t} \tag{2.3}$$

where d_{b0} is the initial bubble size formed near the bottom of the bed. For a porous plate distributor

$$d_{b0} = \frac{3.685}{g}(U_f - U_{mf})^2 \quad [cm] \tag{2.4}$$

d_{bm} is the limiting size of bubble expected in a very deep bed and given by the following equation:

$$d_{bm} = 0.65[\frac{\pi}{4} d_t^2 (U - U_{mf})]^{0.4} \quad [cm] \tag{2.5}$$

The ranges of data from which this correlation was obtained are

$$d_t \le 1.3m \qquad 0.5 \le U_{mf} \le 20\ cm/s$$

$$60\mu m \le d_p \le 450\mu m \qquad U - U_{mf} \le 48\ cm/s$$

Werther (1978) gave the following expression for bubble size at any height z in a bed of Geldart B solids supported by a porous plate distributor:

$$d_b = 0.853[1 + 0.272(U - U_{mf})]^{1/3} (1 + 0.0684z)^{1.21} \quad [cm] \tag{2.6}$$

The applicable ranges of operating conditions for this correlation are:

$$d_t > 20cm \qquad 1 \le U_{mf} \le 8\ cm/s$$

$$100 \le d_p \le 350\mu m \qquad 5 \le U - U_{mf} \le 30\ cm/s$$

Horio and Nonaka (1987) proposed a new bubble diameter correlation that takes into account both splitting and coalescence to predict bubbling characteristics of fluidized beds of various powders including Geldart group A.

$$\left(\frac{\sqrt{d_b} - \sqrt{d_{be}}}{\sqrt{d_{b0}} - \sqrt{d_{be}}} \right)^{1-\gamma_M/\eta} \left(\frac{\sqrt{d_b} + \sqrt{\delta}}{\sqrt{d_{b0}} + \sqrt{\delta}} \right)^{1+\gamma_M/\eta} = \exp(-0.3 \frac{z - z_0}{d_t}) \tag{2.7}$$

where the parameters δ and η are defined as follows:

$$\delta / d_{bm} = (\gamma_M + \eta)^2 / 4$$
$$\eta = (\gamma_M^2 + 4d_{bm} / d_t)^{0.5} \tag{2.8}$$

The authors stated that for the cases of Geldart group B powders the correlation automatically converges to the conventional correlation of Mori and Wen (1975), whose predictions are close to those of Rowe (1976) and Darton *et al.* (1977).

In 1998, in order to derive a consistent interpretation of mean bubble size from the bubbling behaviors of fluidized beds of Geldart's group A, B and D particles, a generalized bubble-growth model was proposed by Choi *et al.* (1998). In the model, bubble diameter can be estimated from the following equation:

$$\left[\frac{d_{b0} - d_{b,eq}}{d_b - d_{b,eq}}\right]^b \left[\frac{(d_{b0}^{1/2} - d_{b,eq}^{1/2})(d_b^{1/2} + d_{b,eq}^{1/2})}{(d_b^{1/2} - d_{b,eq}^{1/2})(d_{b0}^{1/2} + d_{b,eq}^{1/2})}\right]^{d_{b,eq}^{1/2}} = \exp(2(h/a + d_b^{1/2} - d_{b0}^{1/2})) \tag{2.9}$$

where a and b are:

$$a = 4.266 g^{1/2} / f_s^* \qquad b = \frac{(U - U_{mf})}{0.711 g^{1/2}} \tag{2.10}$$

$$d_{b,eq} = 6.792(U - \beta U_{mf}) / f_s^* \tag{2.11}$$

U : superficial gas velocity

U_{mf}: minimum fluidization velocity

h : height of bed

f_s^* :splitting frequency of a single bubble

d_{b0} : bubble diameter at distributor

$d_{b,eq}$: equilibrium bubble diameter (when coalescence frequency equals breakup frequency)

$$f_s^* = 6.47\times10^{-4}(U/U_{mf})^{0.454}\, g/U_{mf}$$

$$d_{b0} = 1.38\left[\frac{A(U-U_{mf})}{N_0 g^{1/2}}\right]^{0.4} \quad \text{for } a \text{ perforated plate}$$

$$d_{b0} = 3.685(U-U_{mf})^2/g \quad \text{for } a \text{ porous plate}$$

$$d_{b,eq} = 6.792(U-\beta U_{mf})/f_s^*$$

$$\beta = (U/U_{mf})^{0.62}$$

Choi *et al.* (1998) claimed in their paper that the correlations they proposed were successfully applicable to beds of Geldart's group A, B, and D particles.

2.3.2 Correlations for Predicting Bubble Velocities

Davidson and Harrison (1963) proposed the following rise velocity equation for bubbles in bubbling beds.

$$u_b = u - u_{mf} + 0.711\sqrt{gd_b} \tag{2.12}$$

A more general equation that covers the whole range of particle sizes from Geldart A to D was reported by Werther (Kunii and Levenspiel, 1991) for the prediction of bubble rising velocity:

$$u_b = \Psi(u_f - u_{mf}) + \alpha u_{br} \tag{2.13}$$

where Ψ is the fraction of visible bubbles, given by the following equation:

$$\Psi = \left(\frac{observed\ bubble\ flow}{excessflow,\ from\ two-phase\ theory}\right) = \frac{v_b}{(u-u_{mf})A_t} \tag{2.14}$$

and α in Equation (2.13) is a factor that accounts for the deviation of bed bubbles from a single rising bubble. From his experimental data, Werther recommended the following for α:

Geldart Classification of Solids	A	B	C
α	$3.2\ d_t^{1/3}$	$2.0\ d_t^{1/2}$	0.87
d_t (m)	0.05-1.0	0.1-1.0	0.1-1.0

Kunii and Levenspiel (1991) proposed the following correlations by analyzing some experimental data.

For Geldard A solids with $d_t \leq 1$m

$$u_b = 1.55\{\ (u-u_{mf}) + 14.1(d_b + 0.005)\ \}d_t^{0.32} + u_{br}\ [m/s] \tag{2.15}$$

For Geldart B solids with $d_t \leq 1$m

$$u_b = 1.6\{(u-u_{mf}) + 1.13d_b^{0.5}\ \}d_t^{1.35} + u_{br}\ [m/s] \tag{2.16}$$

For both Geldart A and Gekdart B solids

$$u_{br} = 0.711(gd_b)^{1/2} \tag{2.17}$$

Kunii and Levenspiel (1991) stated that these correlations fit the experimental data well.

Mori and Wen's correlation for bubble diameter and Kunii and Levenspiel's correlation for velocity was chosen to predict bubble diameter and bubble rising velocity in this study. A comparison between predicted results and the results from image processing will be shown in Chapters 5.

CHAPTER 3
EXPERIMENTAL WORK

This research work focuses on bubble flow dynamics, including bubble diameter, bubble velocity, bubble flow patterns, bubble occurrence frequency and bubble volume fraction, in fluidized beds using X-ray imaging. In this chapter, the experimental set-up and experiments conducted in the lab will be described and the experimental results will be analyzed in a preliminary way.

3.1. Experimental Set-up

For the current research work the experimental set-up consists of a fluidized bed column with a 10 cm diameter and an X-ray imaging system. The X-ray imaging system is a medical fluoroscopy system GE MPX-100. The components of the system include an X-ray tube, an image intensifier, an X-ray camera and a closed circuit television system. A diagram of the experimental set-up is shown in Figure 3.1.

The X-ray tube generates X-rays with a pulse frequency of 1000 Hz (time exposure is 1 ms). The image intensifier is used to convert incident X-ray radiation into a light image to be viewed, recorded or photographed. An image intensifier consists of an evacuated glass, aluminum or non-ferromagnetic envelope that contains an input phosphor, photo-cathode, electrostatic focusing lenses, accelerating anodes and output phosphor as shown in Figure 3.2. The input phosphor absorbs X-ray photons and re-emits part of this absorbed energy as a large number of light photons. Light photons emitted by the image intensifier input phosphor are absorbed by a photo cathode, which emits photoelectrons. The photoelectrons are accelerated across the image intensifier tube by the anode and are focused on the output phosphor by an electrostatic lens. These electrons ranging from 25 to 35 keV, are absorbed by the output phosphor. Thus, the pattern of incident X-ray intensities at the input phosphor is converted into an intense pattern of light at the output phosphor of the image intensifier.

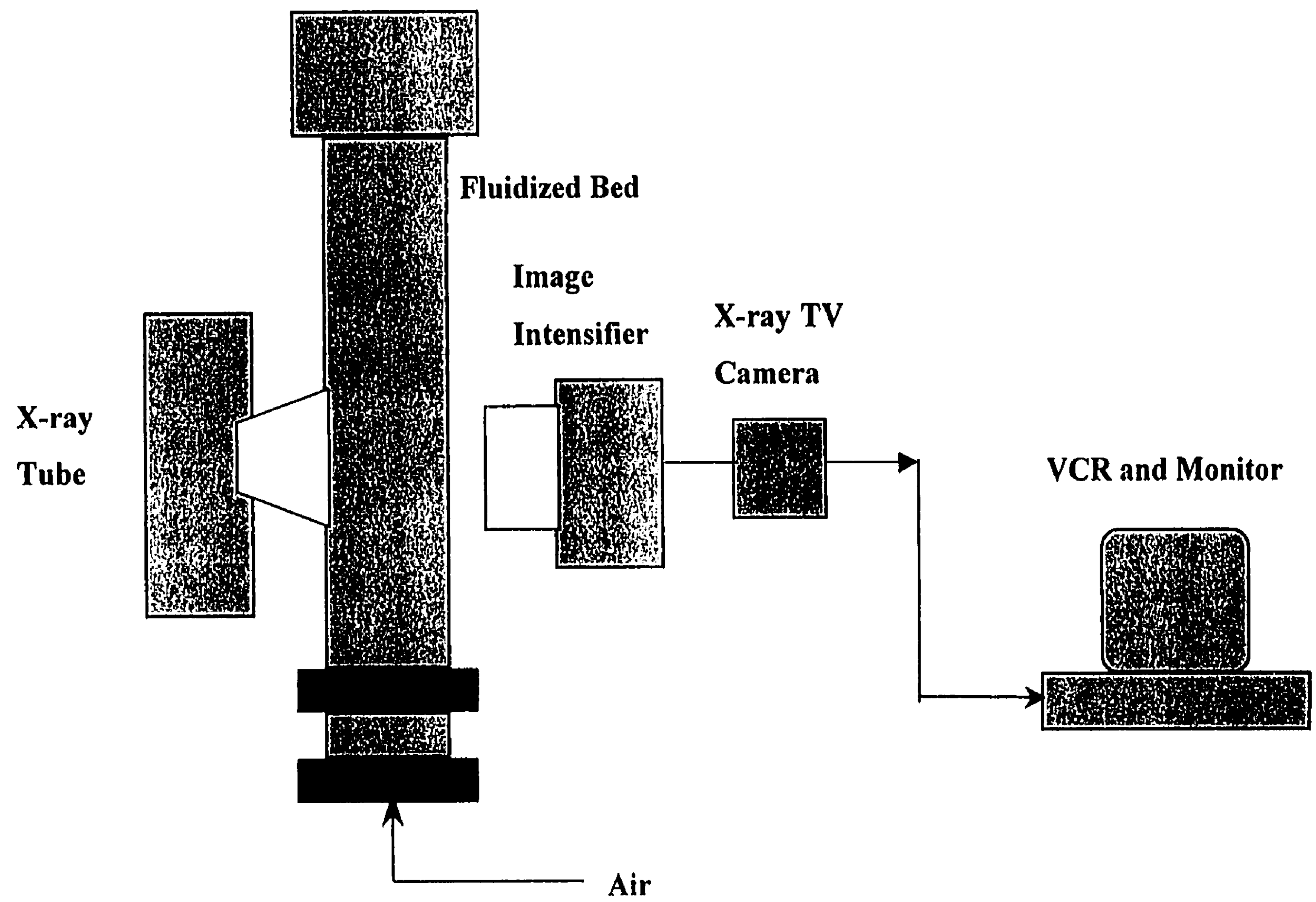

Figure 3.1. Diagram of experimental set-up

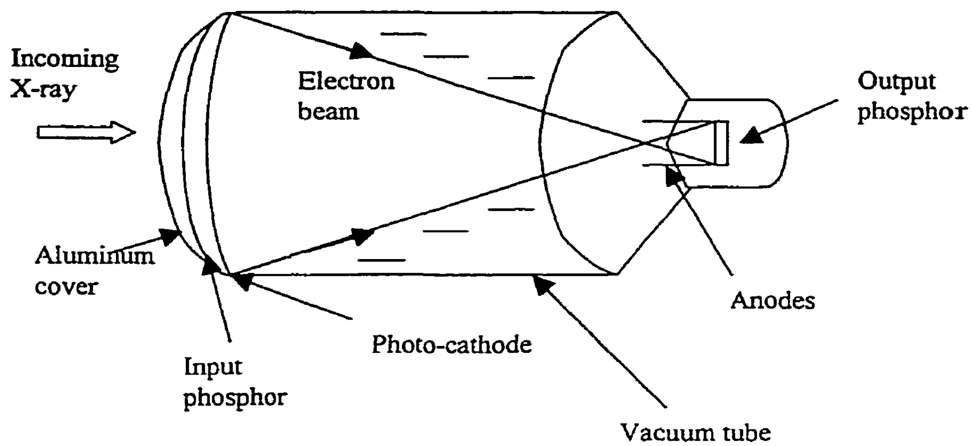

Figure 3.2. Diagram for image intensifier

The imaged area is a circle of 23 cm in diameter. The central portion of an image generated by the image intensifier has a limiting spatial resolution of 4-5 lines per millimeter (l/mm). The resolution decreases at the edges of the image intensifier. Fluoroscopy is performed at low doses, which means that relatively few X-rays are used to produce the image. This results in high noise levels. Several factors contribute to loss of contrast. One is that some X-rays pass through the input phosphor and photo-cathode and strike the output phosphor. Another one is that some light produced at the output phosphor travels back to the photo-cathode and produces more electrons.

Contrast is also reduced by veiling glare, which is the result of light scattered and reflected within the image intensifier and output window. The image intensifier also has some artifacts. One is the lag that is related to continued luminescence after X-ray stimulation has stopped. Pincushion distortion is another artifact, which is produced by the image intensifier as a result of inadequate electronic focusing and can increase magnification at the periphery. Those effects can be removed by subtracting image background, which will be discussed in Chapter 4.

The fluoroscopy system uses a closed circuit television (TV) system to view the image obtained from the image intensifier. The X-ray TV camera converts light images into electric video signals that are recorded on videotapes for digitizing and image processing. The display monitor converts video signals back into the "original" image for direct viewing. The video recording system reads 30 image frames per second.

X-ray imaging experiments were carried out using a cylindrical column made of plexiglas, 10 cm in diameter and 100 cm in height. The body of the column is tapped with a spacing of 4 cm between T0* and T1* and of 17 cm between T1* and T2* and so on, so that pressure measurements can be made at different heights in the bed as shown in Figure 3.3. The bottom of the column is a distribution system that includes a fixed bed containing spherical glass beads (about 1.0 cm in diameter) under a porous plate type distributor. The distributor used in this study is made of sintered woven wire mesh (Rigimesh®, Grade R, 55 μm) supported on a rigid large-opening metal mesh (about 0.5 cm). The column top ends with an expansion section and the outlet of the expansion section is connected to a solids collection device, a cyclone that is used to capture any entrained fine powders. The set up allows for continuous measurements of flow via a rotameter. The imaging experiments were performed for three gas-solid systems. The three types of particles are polyethylene particles with a narrow size distribution (NPE), polyethylene particles with a wide size distribution (WPE) and sand particles with a narrow size distribution (NS).

In order to determine the superficial gas velocities to be used for the imaging experiments, minimum fluidization velocities were measured for each gas-solids system. Continuous measurements of pressure were conducted by using four pressure transducers, which are attached to the pressure taps on the body of the column, with 1/8 inch (0.32 cm) nylon tubing. The data was acquired and stored onto a computer. The pressure transducers used to collect the pressure tap data were manufactured by

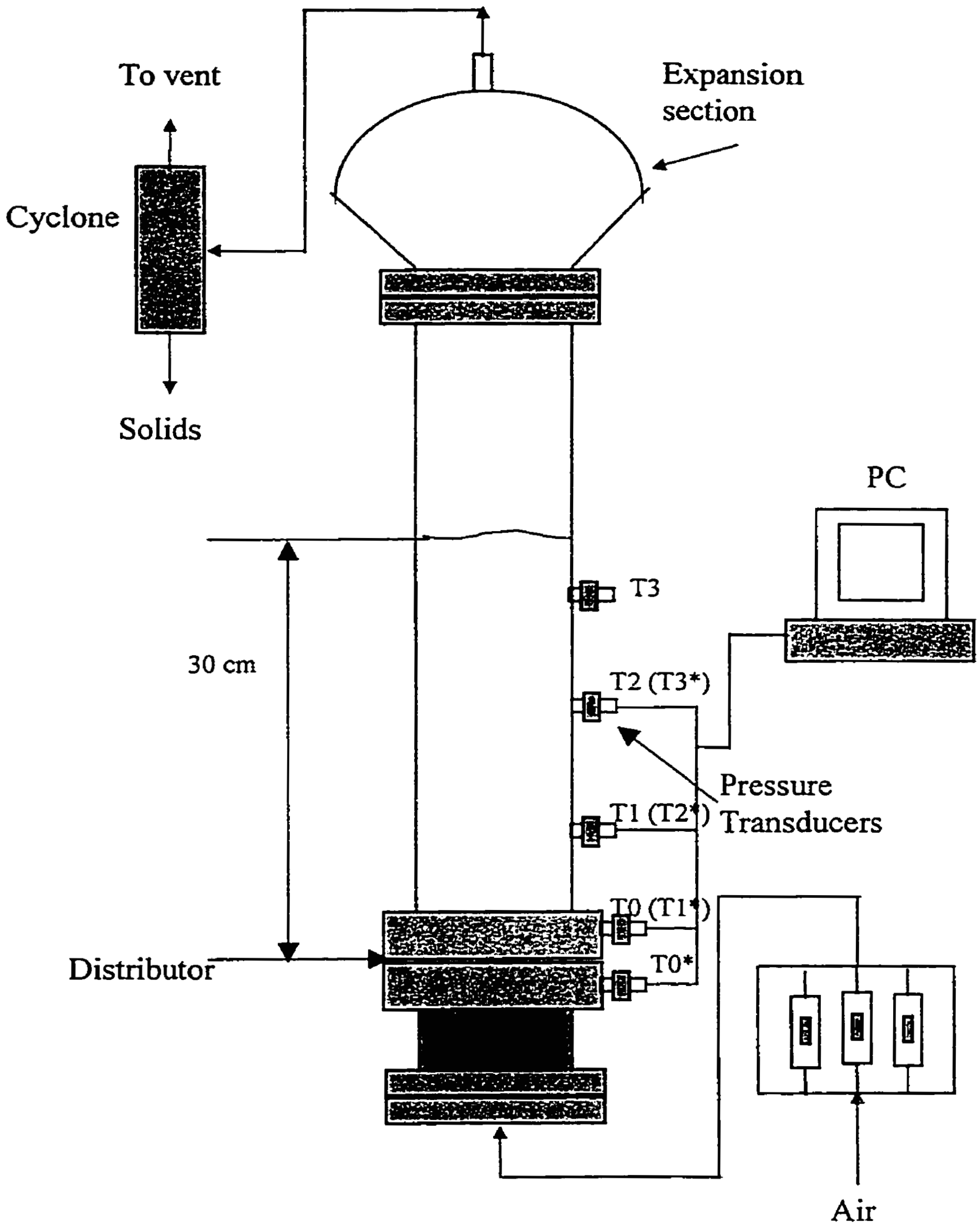

Figure 3.3. Schematic of the fluidized bed set up

Schlumberger Solartron (model 8000DPD). Compressed air at room temperature was used as the gas phase. Polyethylene resin particles and sand particles were used as the solid phase. Several regulators were mounted in the system to maintain a constant air pressure. Three pre-calibrated gas rotameters with different ranges, as shown in Table 3.1, were employed to measure the air flow rates to the fluidized bed. A schematic of the experimental fluidized bed set up is shown in Figure 3.3.

Table 3.1. List of rotameters model numbers

(Products from Bailey Fischer Porter)

	Rotameter for NPE	Rotameter for WPE	Rotameter for NS
Tube	FP1/2-21-G-10/55	FP-1/2-21-G-10	FP-1/2-21-G-10
Float	1/2-GUSVT-40A	1/2-GSVT-45A	1/2-GSVT-45A
Maximum flow rate (SCFM*)	1.35	2.47	2.47
Maximum flow rate (m^3/s)(STP*)	8.02	14.68	14.68

SCFM*: Standard cubic feet per minute.

STP*: Standard temperature and pressure.

3.2. Experiments

Three kinds of particles, NPE, WPE and NS were used as the bed solid phase. The particle size distribution (PSD) plots (Wright, 1999) for the particles mentioned above are shown in Figure 3.4 to Figure 3.6. The properties of those particles are shown in Table 3.2. They are all classified as Geldart group B particles. The beds were fluidized at ambient conditions using air as the gas phase. The experiments were carried out in the 10 cm diameter column with a fixed settled bed height of 30 cm, so that the ratio of the bed height to the bed diameter without flowing gas was 3.0.

Minimum fluidizing velocity for each kind of particles was measured in the laboratory. The values are shown in Table 3.2 along with properties of particles. X-ray imaging experiments were carried out at different superficial gas velocities (Table 3.3) for all kinds of particles. The details of the experimental measurements are summarized in following sections.

Table 3.2. Properties of particles and the fluidized beds

Properties	NPE	WPE	NS
*Mean Particle Diameter μm	543	830	530
*Particle Density, g/cm^3	0.6585	0.6585	2.44
*Particle Sphericity	0.7257	0.7158	0.6376
*Minimum Voidage	0.3405	0.3494	0.48
Gas Density, g/cm^3	1.23E-03	1.23E-03	1.23E-03
Gas Viscosity, Pa.S x 10^5	1.79	1.79	1.79
U_{mf}, cm/s	8.9	7.1	18.5
A_r	3946.8	14095.5	13617.5
$Re_{p,mf}$	2.31	7.66	7.43

*Measured by Wright (1999)

Table 3.3. Superficial gas velocities used in X-ray imaging experiments

	1.5×U_{mf}(cm/s)	2.0×U_{mf}(cm/s)	2.5×U_{mf}(cm/s)	3.0×U_{mf}(cm/s)
NPE	13.2	17.6	21.6*	28.8*
WPE	10.8	14.4	18.0	21.6
NS	N/A	35.2*	N/A	52.8*

* These experiments were conducted by Wright (1999)

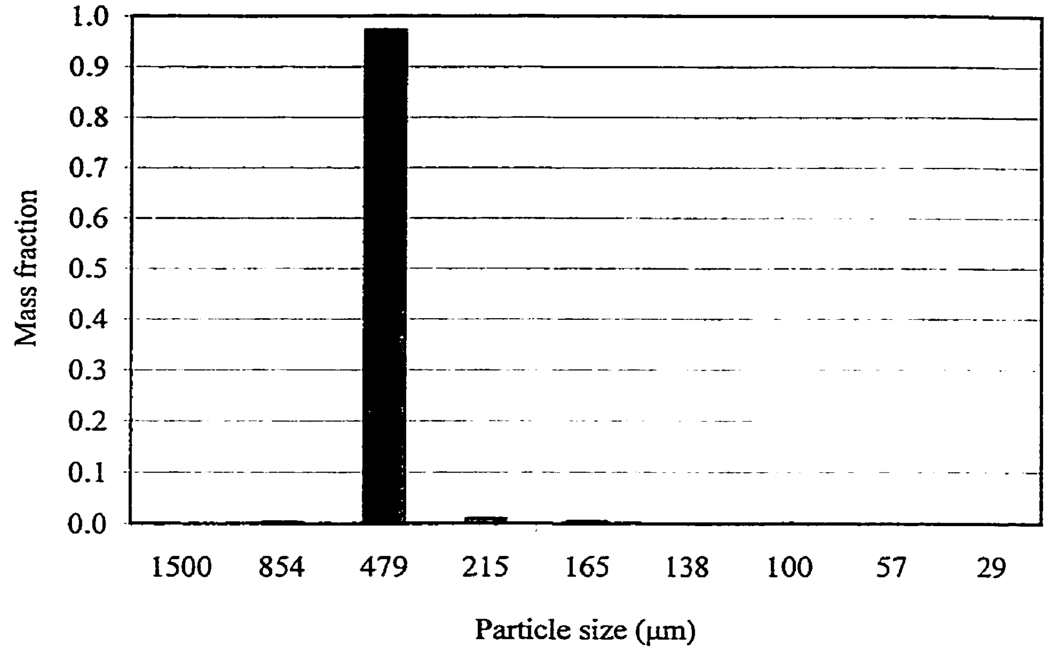

Figure 3.4. PSD for NPE particles

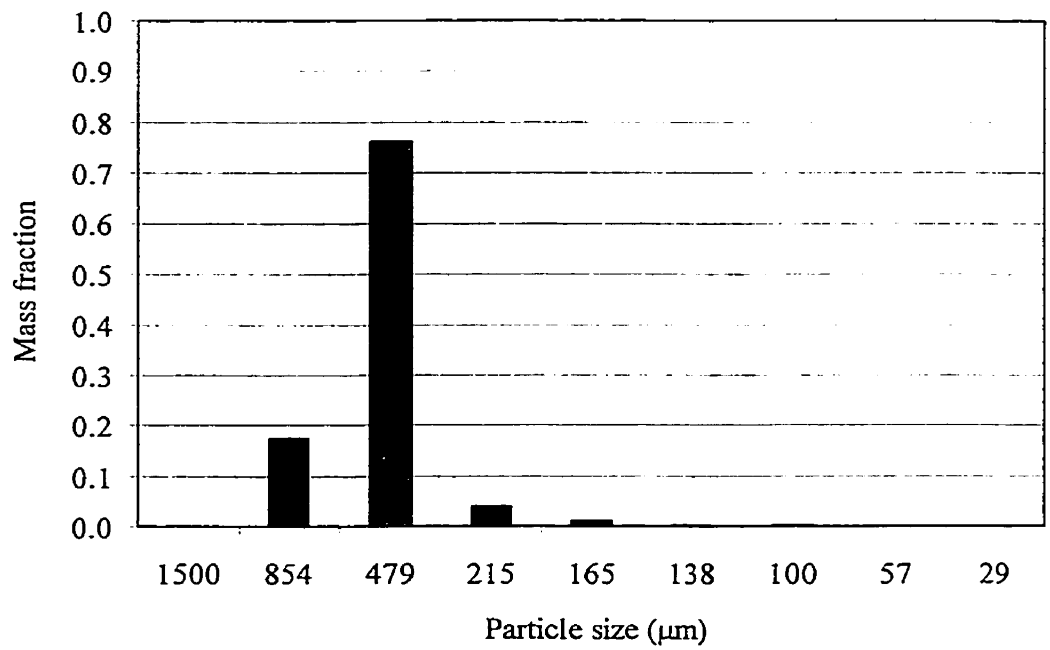

Figure 3.5. PSD for WPE particles

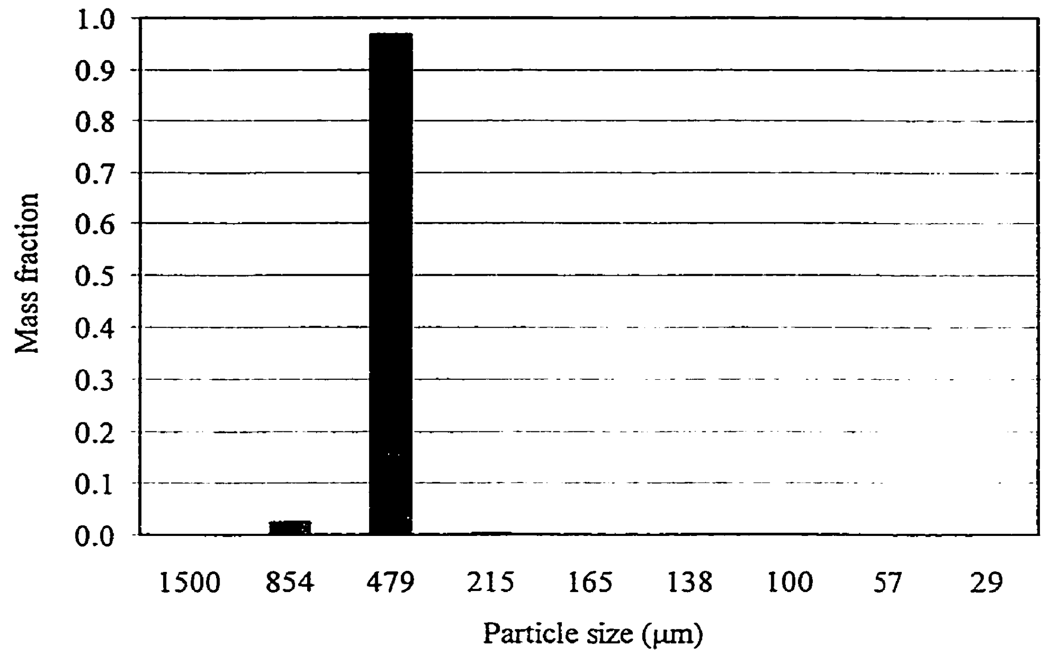

Figure 3.6. PSD for NS particles

3.2.1 Measurements of Minimum Fluidization Velocities

The rotameters used for minimum fluidization velocity measurements are listed in Table 3.1. The rotameters were all operated at a pressure of 137.4 kPa (20 psig). The 10 cm column was used for the minimum fluidization velocity measurements for NPE-air, WPE-air and NS-air systems. Four transducers were employed (Schlumberger Solartron, model 8000DPD). The following is the procedure for the minimum fluidization velocity measurements.

1. Vacuum the inside wall of the column to clean away the residue of the other kind of particles from the column wall and the distributor plate.
2. Fix the column on a stand and install the four-pressure transducers to the stand. Check if the column is vertical. Connect the tubing from the transducers to the bottom four-pressure taps.
3. Make sure that the unused taps are plugged and the sampling port valves are closed.

4. Charge the column with the particles to the desired bed height which is L/D=3 in this study.
5. Install the expansion section to the column body and attach it to a cyclone. Check if the hose is firmly secured to the top of the column.
6. Assemble air feed system. Choose an appropriate rotameter for the air velocities to be used.
7. Fluidize the bed for two hours to remove packing effects. After the 2 hours fluidization, allow the bed to rest for half hour.
8. Create the data sub-directories on the data acquisition computer.
9. Set the airflow on the rotameter to 8% and adjust the rotameter operating pressure. Acquire 20 s of data (2000 samples). Increase the airflow by increments of 2% and acquire the pressure data until maximum flow (100%) is reached.
10. During the first trial, record observations of the changes in bed height, the first appearance of visible bubbles, the changes in readings on the pressure gauges, and any other changes.
11. Repeat step 9, starting at 100% and reducing the airflow by 2% each time.
12. Repeat step 9 and step 10 for two more trials.

The four transducers produce a 4-20 mA signal that runs through a resistance of approximately 250 ohms giving a signal of 0-5 volts. An analog to digital converter reads the voltage through the conversion resistors on a PC-LPM-16 card, from National Instruments, which is mounted in an Intel 386-based PC. The voltage data from the transducers is transferred to an RS6000 workstation where analysis is carried out using Matlab 5.2. The voltage data is converted to pressure data using the measured calibrations. Figures 3.7, 3.8, and 3.9 are the plots of pressure drop along the fluidized bed height versus superficial gas velocity, for NPE-air, WPE-air, and NS-air systems, respectively. From these plots the minimum fluidization velocity for each system can be determined (Kunii and Levenspiel, 1991). The values of the measured minimum fluidization velocities are also shown in Table 3.2.

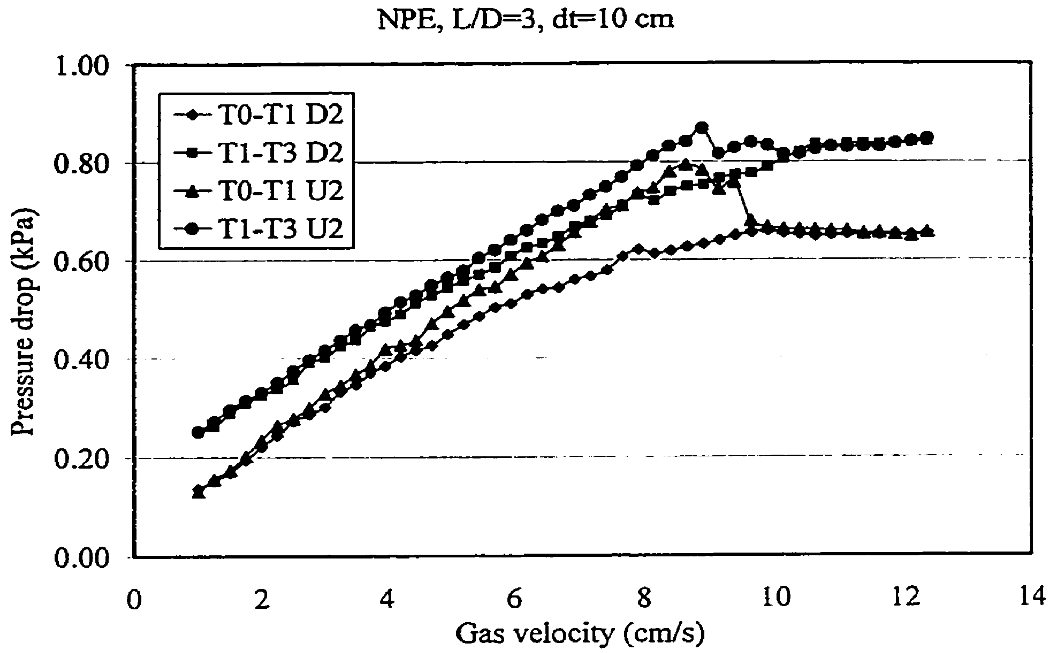

(a)

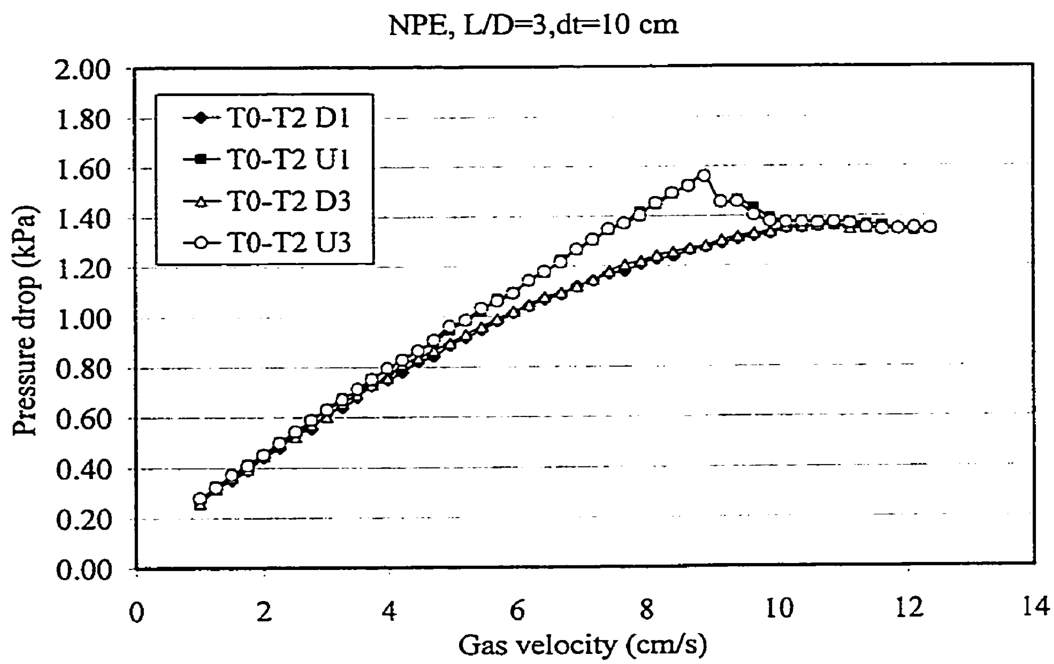

(b)

Figure 3.7. Minimum fluidization velocity plots for NPE-air system, U_{mf}=8.9 cm/s

U1, U2 and U3: increasing velocity

D1, D2 and D3: decreasing velocity

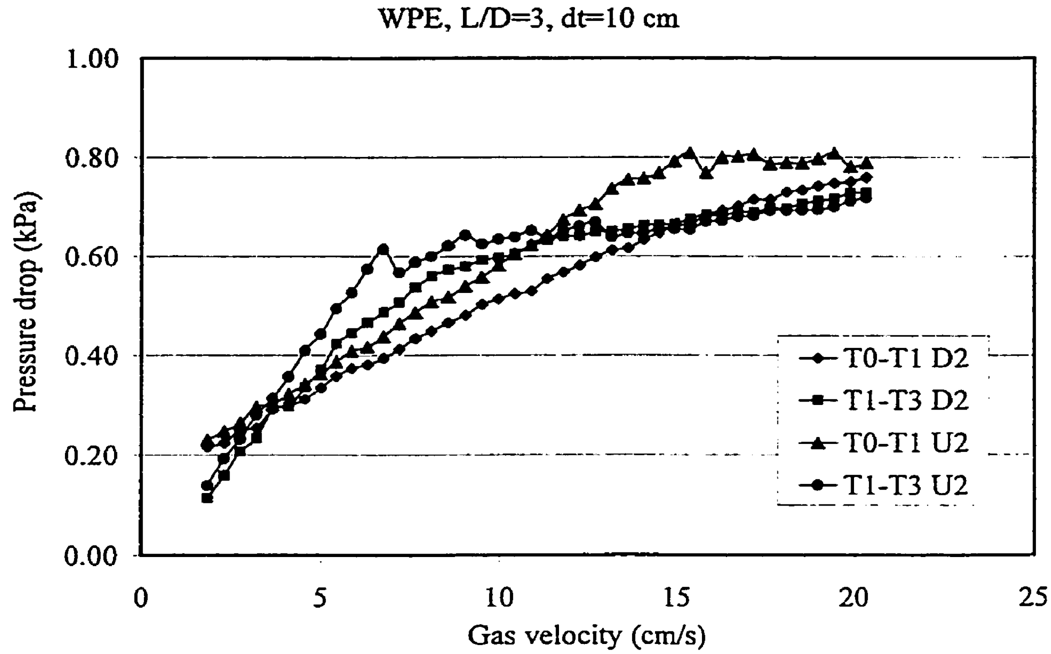

(a)

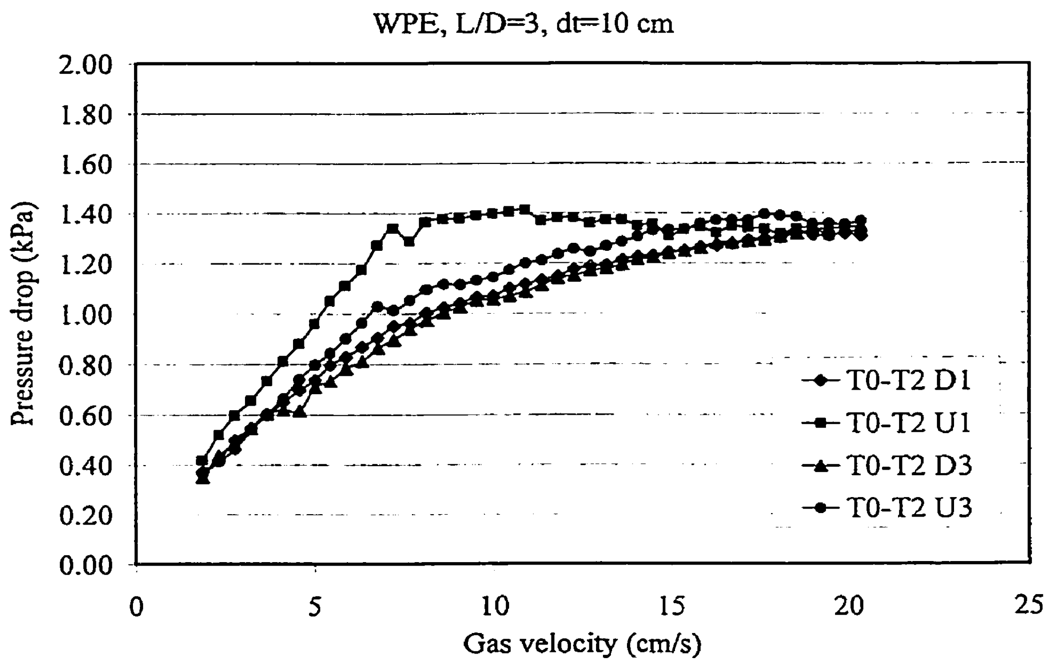

(b)

Figure 3.8. Minimum fluidization velocity plots for WPE-air system, U_{mf}=7.1 cm/s

U1, U2 and U3: increasing velocity

D1, D2 and D3: decreasing velocity

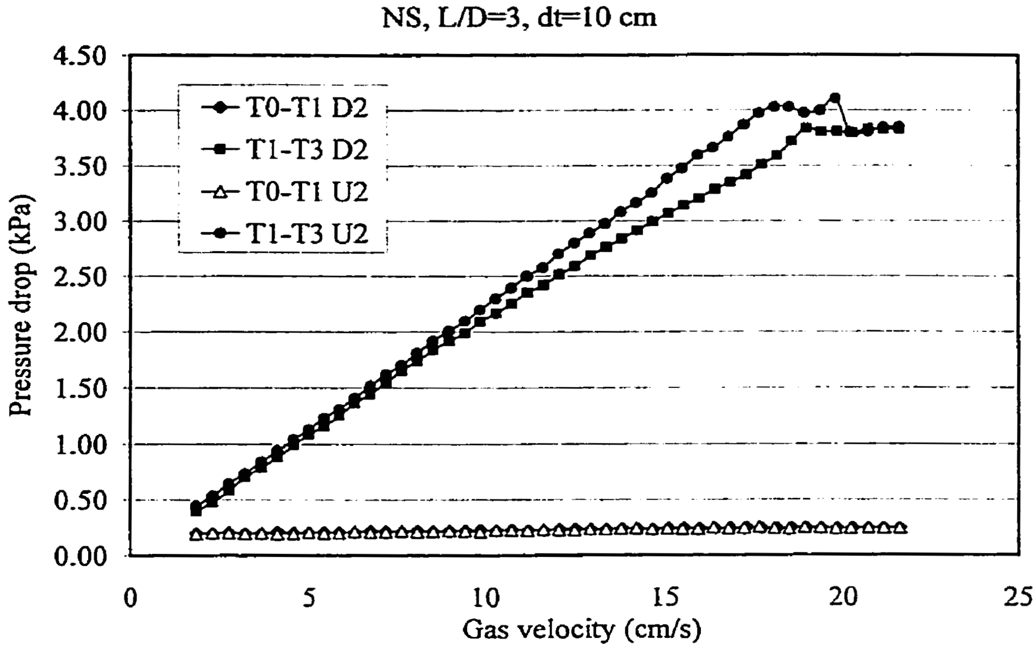

(a)

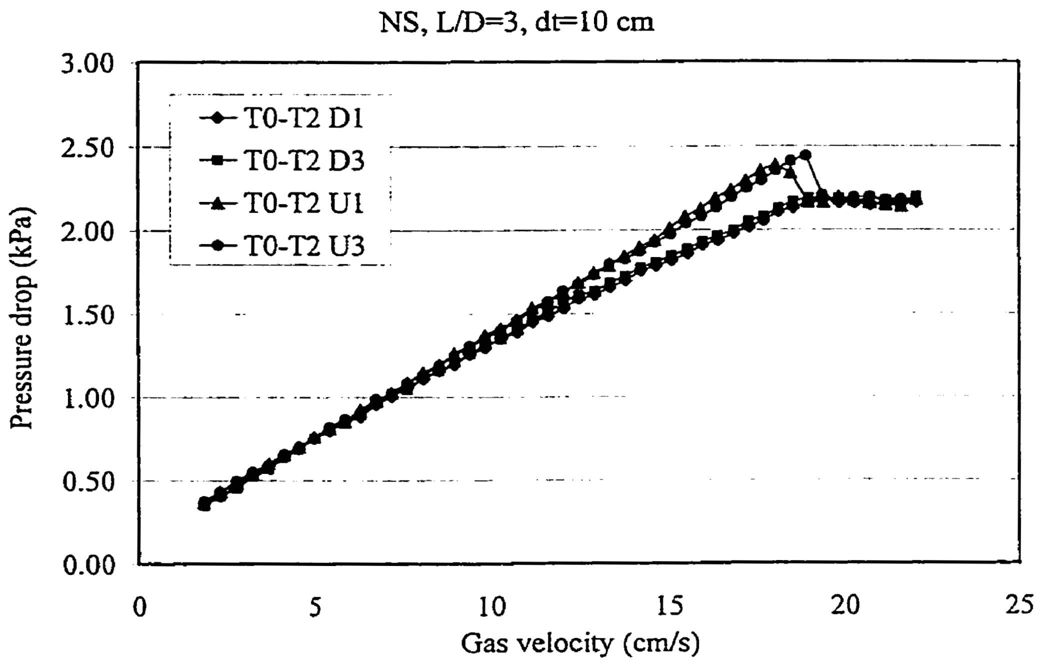

(b)

Figure 3.9. Minimum fluidization velocity plots for NS-air system, U_{mf}=18.5 cm/s

U1, U2 and U3: increasing velocity

D1, D2 and D3: decreasing velocity

3.2.2. X-ray Imaging Experiments

The rotameters used for the X-ray imaging experiments were the same as those used in the minimum fluidization velocity measurements as listed in Table 3.1. The operating pressure of the rotameter was 549.7 kPa (80 psig) for NPE-air system, 137.4 kPa (20 psig) for WPE-air and NS-air system. The X-ray imaging experiments were carried out at different superficial gas velocities, as shown in Table A.1 (Appendix A) for each kind of particle. The procedure for the X-ray imaging experiments is described below.

1. Vacuum the inside wall of the column to clean away the residue of other kind of particles from the column wall and the distributor plate.
2. Fix the column on a stand.
3. Make sure that the unused taps are plugged and the sampling port valves are closed.
4. Charge the column with the particles to the desired bed height which is L/D=3 in this study.
5. Install the expansion section onto the column body and attach it to a cyclone. Check if the hose is firmly secured to the top of the column.
6. Assemble air feed system. Choose an appropriate rotameter for the air velocities to be used.
7. Move the settled fluidized bed to the position between X-ray tube and Image intensifier (see Figure 3.1). Check if the column is vertical.
8. Fluidize the bed for two hours to remove packing effects. After the two hours fluidization, allow the bed to rest for half hour.
9. Connect VCR to X-ray camera and monitor to view the picture directly.
10. Turn on the air system and adjust the rotameter to the desired reading for each superficial gas velocity.
11. Turn on the GE MPX 100 fluoroscopy system to record the real time speed images on videotape for later digitizing and image processing.

The recorded video signals were digitized by playing the videotape on a VHS VCR and sending the video-out signal to the composite video input port on a Personal Video Board (also known as the Video I/O Option) on an SGI O2 workstation. SGI mediarecorder software was used to conduct the digitization process. Thousands of image frames were obtained, at a rate of 30 frames/s. Figures 3.10, 3.11 and 3.12 show some typical sequential sample X-ray image frames at a speed of 30 frames/s for NS-air, NPE-air and WPE-air system, respectively. The frame size is 640×480 pixels. It can be seen that there is a large circle in each frame, which is the X-ray imaging area. Part of the fluidized bed is shown in the image frames. Due to the limitation that the X-ray imaging area is not large enough to cover the entire fluidized bed, images of the top and bottom sections of the fluidized bed had to be taken separately. From these sequential pictures one can see the column wall clearly. Inside the column wall, the brighter areas represent the bubbles and the darker areas represent the emulsion phase, also called the background of the image frames. Bubbles are moving up from one frame to another. The bubble shape changes as the bubble is moving up. It is clear that the bubble shape is not always spherical as assumed in Davidson's model (Kunii and Levenspiel, 1991).

One should note that the bubbles in the images shown in Figures 3.10, 3.11 and 3.12 are not very clear. Image enhancement, segmentation and representation are needed for each image frame. Bubble tracking can then be performed with bubble marking. Bubble marking means giving a number to each bubble and counting pixels for each bubble. Then bubble size, velocity, occurrence frequency and volume fraction will be obtained at each operating condition. All of these operations are called image processing which will be discussed in next chapter.

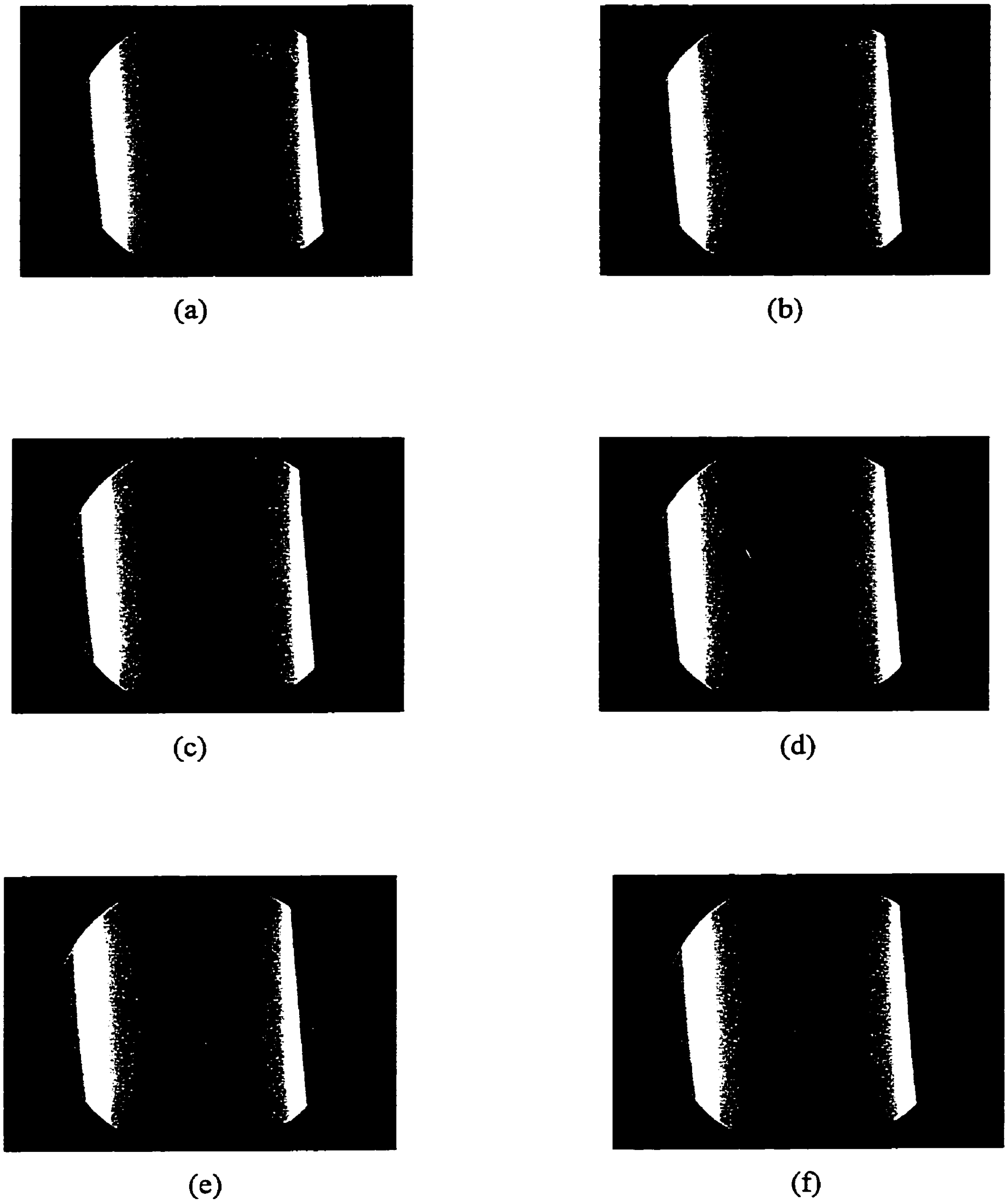

Figure 3.10. X-ray image frames obtained in NS-air fluidized bed

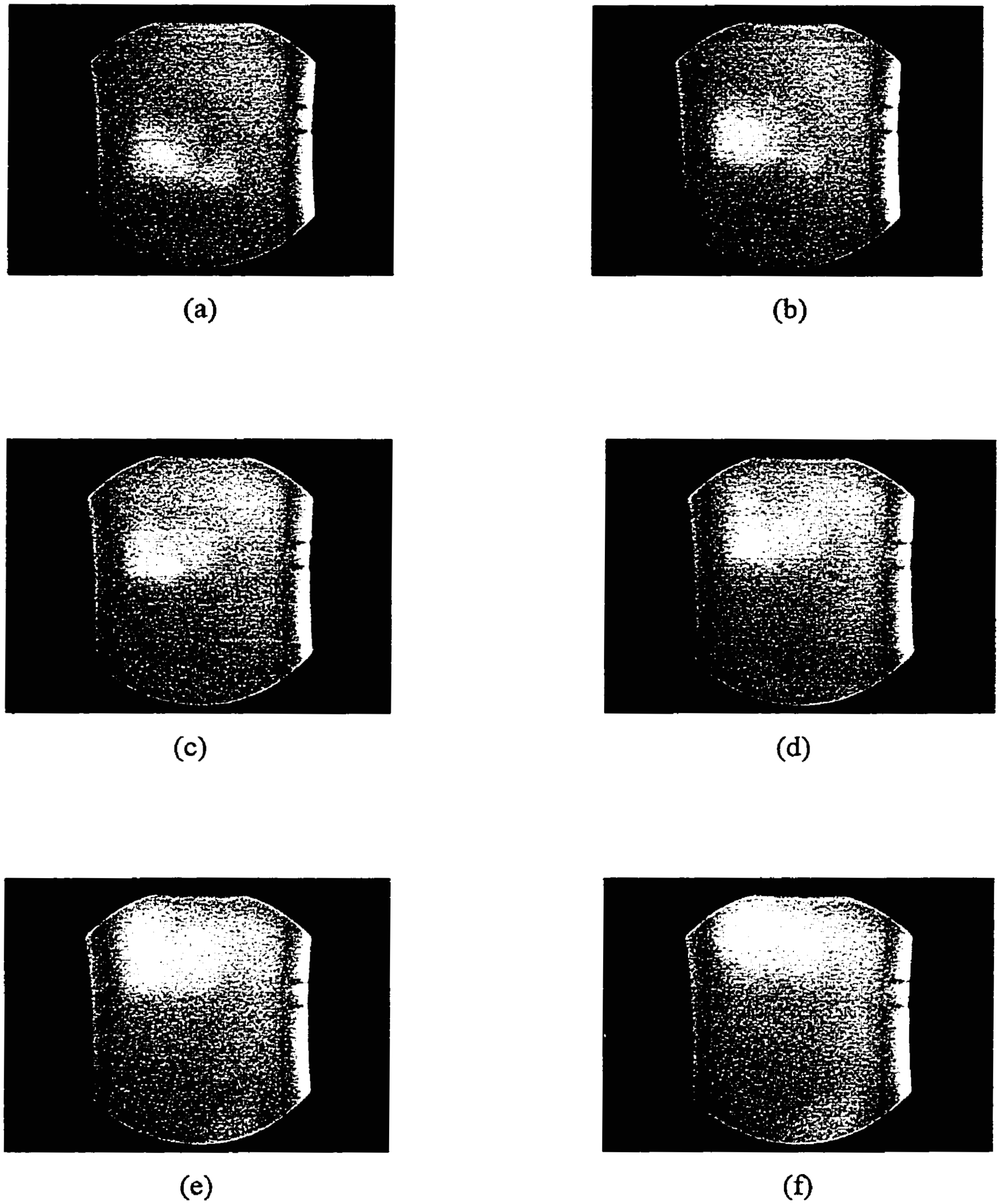

Figure 3.11. X-ray image frames obtained in NPE-air fluidized bed

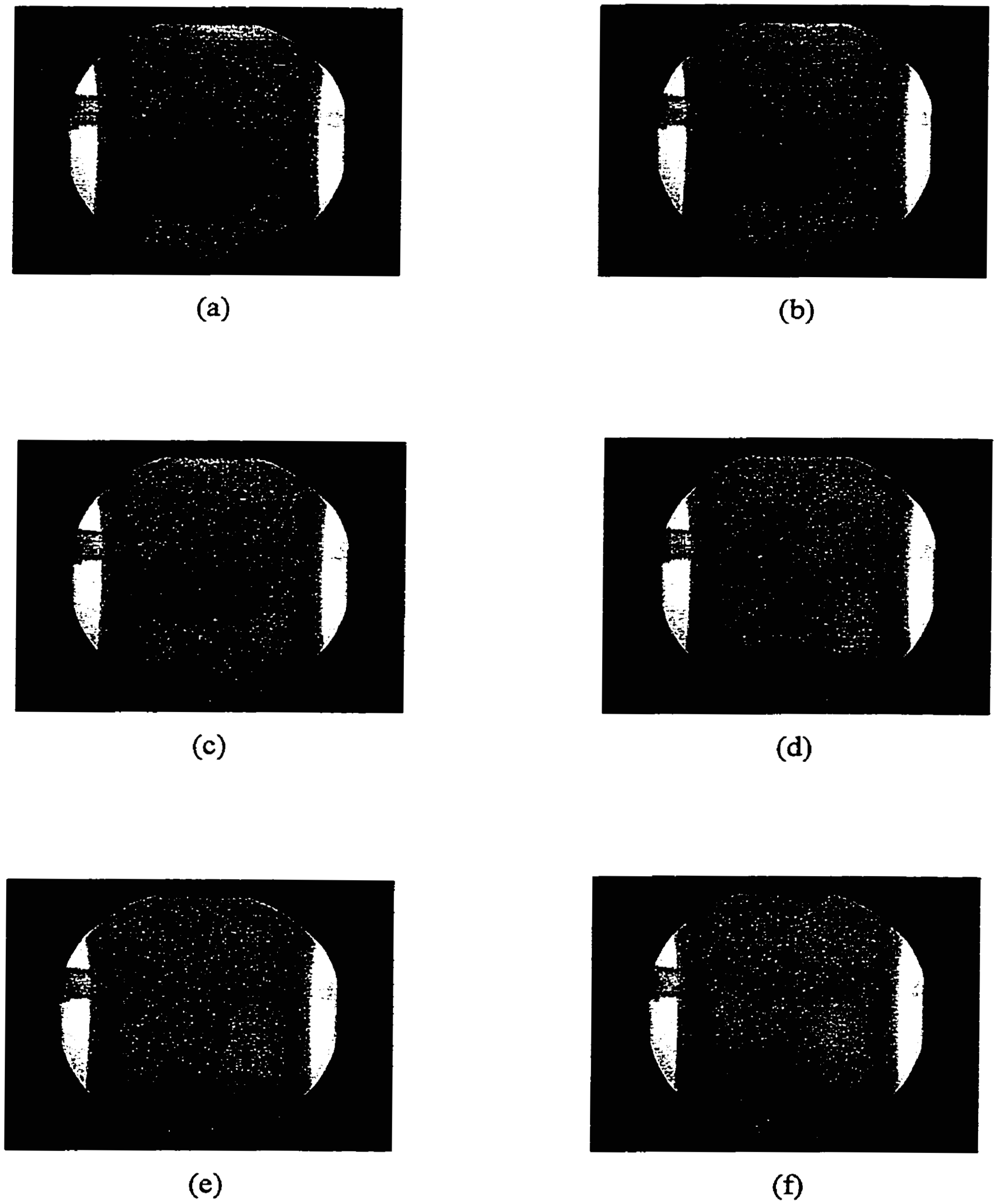

Figure 3.12. X-ray image frames obtained in WPE-air fluidized bed

CHAPTER 4
IMAGE PROCESSING

Interest in digital image processing techniques can be dated back to the early 1920's (Gonzalez *et al.*, 1977, 1992) when pictures of world news events were first transmitted by submarine cable between New York and London. Application of digital image processing concepts, however, did not become widespread until the middle 1960's when third-generation digital computers began to offer the speed and storage capabilities required for practical implementation of image processing algorithms. Since then, this area has experienced vigorous growth, having been a subject of interdisciplinary study and research in such fields as engineering, computer science, information science, statistics, physics, chemistry, biology and medicine. The results of these efforts have established the value of image processing techniques in a variety of problems ranging from restoration and enhancement of space-probe pictures to processing of fingerprints for commercial transactions.

In digital image processing, the image refers to a two-dimensional light intensity function $f(x, y)$, where x and y denote spatial coordinates and the value of f at any point (x, y) is proportional to the brightness (or gray level) of the image at that point. A digital image is an image $f(x, y)$ which has been discretized both in spatial coordinates and in brightness. We may consider a digital image as a matrix whose row and column indices identify a point in the image and the corresponding matrix element value identifies the gray level at that point. The elements of such a digital array are called image elements or pixels. The size of digital image can vary with the application.

Digital image processing encompasses a broad range of hardware, software and theoretical understanding. To perform image processing several fundamental steps are required, as shown in Figure 4.1. A digitizer converts an image into a numerical representation (digital image) to be the input into a digital computer. Systems used for image processing range from microprocessor devices for special purpose applications to large systems capable of performing a variety of functions. Image processing computer programs are often coded for different purposes. Some commercial image processing software has been used by Mudde *et al.* (1994) to study bubble dynamics in fluidized beds. However, even when assisted by this software, the analysis was still executed manually. Continuous measurements frame by frame, especially continuous bubble tracking for bubble velocity measurements have not been found in the open literature. In image processing, automatically tracking features of an object is difficult because the features are continually evolving and interacting (Silver and Wang, 1996).

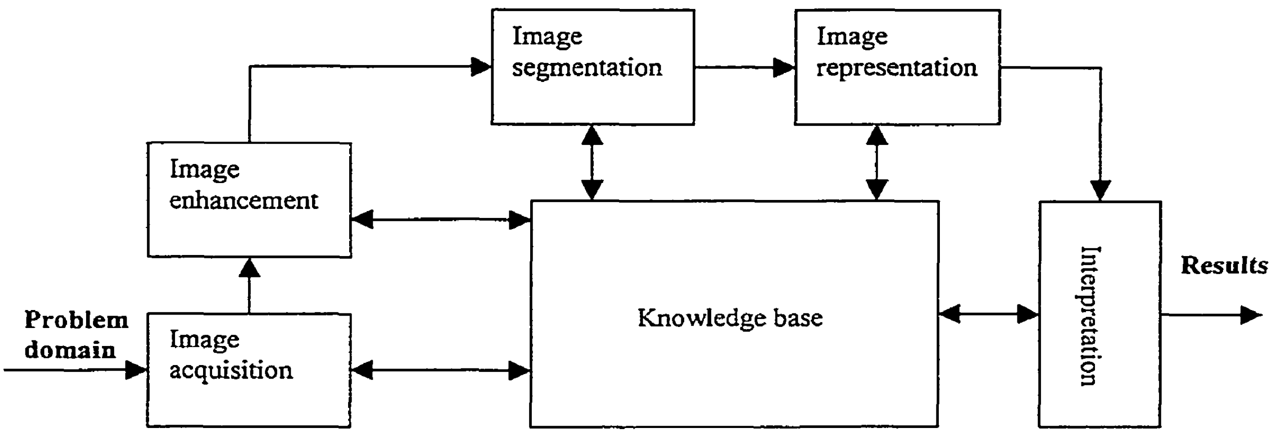

Figure 4.1. Steps for digital image processing

In this study, SGI mediarecorder software was used to digitize the composite video input signal acquired with a Personal Video board (also known as the Video I/O Option) on an SGI O2 workstation provided by Dr. Doug Phillips (Information Technologies, University of Calgary). Thousands of image frames at a temporal resolution of 30 frames/s were obtained by digitizing. Digitized image files were then compressed and backed-up on CDs for further processing. An image processing software package written in FORTRAN and UNIX shell scripts was developed for X-ray image processing of bubbles in fluidized beds. This package can be used for bubble tracking to measure bubble size, velocity and occurrence frequency, bubble volume fraction etc., sequentially and automatically. Since digitized image arrays need a lot of computer space an adequate and efficient computer storage capability has to be provided. For the current work, an IBM-RS/6000 model H70 computer (UNIX system) was used to perform the bubble image processing. Display is necessary to view the image pictures. For this purpose, a software package called XV created by John Bradley (Bradley, 1998) for viewing image pictures, and a computer monitor with high resolution were employed.

By using the developed image processing software package, bubble tracking measurements were executed for images obtained at 11 operating conditions in gas fluidized beds with NS-air, NPE-air and WPE-air systems, which are shown in Table 4.1. Because of a limitation of the imaging system the images of the entire fluidized bed can not be taken at the same time. Instead, images were taken at the top and bottom sections of the fluidized bed separately, with the height of each section being about 20 cm.

Image processing in this study consists of the following four steps:

- rotating and cropping image frames;
- image enhancement-subtracting image background;
- image segmentation and representation-smoothing, filtering and thresholding;
- bubble marking and tracking.

These four steps are discussed in detail in the following sections.

4.1. Rotating and Cropping

As mentioned above, the term digital image refers to a two dimensional light intensity function $f(x, y)$ and the value of f at spatial coordinates (x, y) gives the intensity (brightness) of the image at that point (Gonzalez *et al.*, 1977). Intensity number is non-negative in each digital image. The $f(x, y)$ can be arranged in the form of an array as shown in Equation (4.1), where each element of the array is a discrete quantity. Each element of the right hand side of this equation is referred to as an image pixel.

Table 4.1. Image processing work list

Solids	Superficial gas velocities cm/s	Number of frames	Number of bubbles	Fluidized bed height (cm)
NS-bottom	U=35.2 $\cong 2.0\times U_{mf}$	328	805	
NS-bottom	U=52.8 $\cong 3.0\times U_{mf}$	312	551	
NPE-bottom	U=17.6 $\cong 2.0\times U_{mf}$	517	500	41
NPE-bottom	U=21.6 $\cong 2.5\times U_{mf}$	339	570	45
NPE-bottom	U=28.8 $\cong 3.0\times U_{mf}$	339	550	47
NPE-top	U=13.2 $\cong 1.5\times U_{mf}$	457	244	39
NPE-top	U=17.6 $\cong 2.0\times U_{mf}$	553	513	41
NPE-top	U=21.6 $\cong 2.5\times U_{mf}$	293	647	45
WPE-top	U=14.4 $\cong 2.0\times U_{mf}$	561	449	33
WPE-top	U=18.0 $\cong 2.5\times U_{mf}$	667	841	40
WPE-top	U=21.6 $\cong 3.0\times U_{mf}$	572	541	42

$$f(x,y)=\begin{bmatrix} f(0,0) & f(0,1) & . & . & . & f(0,M-1) \\ f(1,0) & f(1,1) & . & . & . & f(1,M-1) \\ . & & & & & \\ . & & & & & \\ . & & & & & \\ f(N-1,0) & f(N-1,1) & . & . & . & f(N-1,M-1) \end{bmatrix} \tag{4.1}$$

The edge area of the digital image as shown in Figures 3.10, 3.11 and 3.12, which is outside of the column, should be cut off before further image processing. It is also noted that some images are tilted and therefore rotating of the images is required. To resolve these problems, a UNIX shell script program was developed by modifying one written by Dr. Doug Phillips (Information Technologies, University of Calgary). The shell script calls routines from the PBMPLUS package developed by Jef Poskanzer to rotate the frame to the correct position and to crop the edges. An updated version of the PBMPLUS package is freely available on the Internet under the name NETPBM.

The rotating and cropping operations are illustrated in Figure 4.2. As noted in the diagram, rotation changes the image intensity values slightly due to interpolation effects.

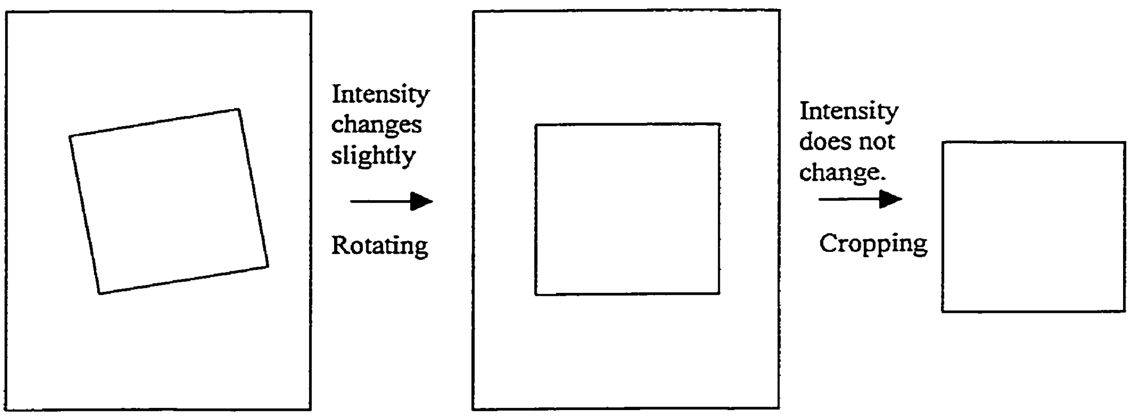

Figure 4.2. Diagram for rotating and cropping operation

A typical digitized image is shown in Figure 4.3a. The edges of the image beyond the inside wall of the column were cut off. The top and bottom edges of the image were also cropped off. The cropped image was then also rotated by 2° in the clockwise direction. The cropped and rotated image is shown in Figure 4.3b. Similar rotating and cropping operations were also performed for the image shown in Figure 4.4a to get the cropped and rotated image shown in Figure 4.4b. For each data set in this study as shown in Table 4.1, consisting of from 293 to 667 frames each, the rotating and cropping processing was conducted continuously and automatically for each data set. The operation of rotating and cropping was performed at a speed of about 4 frames processed per second in the IBM-RS/6000 model H70 computer.

4.2. Image Enhancement -Subtracting Image Background

Usually, images directly obtained from digitization are not clear enough. They need further processing. There are many approaches for image enhancement. Subtracting the image background is one of them. The principal objective of various enhancement techniques is to process a given image so that it is more suitable than the original one for a specific application. In this study, a computer program was developed to do subtraction of image background. Since sand particles and polyethylene particles have different densities, their X-ray attenuation properties are different. Therefore, the subtraction of image background for the sand-air system is different from that for the polyethylene-air system, which will be discussed separately in the following two sub-sections.

4.2.1. Sand -Air System

The background of the digital image in Figure 4.3 is brightened at the right and left side edges. That is caused by the X--ray attenuation through the cylindrical NS-air fluidized bed column as illustrated in Figure 4.5.

Assuming the Beer-Lambert law (Equation (2.1)) applies to X-ray attenuation through a gas-solid fluidized bed column, the transmitted intensity can be expressed in Equation (2.2), represented here for convenience.

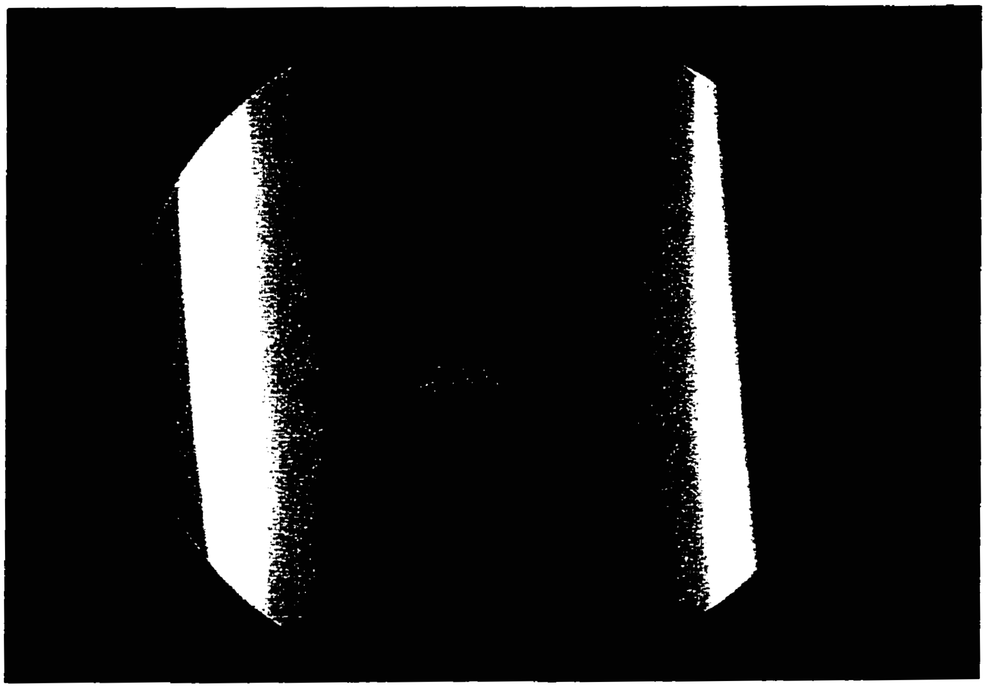

(a) Before cropping and rotating

(b) After cropping and rotating

Figure 4.3. Example for rotating and cropping (NS) (frame 19)

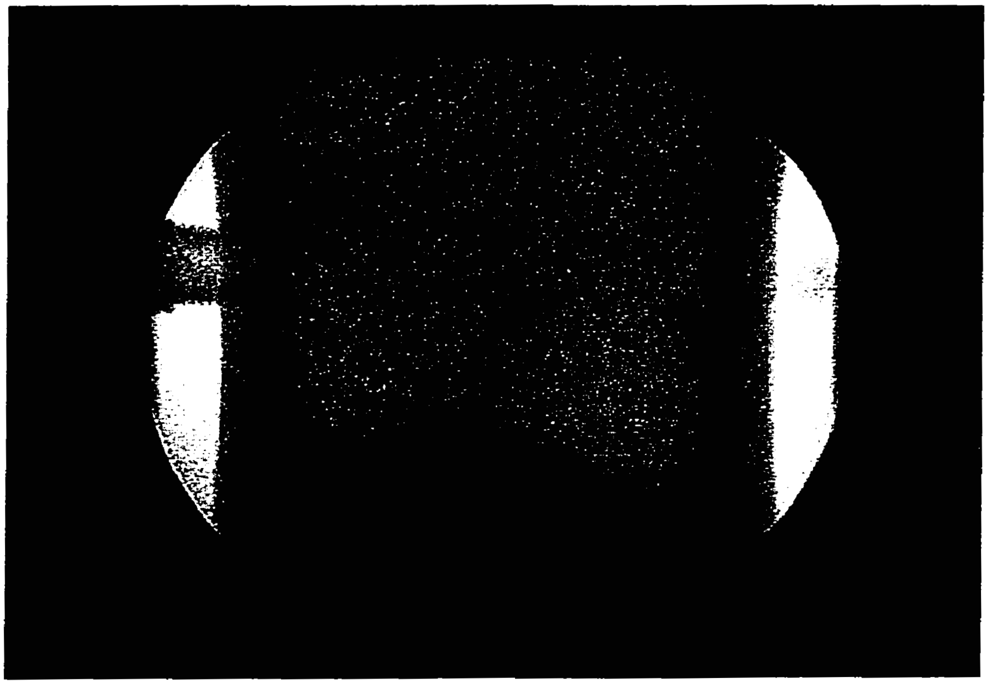

(a) Before cropping and rotating

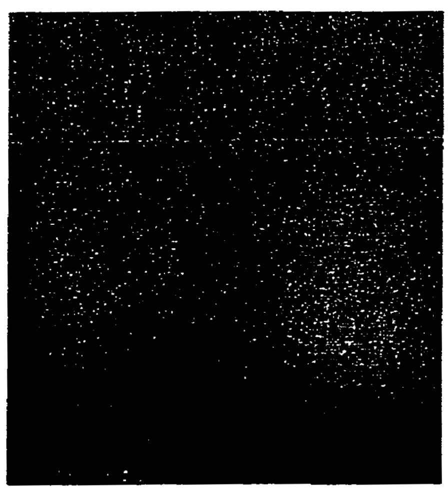

(b) After cropping and rotating

Figure 4.4. Example for rotating and cropping (WPE) (frame 9)

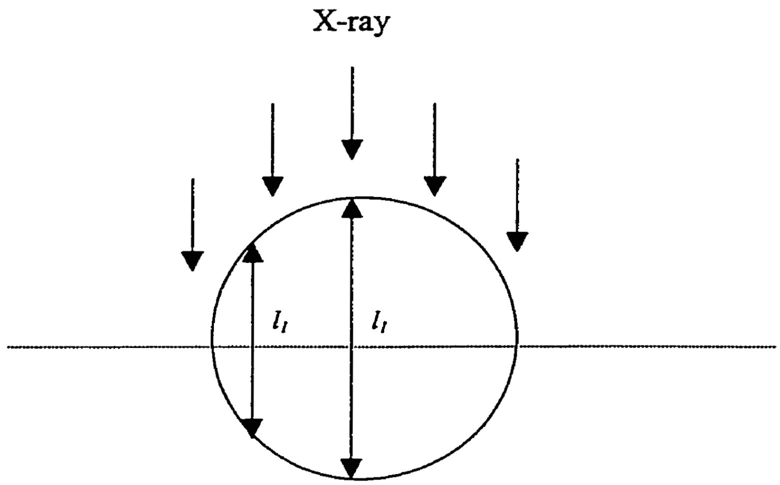

Figure 4.5. X-ray passing through the column

$l_1<l_2 \Rightarrow I_1>I_2$

$$I = I_0 \exp[-(\mu_g \rho_g \varepsilon_g + \mu_s \rho_s (1-\varepsilon_g))l] \tag{4.2}$$

For a given imaging system and a given fluidized bed, if the incident intensity is fixed, the transmitted intensity is a function of density ρ_g, path length l and holdup of the individual phases. As seen in Table 3.2, The density of sand particles is about four times as high as that of polyethylene particles. Compared to the effect of polyethylene particle density, the effect of sand particle density on X-ray attenuation through the column is more significant.

In Equation (4.6), if the incident intensity I_0, the density of the material and holdup of the individual phase are fixed, the transmitted intensity will be a function of path length only. This is the reason that the background of the image in Figure 4.3 has a change of brightness from center to both right and left edges. Since the column is cylindrical the path length through attenuating materials along a chord near the edge is less than that through the center. In order to remove this cylindrical shape effect, a background has to be subtracted from each image during image processing. Figure 4.6 is an averaged background over 3 image frames obtained at the same superficial gas velocity for NS-air system. During image processing for NS-air system, the image background for a given set of frames was subtracted from each image in that set by running the subtracting image background program. Figure 4.7 is the image frame after subtracting background for the image frame shown in Figure 4.3b.

4.2.2. Polyethylene -Air System

For the polyethylene-air system, the background of the digital image in Figure 4.4 does not have uniform intensity distribution. The top part is brighter and the bottom part is darker. Two possible reasons are:

- gradient change in emulsion phase density along the fluidized bed height.
- artificial error of the fluoroscopy system.

To investigate the second reason, blank experiments were conducted using the same experimental set up. While polyethylene particles were inside the column, X-ray images were taken without air flowing. The images were then digitized and analyzed. Figure 4.8 shows one of the images obtained from blank experiments. Figure 4.9 is the plot of intensity number variation along one column of the image array for the same image shown in Figure 4.8. One can see from Figure 4.9 that the intensity number increases from the bottom to the top of the image, indicating an artificial error caused by the fluoroscopy system. Otherwise, the intensity number should be approximately constant along the bed height.

In order to remove the effects of emulsion phase density and artificial errors, an averaged background image for each data set of polyethylene-air system was created by averaging a number of image frames that do not contain bubbles. Figure 4.10 illustrates an averaged background frame obtained with the WPE-air system. Figure 4.11 is the image after subtracting background for the image shown in Figure 4.4b.

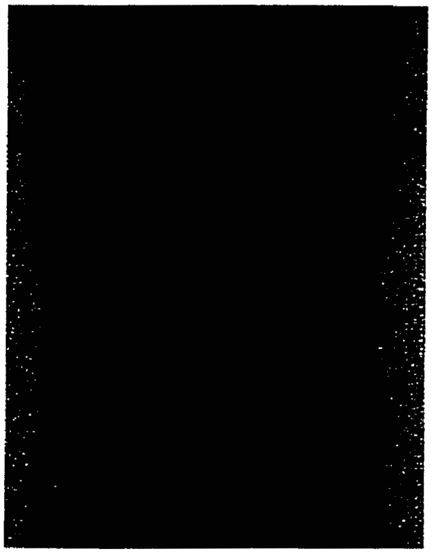

Figure 4.6. Averaged image background for NS-air system

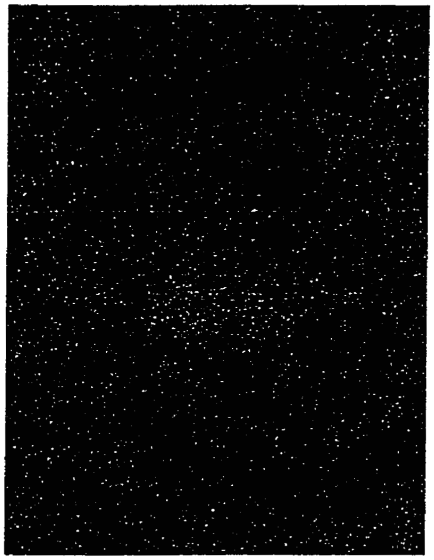

Figure 4.7. Image frame after subtracting background of the same image frame shown in Figure 4.3(b)

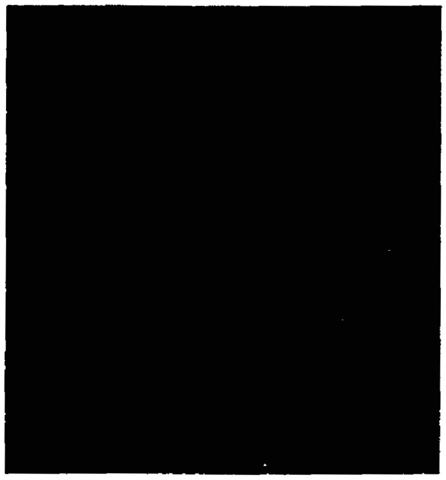

Figure 4.8. Image frame from blank experiments

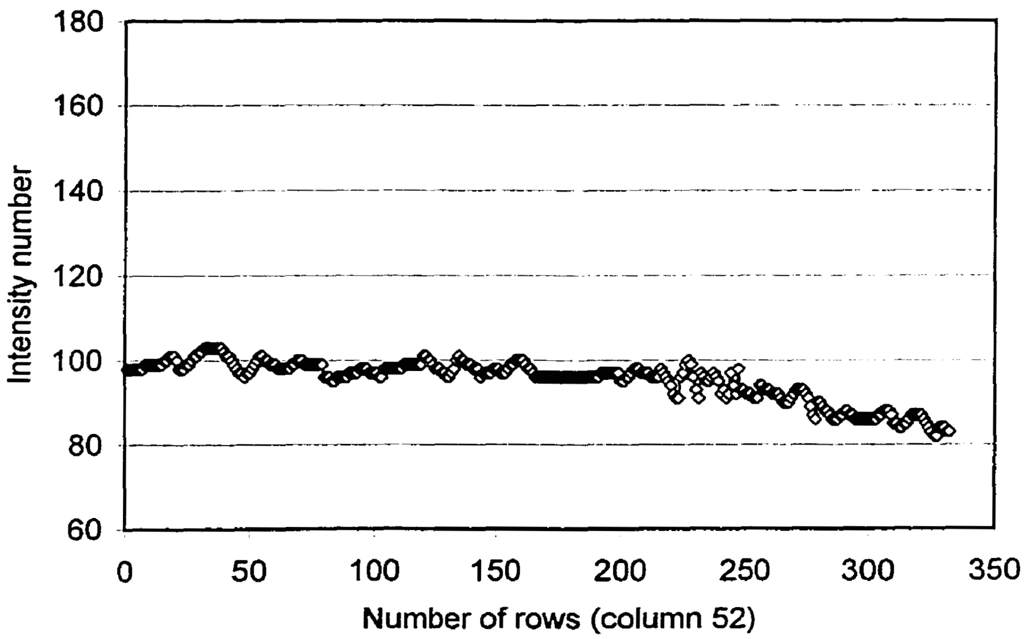

Figure 4.9. Intensity number variation along the column height (blank experiments) (The left-hand side is the top of the image and the right-hand side is the bottom of the image)

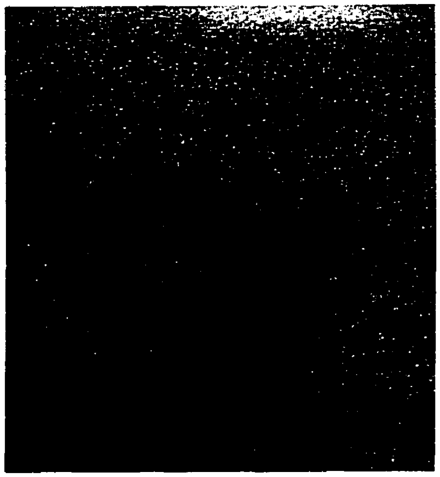

Figure 4.10. Averaged image background for WPE-air system

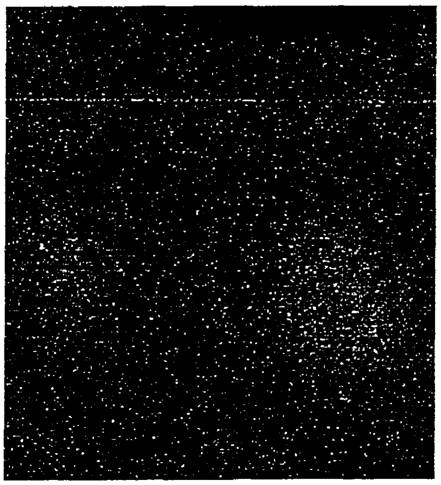

Figure 4.11. Image frame after subtracting background for the same image frame shown in Figure 4.4 (b)

4.3. Image Segmentation and Representation - Smoothing, Filtering and Thresholding

Gonzalez and Woods (1993) discussed image segmentation in details in their book. Image segmentation subdivides an image into its constituent parts or objects. The level to which this subdivision is carried out depends on the problem being solved. Segmentation should be terminated when the objects of interest in an application have been isolated. In this study a computer program was developed to do smoothing, filtering and thresholding of images. In professional image processing work, smoothing is an approach to image segmentation. Normally, smoothing operations are used primarily for diminishing spurious effects that may be present in a digital image as a result of a poor imaging system. There are several techniques for image smoothing. Neighborhood averaging (Gonzalez *et al.*, 1992) is a straightforward one. In this particular bubble imaging study, since the edge of each bubble area in the image frames needs to be smoother than the original the 4-pixel neighborhood averaging technique was used. Given an image $f(x, y)$, the procedure generates a smoothed image $g(x, y)$ whose value at each pixel is obtained by averaging the 4 pixels as shown in Figure 4.12. Mathematically the smoothing/ averaging process can be represented by

$$\begin{aligned} g(x,y) &= g(x+1,y) = g(x,y+1) = g(x+1,y+1) \\ &= [f(x,y)+f(x+1,y)+f(x,y+1)+f(x+1,y+1)]/4 \end{aligned} \quad (4.7)$$

where

$y=0, 2, 4, 6, \ldots\ldots\ldots M$

$x=0, 2, 4, 6, \ldots\ldots\ldots N$

In this study, "filtering" refers to bubble size filtering. Since some noise was generated in the image during X-ray imaging, bubble size filtering was performed to remove the noise. In addition, unstable small bubbles that are not considered as bubbles in this work were also removed by filtering. Figure 4.13 shows the determination of 170 pixels as a bubble size threshold for filtering images of NPE-air system at bottom section of the bed at

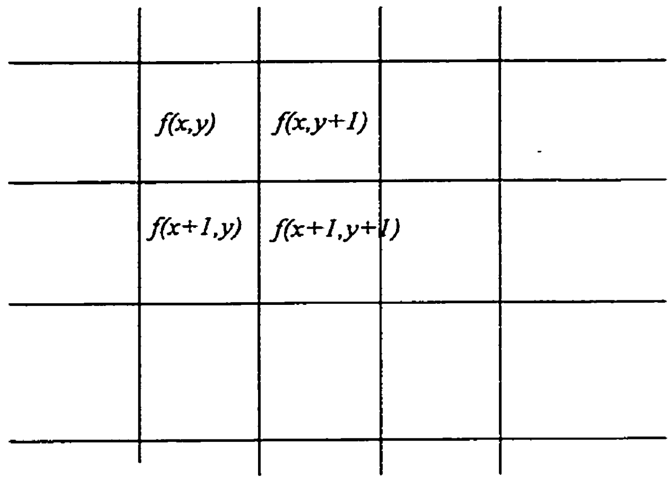

Figure 4.12. Pixel averaging 2 by 2

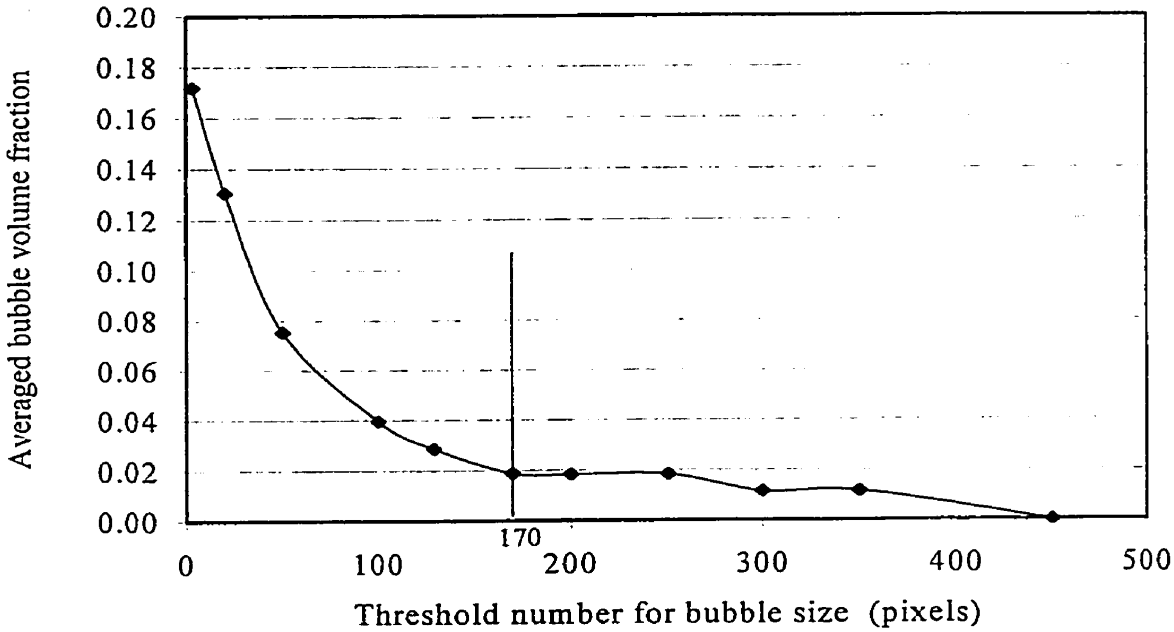

Figure 4.13. Determination of bubble size threshold

superficial gas velocity of 21.6 cm/s. From Figure 4.13 one can see that 11 different bubble size numbers were tested for this data set by inspecting all frames in this image set. With the increase in the number of pixels as filtering bubble size threshold, bubble volume fraction decreases significantly at the beginning, and then becomes relatively constant from number of 170, which was assumed to be the filtering bubble size threshold for this data set. Similar processes were applied for all other data sets in this study.

In the current research work, the image intensity thresholding was performed to extract the objects (bubbles) from the background (emulsion phase). Intensity thresholding is one of many image segmentation approaches. In order to perform intensity thresholding in this work, various investigations have been conducted in this study. A global intensity thresholding method (Gonzalez and Woods, 1993) in which intensity data in an image are plotted into a histogram, was tested at first. Unfortunately, this method was not successful in this work due to the small intensity value difference between image background and bubble area. Finally, intensity thresholding was performed by analyzing intensity data in the way shown in Figures 4.14 and 4.15. These two figures are sample plots for determining the intensity threshold for WPE-air system at superficial gas velocity of 14.4 cm/s. Figure 4.14 shows the intensity number variation in column 194 in image frame 23 after subtracting the background. From the figure, the intensity threshold was subjectively determined as 134. Other people may choose another number, for example, 133. Even in global thresholding method (Gonzalez and Woods, 1993) there is subjectivity in the threshold determined from the histogram. Figure 4.15 shows the intensity number variation in column 32 in image frame 9 of the same set after subtracting background. From this frame, an intensity threshold was determined as 136. In this work, three to nine image frames were selected randomly for intensity thresholding for each data set. For this operating condition (WPE-air, superficial gas velocity of 14.4 cm/s), six frames were tested and the averaged intensity threshold was taken as 135. Smoothing, filtering and thresholding were performed for all the 11 data sets as shown in Table 4.1. Figure 4.16 and 4.17 are typical examples of images after smoothing, filtering and thresholding.

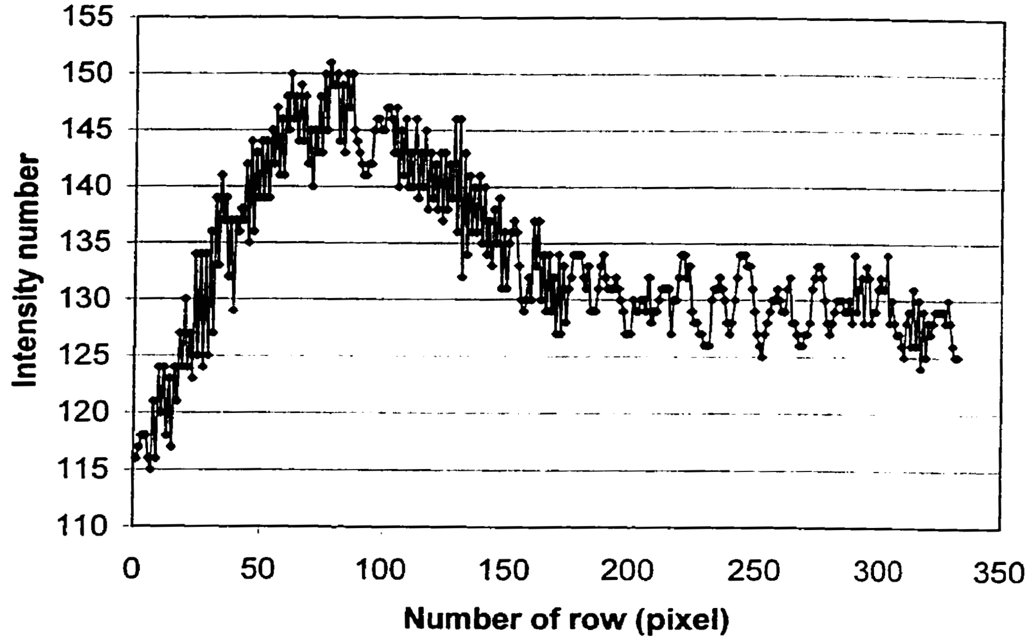

Figure 4.14. Intensity number variation with number of row for column 194 in frame 23

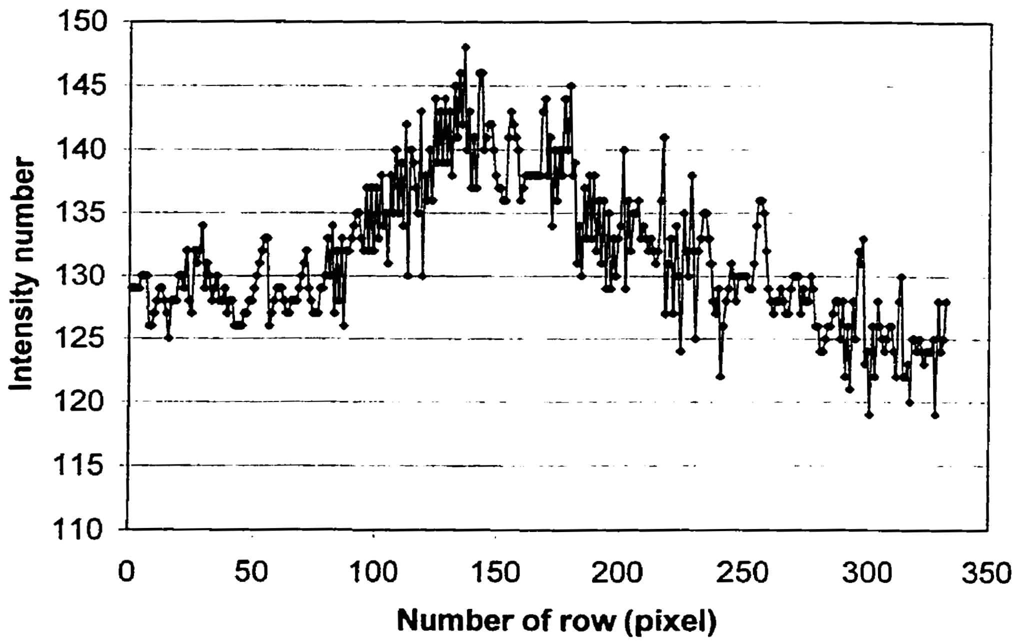

Figure 4.15. Intensity number variation with number of row for column 32 in frame 9

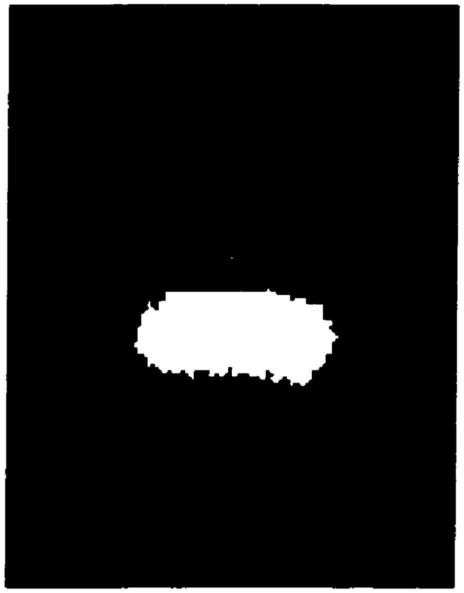

Figure 4.16. Image frame after smoothing, filtering and thresholding for the same frame shown in Figure 4.7

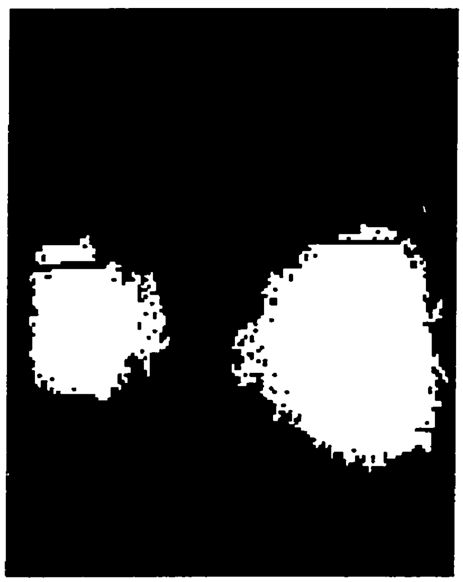

Figure 4. 17. Image frame after smoothing, filtering and thresholding for the same frame shown in Figure 4.11

4.4. Bubble Marking and Tracking

In the software package developed in this study, a computer program can perform bubble tracking to determine bubble size, bubble vertical and horizontal velocities, bubble occurrence frequency and bubble volume fraction, sequentially and automatically. During bubble tracking and marking, bubble coalescence and break-up were taken into account. Figure 4.18 shows a series of sequential image frames, at an interval of 33 ms, that show the process of bubble coalescence and break-up. In Figure 4.18 (c), 4.18 (d) and 4.18 (e) the bubble at the top of the frame breaks up while in Figure 4.18 (f), 4.18 (g) and 4.18 (h), 4.18 (i) the coalescence of the two bubbles at the top of the frame occurs. In this figure the numbers show how bubble coalescence and break-up are considered in the bubble tracking and marking program. When a complicated case happens such as Figures 4.18 (g) to 4.18 (h) the bubble tracking and marking program will judge the velocities of other bubbles first in order to satisfy that the bubble rising velocities are always positive. After several times of judgement, the program will give a number to each bubble. It should be pointed out that in one image set, about 95% of the bubbles were marked and tracked correctly by the program by counting every frame in one image set manually. In Figure 4.18 (h) the bubble marked as bubble 4 is not correct. This can explain why some bubble velocity data in image processing results are unreasonable some figures that will be discussed in Chapter 5. Modification of the bubble tracking and marking program is recommended for future work.

The bubble tracking and marking computer program marks all the bubbles present in an image frame. However, a portion of a bubble at the top edge or bottom edge of the frame, is not counted in the program. The marking strategy is marking bubbles from top to bottom and from left to right of the frame. Bubbles in the first frame are identified as bubble 1, bubble 2 and so on. The total number of pixels multiplied by pixel size is counted as the original cross sectional area of the bubble. Assume that bubbles are spherical and their silhouettes are circular, then the bubble diameter can be calculated by the following simple equation:

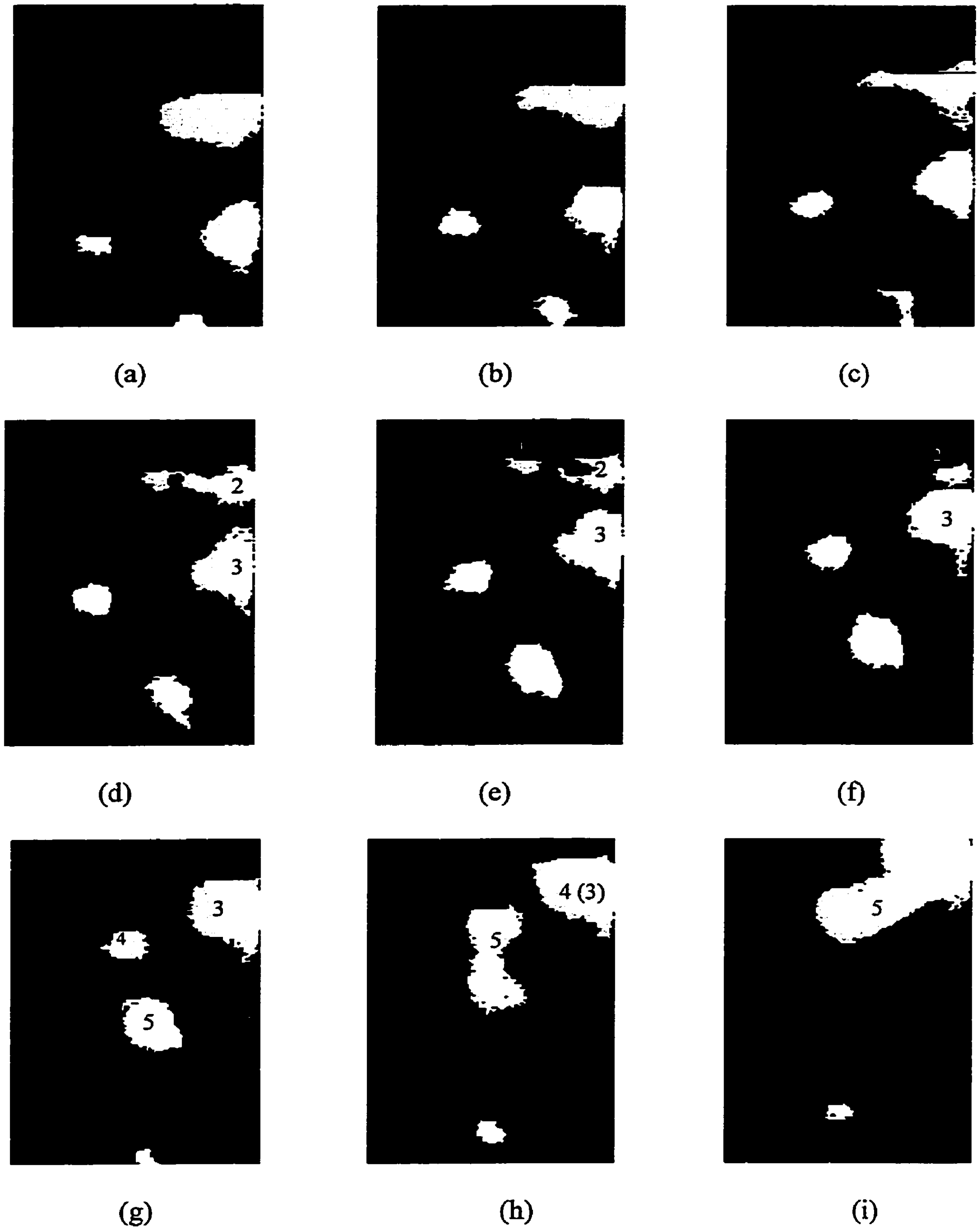

Figure 4.18. Image frames with bubble coalescence, break-up and new bubble occurrence with NS-air system, U=35.2 cm/s

$$d_b = \sqrt{\frac{4A}{\pi}} \tag{4.8}$$

where d_b is the bubble diameter, A is the bubble area within the silhouette circle.

The tracking and marking program developed in this study can automatically record the coordinates (x, y) of the bubble center for every bubble in every frame being tracked. The center of a bubble is defined as the geometric center of the original bubble silhouette area as shown in Figure 4.19. For example, the programs record the center coordinate of bubble 1 on the first frame. When the programs track the second frame and if bubble 1 still in the second frame, the center coordinate of bubble 1 is also recorded so that the distance that bubble 1 travels in both vertical and horizontal directions can be calculated. The vertical and horizontal components of velocity of bubble 1 can then be easily computed by dividing the travel distances by the time step between two successive frames, which is 1/30 second in this study. The velocity calculation is illustrated in Figure 4.19.

While the programs created in this work automatically calculate bubble size and bubble velocity they count new bubble occurrence frequency as well. Bubbles coming from the bottom of each image frame are called new bubbles in this bubble image processing. The bubble occurrence frequency is defined as the total number of new bubbles counted for all the frames divided by the time period during which the frames are taken as shown in Equation (4.9).

$$f = \frac{N}{t} \tag{4.9}$$

where

$$t = n \times \frac{1}{r} \tag{4.10}$$

f : bubble occurrence frequency.

n : number of frames tracked.

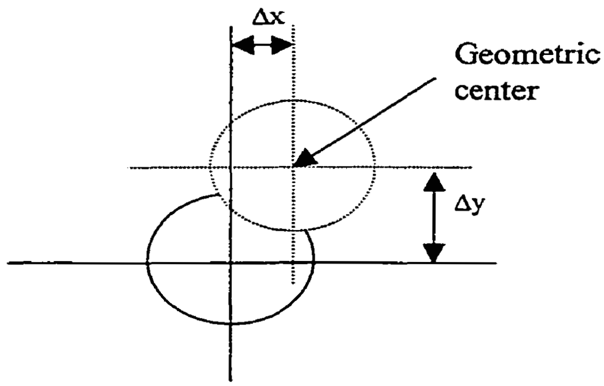

Figure 4.19. Illustration of bubble velocity calculation in image processing

N : total number of new bubbles counted.

r : Frame rate (30 frames/s in this work).

t : time period tracked.

In this study, the bubble volume fraction, f_v, is defined as the ratio of total geometric bubble volume in one frame to the bed volume in the frame after fluidization as shown in Equation (4.11).

$$f_v = \frac{V_{bubble}}{V_{bed}} \tag{4.11}$$

The bubble volume is assumed to be the sphere volume having the same projected area as the bubble measured in the image frames. Figures 4.20 and 4.21 are typical example frames after the bubble tracking and marking operation. As listed in Table 4.1, in most cases the number of bubbles tracked during the image processing is over 500, which is two orders of magnitude larger than sample points collected in the literature. The analysis of the image processing results, including bubble diameter, velocity, occurrence frequency and volume fraction will be conducted in the following chapter.

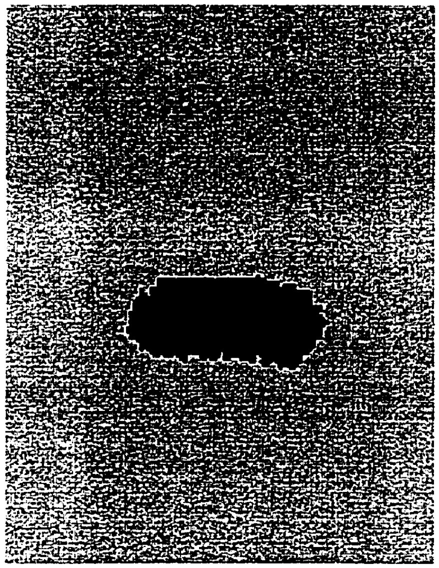

Figure 4.20. Image frame after marking and tracking for the same frame shown in Figure 4.16

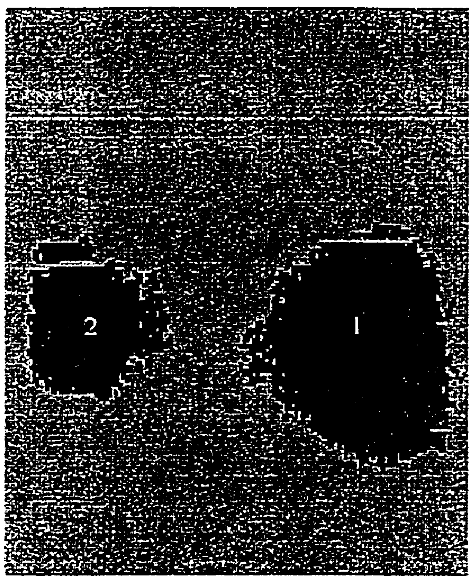

Figure 4.21. Image frame after marking and tracking for the same frame shown in Figure 4.17

CHAPTER 5
ANALYSIS OF RESULTS

Image processing was performed for NPE-air, WPE-air and NS-air fluidized bed systems by using the image processing software developed in this study. The fluidized beds were operated at superficial gas velocities of 13.2 cm/s, 17.6 cm/s, 21.6 cm/s and 28.8 cm/s for the NPE-air system, at 10.8 cm/s, 14.4 cm/s, 18.0 cm/s and 21.6 cm/s for the WPE-air system and at 35.2 cm/s and 52.8 cm/s for NS-air system. Due to the limitation of the image size recorded with the fluoroscopy system, images of the top section and bottom section of the fluidized beds were obtained separately at the same operating conditions.

5.1. Analysis of Bubble Size from Image Processing and Correlations

5.1.1. Analysis of Bubble Size from Image Processing

For NPE-air system, eight sets of images at four different superficial gas velocities, which are $1.5\times U_{mf}$, $2.0\times U_{mf}$, $2.5\times U_{mf}$ and $3.0\times U_{mf}$, were recorded on videotape. No bubble was observed in the images for the bottom section of the bed (close to the distributor) at a superficial gas velocity of 13.2 cm/s ($1.5\times U_{mf}$). Slugging occurred at the top section of the bed (close to the free surface) at a superficial gas velocity of 28.8 cm/s ($3.0\times U_{mf}$). Therefore, the images obtained in these two cases were not processed further. However, image processing was performed for the images obtained at the bottom section of the bed at superficial gas velocity of 28.8 cm/s to investigate the fluid dynamics of bubble flow in this situation.

Figure B.1 (Appendix B) shows the original results of bubble diameters from image processing for the NPE-air system for the bottom section of the bed at the three superficial gas velocities. Figure 5.1.1 illustrates the distribution of bubble size for each of the superficial gas velocities. The number of larger size bubbles increases with increasing superficial gas velocity. From Figure B.1, one can see that with increase in

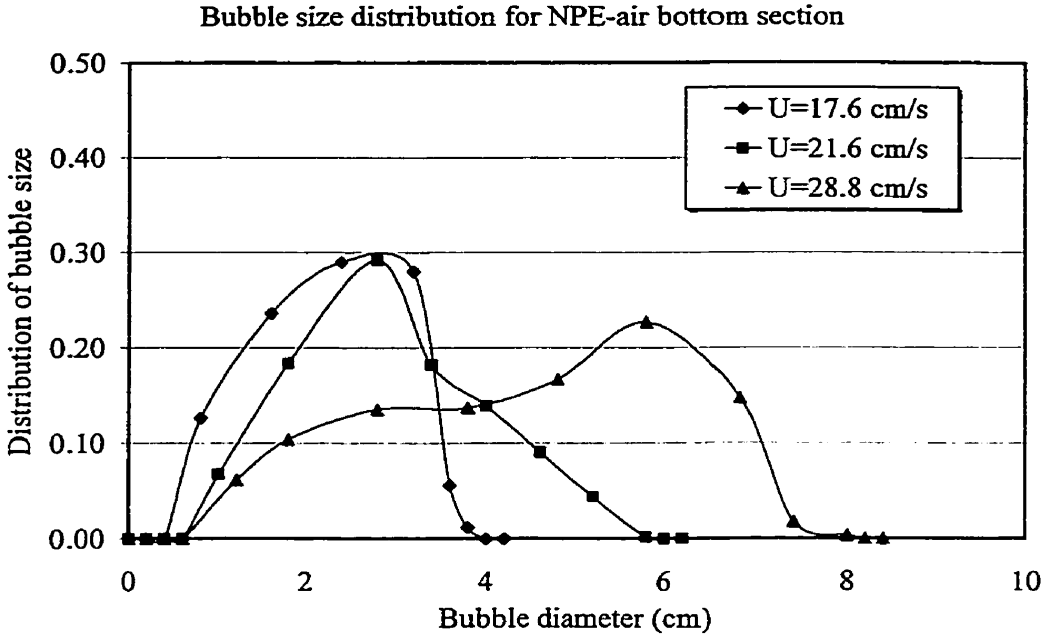

Figure 5.1.1. Distribution of bubble size at three superficial gas velocities for NPE-air system-bottom section of the bed

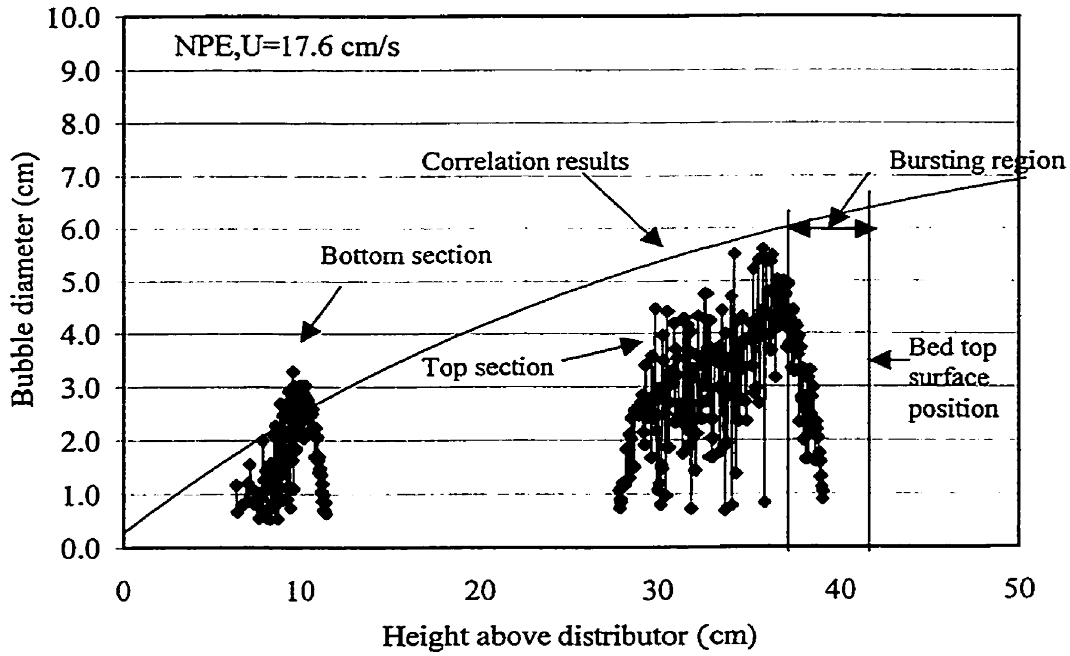

Figure 5.1.2. Averaged bubble size along the entire height for NPE-air system at U=17.6 cm/s

superficial gas velocity bubble size increases. This is easy to understand since more volume of gas flows in the form of bubbles through the bed per second when superficial gas velocity increases. Figures 5.1.2, 5.1.3 and 5.1.4 display the variation of averaged bubble diameter along the height of the fluidized bed at superficial gas velocities of 17.6 cm/s, 21.6 cm/s and 28.8 cm/s, respectively. Apparently, the bubble size increases along the bed height since bubble coalescence occurs as bubbles move up through the bed. Decreasing bubble size at the top of each section is an artifact that is discussed in detail in subsequent paragraphs.

Figure B.2 (Appendix B) shows the original results of bubble diameter from image processing for NPE-air system for the top section of the bed while Figure 5.1.5 indicates the distributions of bubble size for the three superficial gas velocities investigated in this study. Similarly, with an increase in superficial gas velocity larger bubbles were observed at the top section of the bed. The averaged bubble diameter along the bed height are shown in Figures 5.1.6, 5.1.2 and 5.1.3 for the three superficial gas velocities for the top section of the bed. One can see the similar trends that with the increase in superficial gas velocity bubble diameter increases. From Figure 5.1.2 and 5.1.3 one can also conclude that bubble diameter increases from bottom to top of the fluidized bed at the same superficial gas velocity. At the top section of the bed bubble flow is well developed after bubble coalescence and break-up.

For the WPE-air system, eight sets of images were recorded on videotape at four different superficial gas velocities, namely 10.8 cm/s, 14.4 cm/s, 18.0 cm/s and 21.6 cm/s which are $1.5\times U_{mf}$, $2.0\times U_{mf}$, $2.5\times U_{mf}$ and $3.0\times U_{mf}$, respectively. No bubbles were observed at the bottom section of the bed for all the four superficial gas velocities. Therefore, the images obtained at this bed section were not further processed.

Figure B.3 shows the original results of bubble diameter data versus the height above the distributor obtained from image processing for WPE-air system for the top section of the bed at three different superficial gas velocities of 14.4 cm/s, 18.0 cm/s 21.6 cm/s. Figure

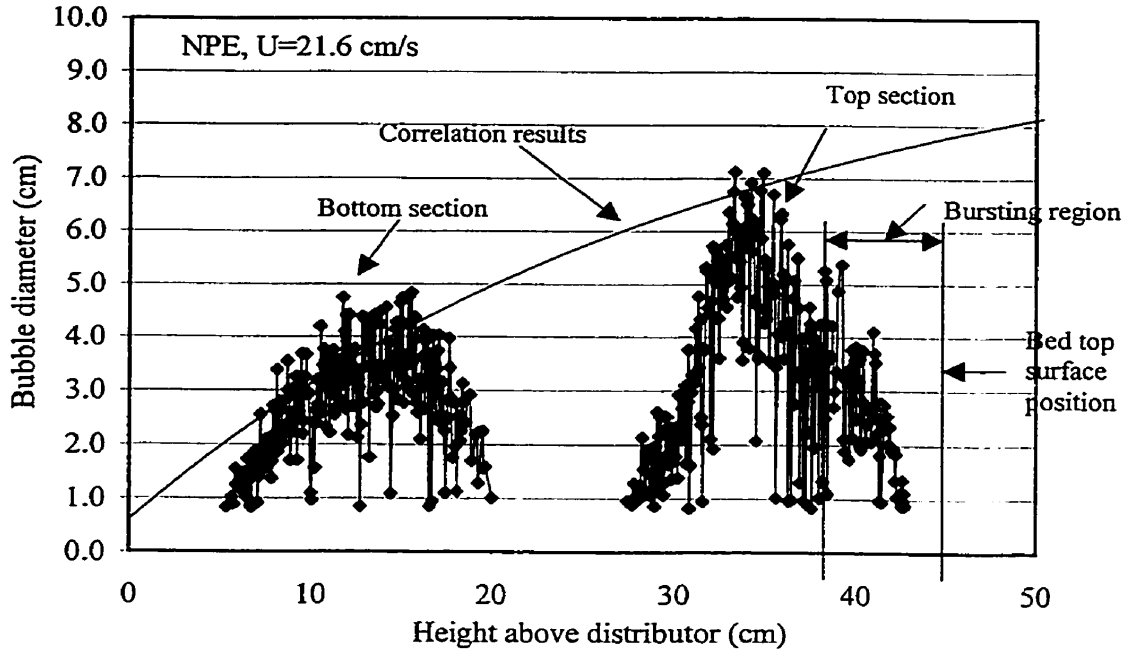

Figure 5.1.3. Averaged bubble size along the entire height for NPE-air system at U=21.6 cm/s

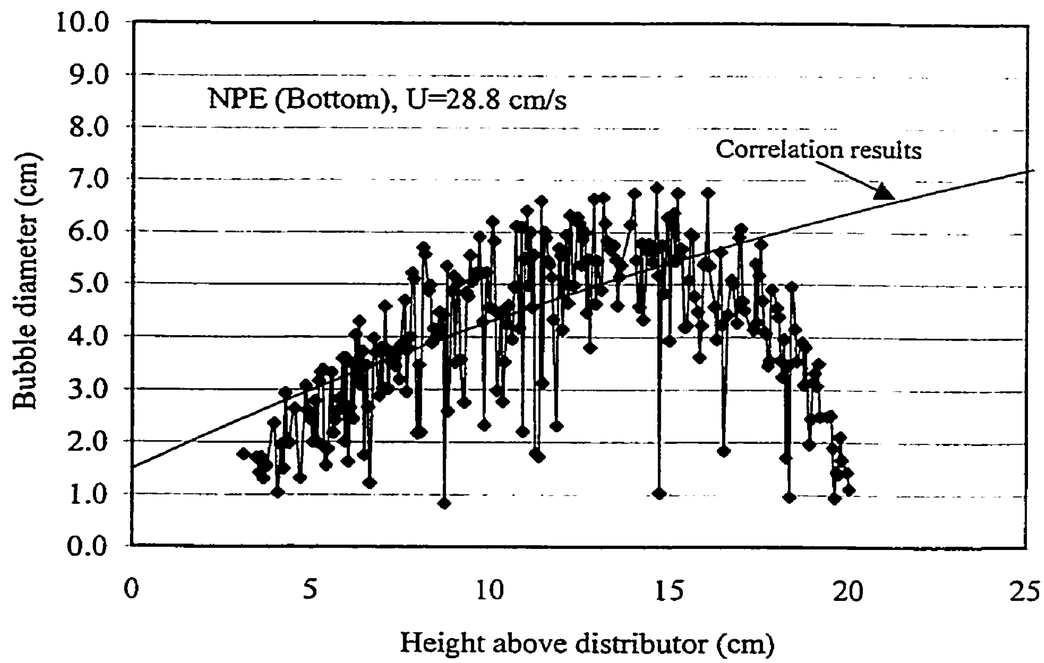

Figure 5.1.4. Averaged bubble size along the height for NPE-air system at U=28.8 cm/s-bottom section of the bed

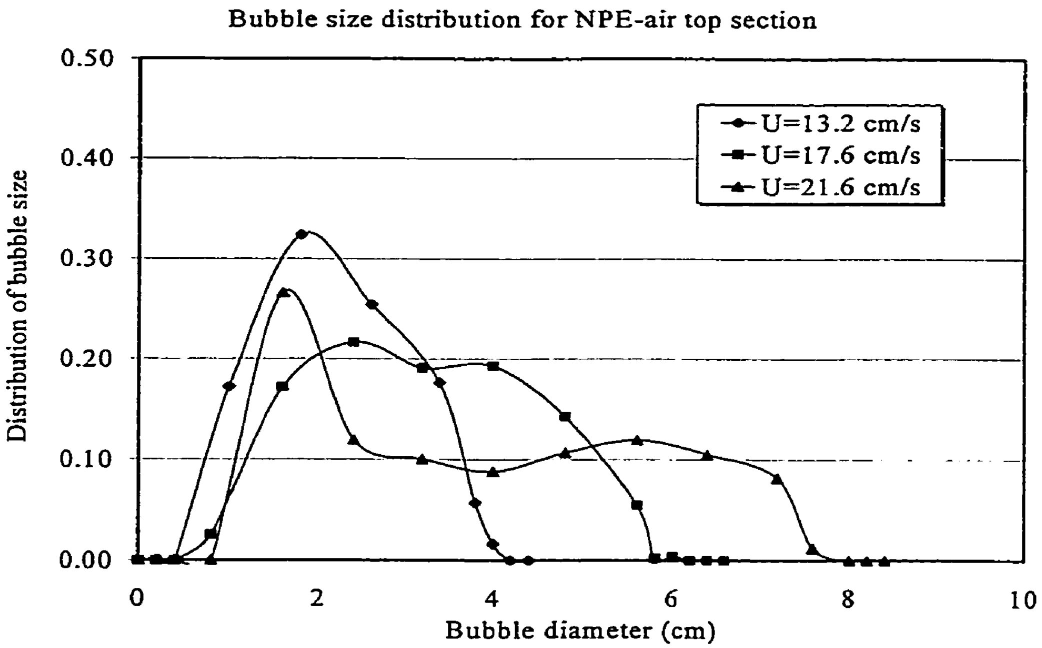

Figure 5.1.5. Distribution of bubble size at three superficial gas velocities for NPE-air system-top section of the bed

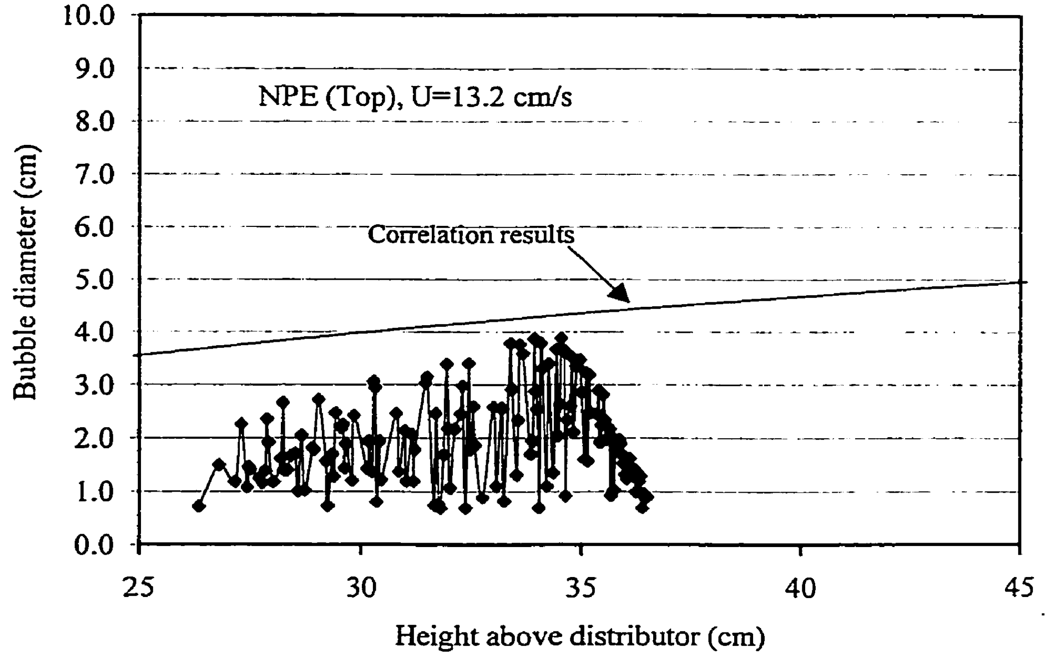

Figure 5.1.6. Averaged bubble size along the height for NPE-air system at U=13.2 cm/s-top section of the bed

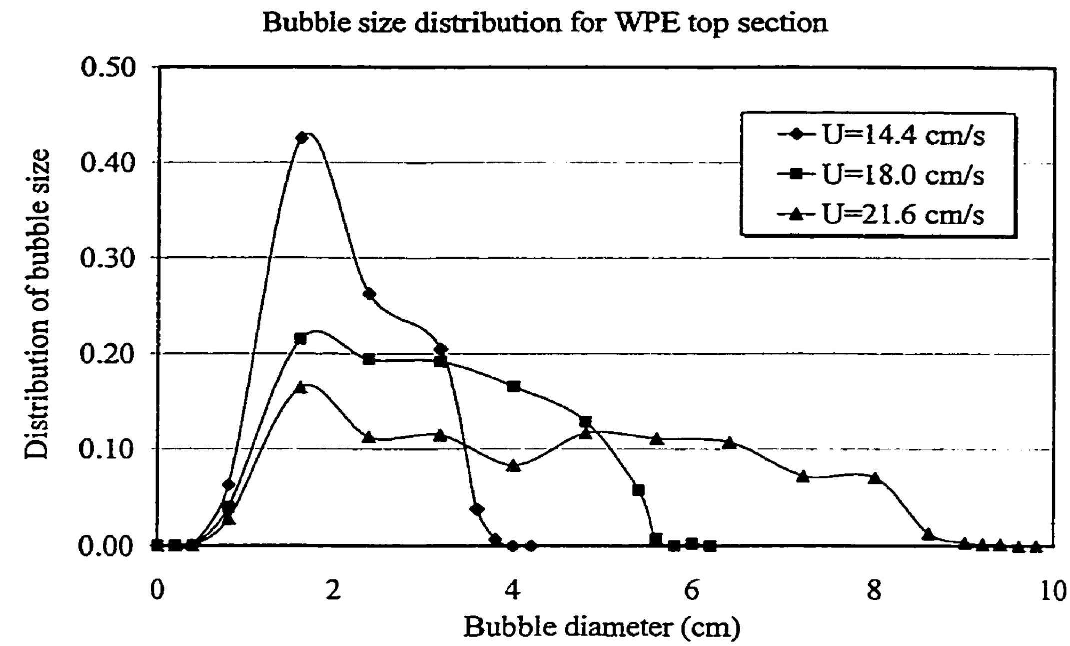

Figure 5.1.7. Distribution of bubble size at three superficial gas velocities for WPE-air system-top section of the bed

5.1.7 illustrates the distribution of bubble size at the three superficial gas velocities. It is also noted that with increase in superficial gas velocity larger bubbles are formed. Figures 5.1.8, 5.1.9 and 5.1.10 show the variation of averaged bubble diameter along the bed height at the three superficial gas velocities mentioned above. With increase in superficial gas velocity bubble diameter increases, and the bubble diameter increases with increase in bed height at a certain superficial gas velocity. The image pictures were obtained at the axial position of 2 cm below the averaged free surface of the fluidized bed for all the three superficial gas velocities. Due to the increase of the bed height with the increase in superficial gas velocity, the fluidized bed was expanding gradually as shown in Figure B.3 and Figure 5.1.8, 5.1.9 and 5.1.10.

For the NS-air system, four sets of images were recorded on videotape. Slugging occurred at the top section of the bed at superficial gas velocities of 35.2 cm/s and 52.8 cm/s which are about 2.0× U_{mf} and 3.0× U_{mf}. Therefore, no further processing was performed for the two top section image sets. Only the two sets of images for the bottom section of the bed were processed. Figure B.4 shows the original results of bubble diameter data versus the height above the distributor obtained from image processing for NS-air system at the two superficial gas velocities mentioned above. Figure 5.1.11 shows the distribution of the bubble size for each superficial gas velocity. For this system, it can also be seen that with the increase in superficial gas velocity larger bubbles appeared. Figures 5.1.12 and 5.1.13 display the results of the averaged bubble diameter along the height of the fluidized bed at the two superficial gas velocities. Similarly, with an increase in superficial gas velocity bubble diameter increases and the bubble diameter increases with an increase in bed height at a certain superficial gas velocity.

In this study, the difference in bubble flow dynamics between top section and bottom section of the fluidized beds was investigated. Figure 5.1.14 illustrates the averaged bubble diameter at the top and bottom section of the fluidized bed at different superficial gas velocities for the NPE-air system. All the populations of bubbles in one image set were included in the

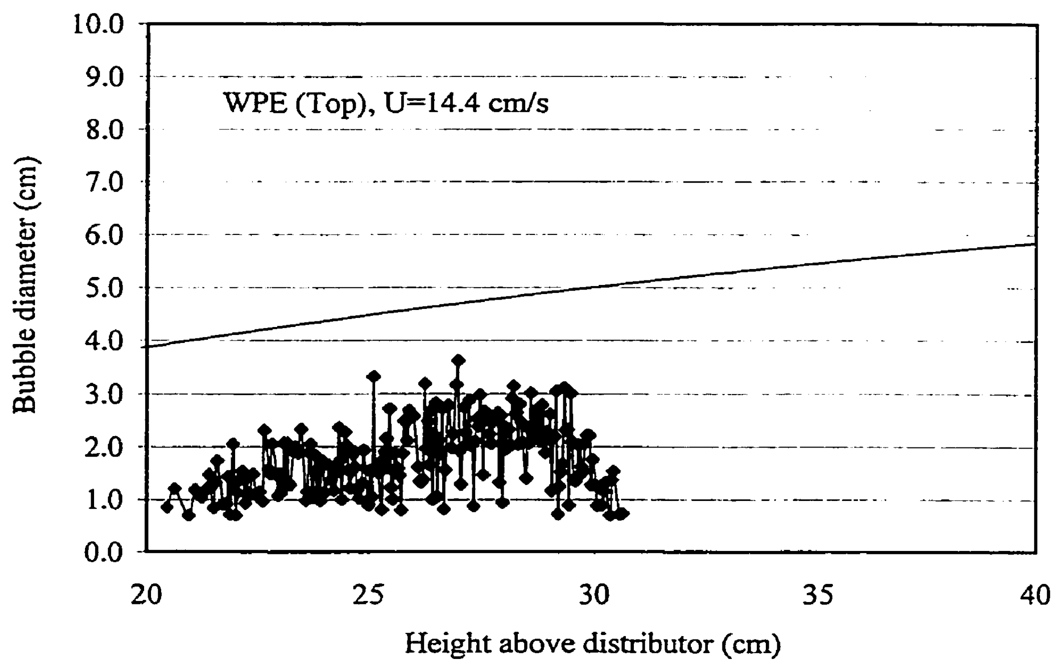

Figure 5.1.8. Averaged bubble size along the height for WPE-air system at U=14.4 cm/s-top section of the bed

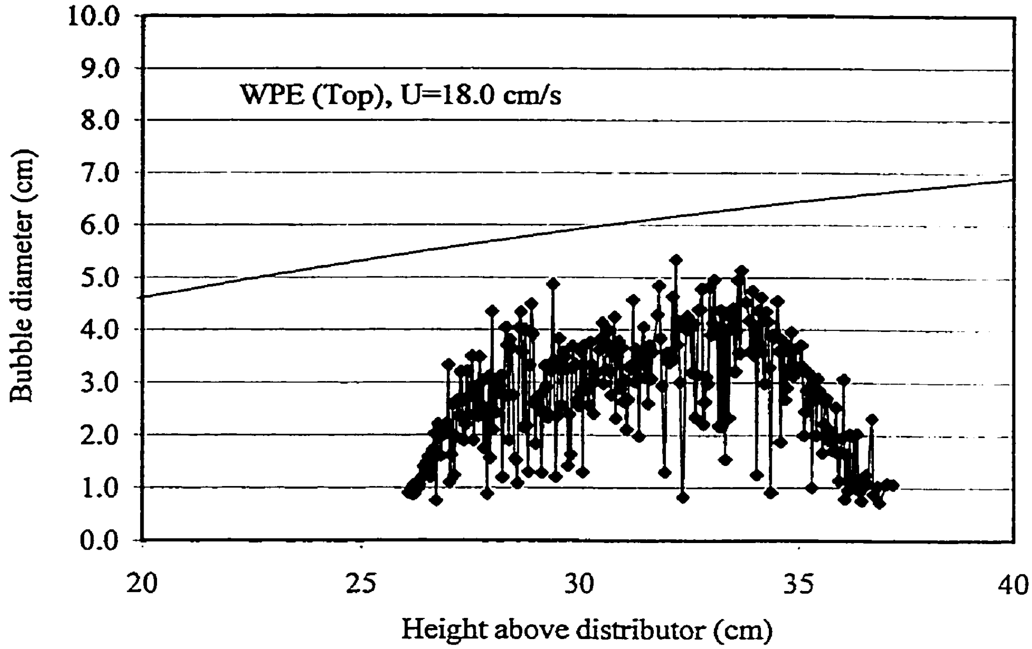

Figure 5.1.9. Averaged bubble size along the height for WPE-air system at U=18.0 cm/s-top section of the bed

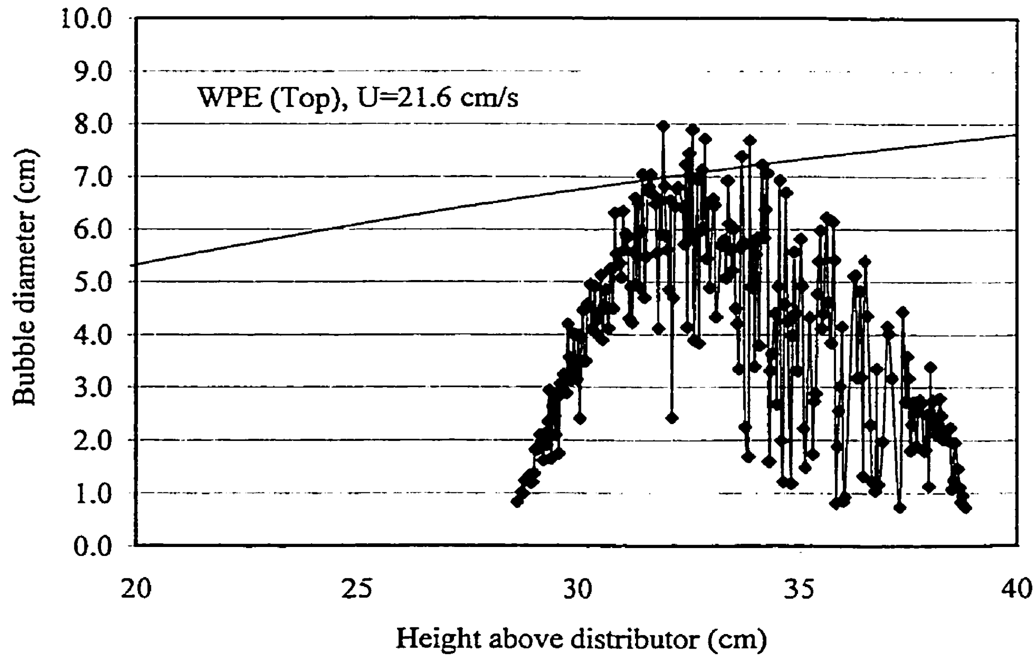

Figure 5.1.10. Averaged bubble size along the height above the distributor for WPE-air system at U=21.6 cm/s-top section of the bed

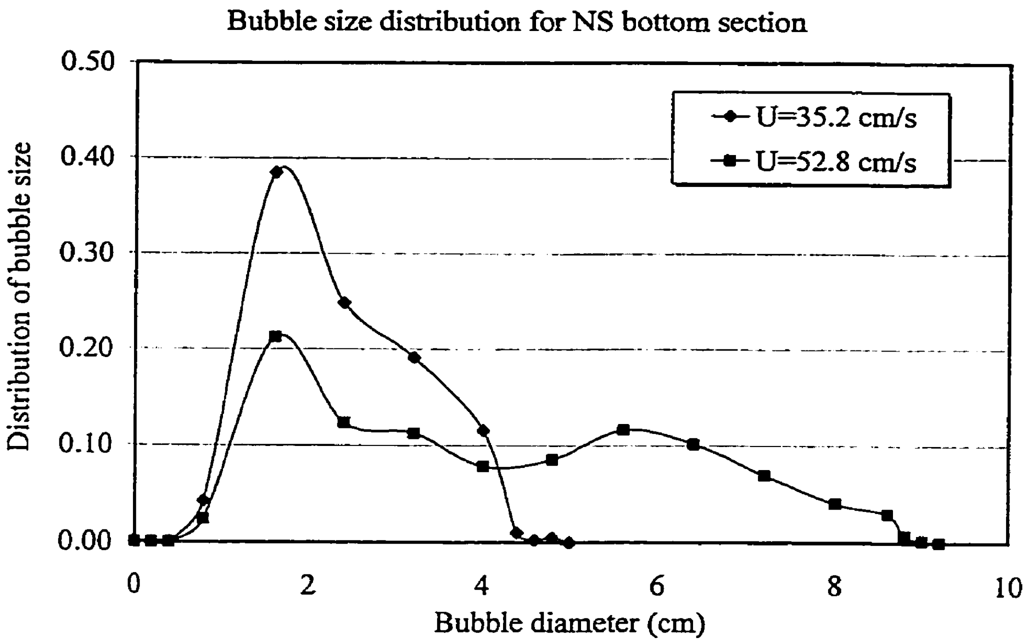

Figure 5.1.11. Distribution of bubble size at two superficial gas velocities for NS-air system-bottom section of the bed

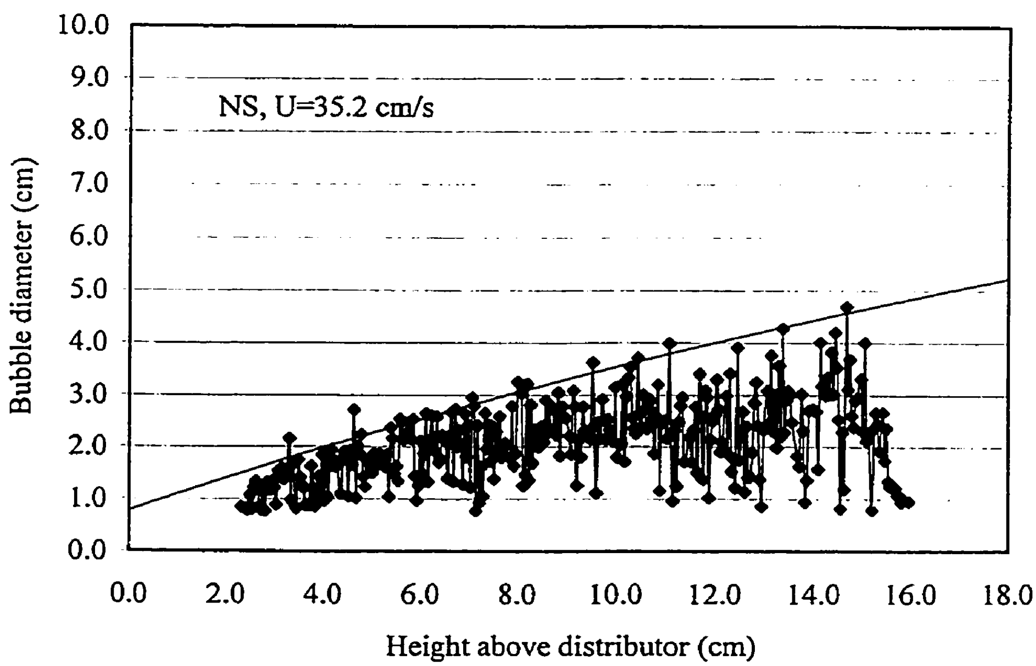

Figure 5.1.12. Averaged bubble size along the height for NS-air system at U=35.2 cm/s-bottom section of the bed

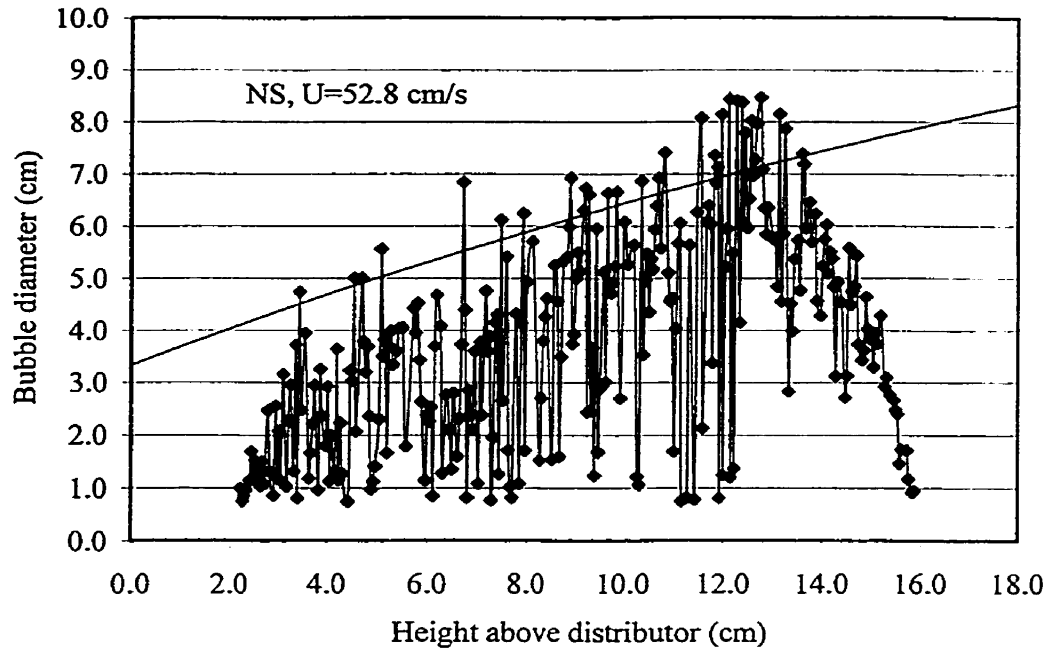

Figure 5.1.13. Averaged bubble size along the height above the distributor for NS-air system at U=52.8 cm/s-bottom section of the bed

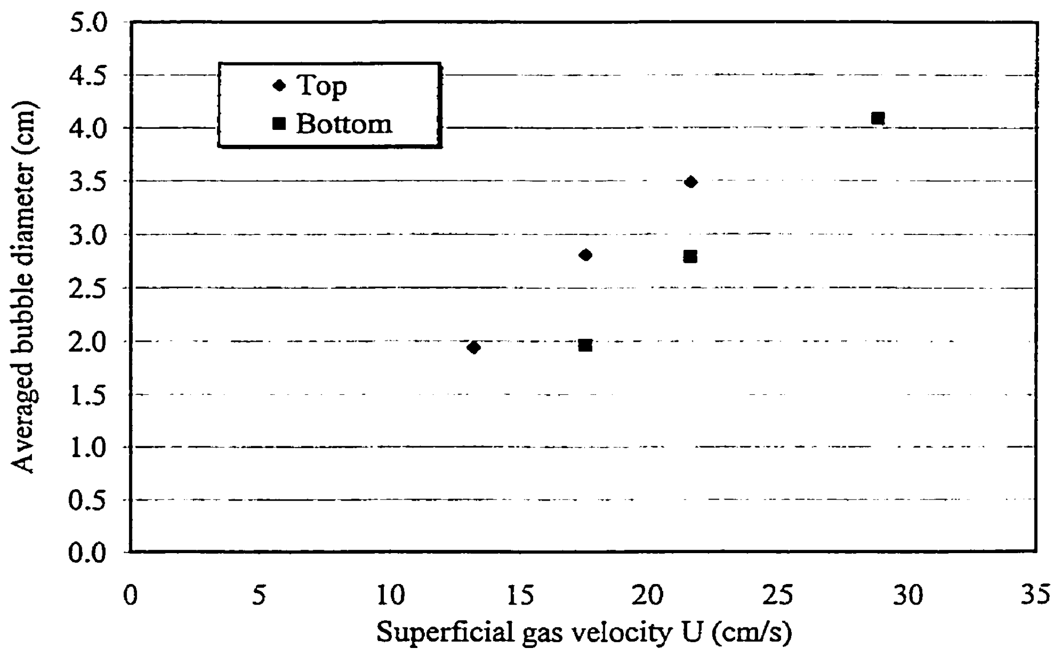

Figure 5.1.14. Difference in bubble diameters for NPE-air system between top section and bottom section of the fluidized bed

averaging. From Figure 5.1.14 it is clear that with an increase in superficial gas velocity the averaged bubble diameter increases, which is consistent with what is expected. It seems that the increase in the averaged bubble diameter is linear with the increase in superficial gas velocity in the range investigated in this study. In addition, the bubble diameter at top section of the bed is always larger than that at bottom section of the bed at the same superficial gas velocity.

The particles used in this study include narrow size distribution polyethylene (NPE), wide size distribution polyethylene (WPE) and narrow size distribution sand (NS). They all belong to Geldart B group according to Geldart's classification. Studies of bubble flow dynamics with polyethylene particle have not been reported in open literature so far to the best of our knowledge. In order to investigate the difference in the bubble flow dynamics with NS and NPE particles, comparisons were conducted and are shown in Figures 5.1.15 and 5.1.16. Figure 5.1.15 shows the averaged bubble diameter versus U/U_{mf} for the two systems. From the figure it is noted that an increase in superficial gas velocity results in an increase in bubble diameter for both systems. It is also clear that the bubble diameter with NPE particles is very close to that with NS particles for the same value of U/U_{mf}. However, in Figure 5.1.16 it seems that the two sets of data are more apart from each other since the minimum fluidization velocities are very different for the two types of particles. For NPE particles the minimum fluidization velocity is 8.9 cm/s and for NS particles it is 18.5 cm/s. This can explain the reason that correlations for bubble diameter in literature always include U_{mf}, the minimum fluidization velocity, as one of the parameters.

As mentioned above, bubble flow dynamics of WPE particles was also investigated to compare the behavior of bubbles in fluidized beds, which have different particle size distributions. Figures 5.1.17 and 5.1.18 show the averaged bubble diameter data versus U/U_{mf} and superficial gas velocities, respectively.

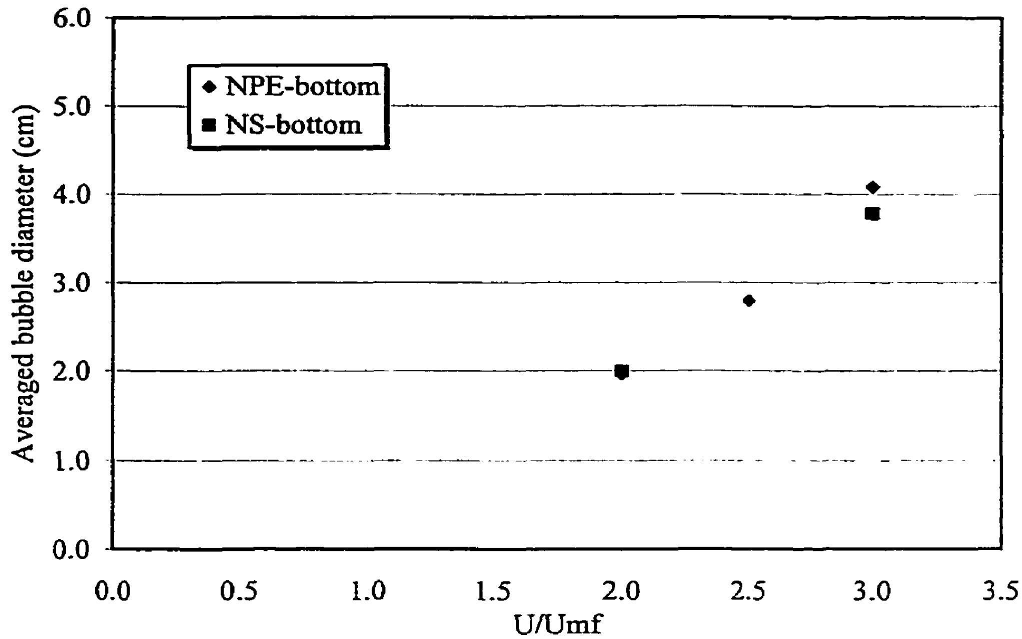

Figure 5.1.15. Difference in bubble diameters between NPE –air system and NS-air system at different U/U_{mf}

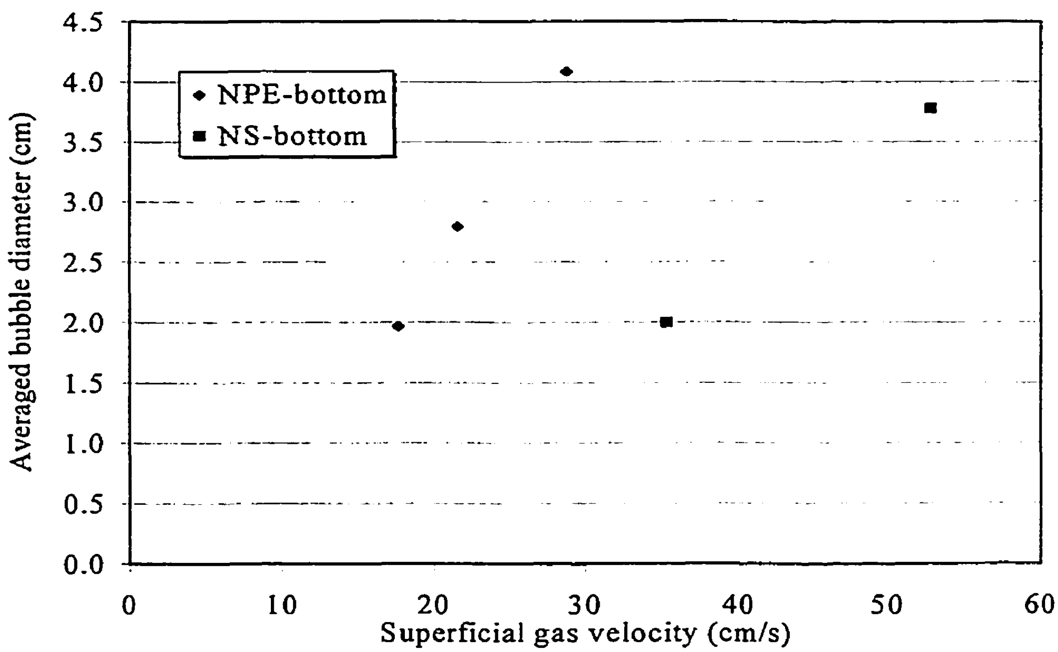

Figure 5.1.16. Difference in bubble diameters between NPE –air system and NS-air system at different superficial gas velocities

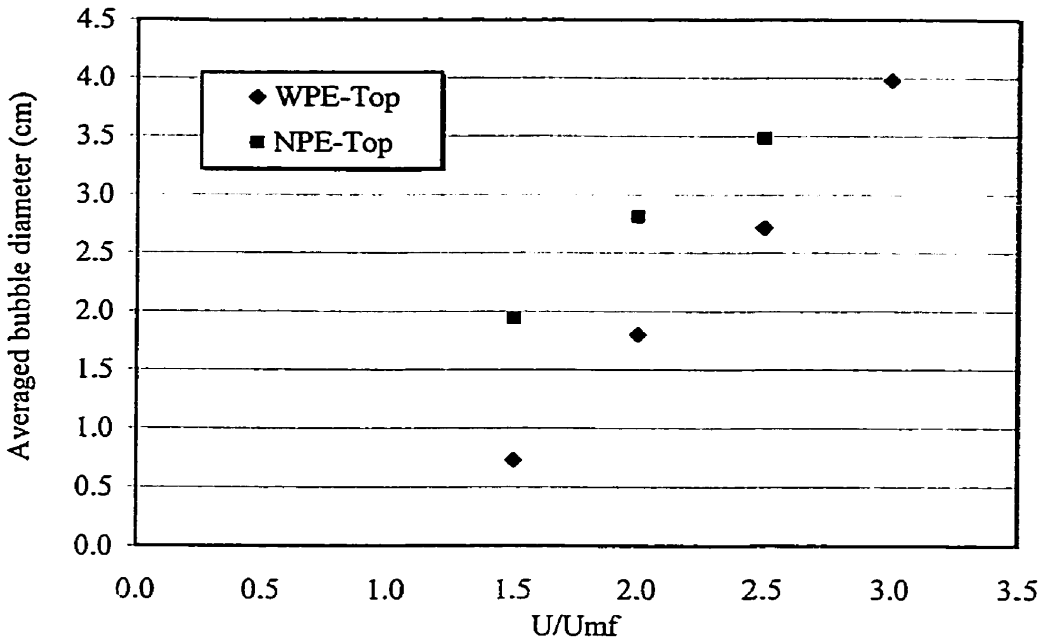

Figure 5.1.17. Difference in bubble diameters between NPE –air system and WPE-air system at different U/U_{mf}

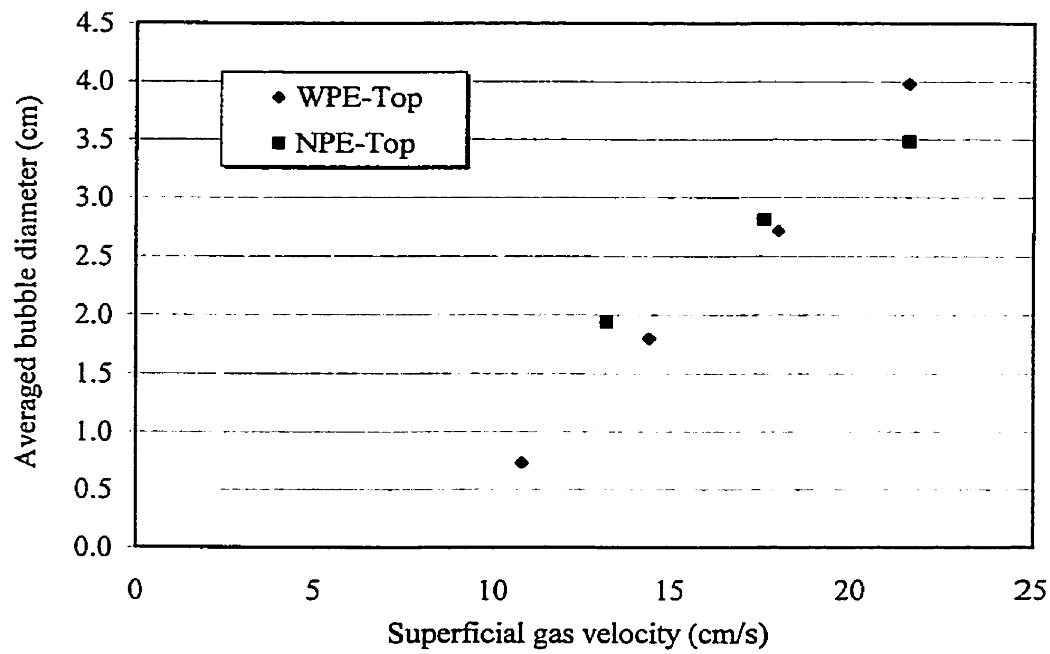

Figure 5.1.18. Difference in bubble diameters between NPE –air system and WPE-air system at different superficial gas velocities

From Figure 5.1.17, one can see that the averaged bubble diameter increases with an increase in U/U_{mf} and that the averaged bubble diameter with NPE particles is larger than that with WPE particles at the same value of U/U_{mf}. One possible reason is that smaller particles that belong to Geldart A in WPE are favorable to generate smaller bubbles in the bed. Therefore, it can be inferred that wider particle size distribution would result in smaller bubbles in fluidized bed, which is desired in fluidization operation for better gas-solid mixing. However, more experimental work is needed before such a general conclusion can be reached. In Figure 5.1.18 the two sets of data are very close to each other since the minimum fluidization velocities of NPE-air system and WPE-air system are close to each other, 8.9 cm/s for NPE particles and 7.1 cm/s for WPE particles. Both Figure 5.1.17 and 5.1.18 indicate that the effect of superficial gas velocity on bubble size is more significant for WPE particles (higher slope).

Figures 5.1.2 and 5.1.3 provide an overview of bubble diameter versus the height above the distributor for the entire fluidized bed at superficial gas velocities of 17.6 cm/s and 21.6 cm/s, respectively, for the NPE-air system. Unfortunately, images were not taken at the middle section of the bed. This is recommended for future work. From these two figures one can see the trend that with an increase in the height above the distributor the bubble diameter increases at both superficial gas velocities. It may be noted that for each data set, bubble diameter increases sharply along the height at the beginning and then gradually. After the bubble diameter cure reaches its highest point it decreases sharply, which is not as expected since, generally, bubble diameter should always increase gradually along the height. The possible reasons for this discrepancy are as below.

- In the current image processing technique, a bubble at the top of the frame is not counted if part of it is out of the frame. Howev-er, these edge bubbles are normally large ones. In Figure 5.1.2, bubble diameter decreases along the height after it reaches the highest point because this region is very close to the top of the frame and some large bubbles are omitted by the image processing procedures. At higher superficial gas velocity, in the same region in Figure 5.1.3, the trend is more significant and the region is longer (bed height from 16 cm to 20 cm). For the top section of the bed at the two superficial gas velocities, the regions are even more pronounced with the bed height from 36 to 40 cm in Figure 5.1.2 and from 35 to 43 cm in Figure 5.1.3. Another contribution to this bubble diameter decrease with bed height for the top section is the bursting of large bubbles. Modifications are needed in the bubble marking and tracking programs to take into account of the portion of bubbles at the top and bottom of the frame. This is again suggested as future work.

- Similarly, in the program a large bubble at the bottom of the frame is not counted if part of it is out of the frame, which explains the sharp increase in bubble diameter along the bed height at the bottom region of the frame. In addition, some artifacts may also contribute to this sharp increase. It was mentioned in Chapter 4 that the background of the digital image does not have uniform intensity distribution. The top part is brighter and the bottom part is darker. The possible reason is that the gradient change in emulsion phase density along the fluidized bed height and the artificial effect of the fluoroscopy system. In order to remove the artificial effect, subtracting image background was performed. However, the artificial effect may still be there at a lower level. Removal of the artifacts should also be reconsidered in future work.

5.1.2. Bubble Size Prediction with Correlations

Correlations for predicting bubble size in fluidized beds have been reviewed in Chapter 2. In the literature, a number of bubble diameter correlations have been proposed (Yasui and Johanson, 1958; Geldart, 1970-1971; Mori and Wen, 1975; Rowe, 1976; Darton *et al.*, 1977; Werther, 1978; Horio and Nonaka, 1987 and Choi *et al.*, 1988, 1998).

After an investigation of all the individual correlations discussed in Chapter 2, the following brief summary is made. The applicable ranges of operating conditions for Werther's correlation (1978) (Equation (2.6)) are not suitable for this study. Horio and Nonaka (1987) (Equation (2.7)) proposed a bubble diameter correlation that takes both break-up and coalescence into account to predict bubbling characteristics of fluidized beds with a variety of powders, including Geldart group A. However, the authors mentioned in the article that for the case of Geldart group B powders the correlation automatically converges to the conventional correlation of Mori and Wen (1975), whose predictions are close to those of Rowe (1976) and Darton *et al.* (1977). In 1998, in order to derive a consistent interpretation of mean bubble size from the bubbling behaviors of fluidized beds of Geldart group A, B and D particles, a generalized bubble-growth model was proposed by Choi *et al.* (1998). In the article, Choi *et al.* (1998) indicated that the prediction of bubble size from their correlation was as good as that from Horio and Nonaka's correlation (1987) in fluidized beds of Geldart group A and B particles. Therefore, only the correlation proposed by Mori and Wen (1975) was chosen to predict bubble diameters in fluidized beds in this study as shown in Equation (2.3) to (2.5), since all the particles used in this study are Geldart B. The bubble size d_b at any height z in the bed can be given as:

$$\frac{d_{bm} - d_b}{d_{bm} - d_{b0}} = e^{-0.3z/d_t} \qquad (5.1.1)$$

The ranges of data from which this correlation was obtained are

$$d_t \le 1.3m \qquad 0.5 \le U_{mf} \le 20cm/s$$

$$60\mu m \le d_p \le 450\mu m \qquad U - U_{mf} \le 48cm/s$$

For the prediction of bubble diameters with the above correlation, Table 5.1 lists the properties of the fluidized bed and the operating conditions used in this bubble diameter prediction. One should note that the diameter of particles d_p listed in Table 5.1 are larger than 450 μm which is the upper limit of applicable d_p range for Mori and Wen's correlation. Considering that NPE, WPE and NS are all Geldart group B particles, which was the basis of Mori and Wen's correlation, violation of upper d_p limit was ignored in the prediction.

The solid lines in Figures 5.1.2, 5.1.3, 5.1.4, 5.1.6, 5.1.8, 5.1.9, 5.1.10, 5.1.12 and 5.1.13 show the predicted bubble diameters from the correlation proposed by Mori and Wen (1975). For the bottom section of the bed, predicted results are slightly higher than the averaged image processing results as shown in Figures 5.1.2, 5.1.3, 5.1.4, 5.1.12 and 5.1.13 while the predicted results are higher than the averaged bubble diameter for the top section of the bed as shown in Figures 5.1.2, 5.1.3, 5.1.6, 5.1.8, 5.1.9, and 5.1.10.

Table 5.1. Bed properties and operating conditions for bubble size prediction

	NPE	WPE	NS
d_t	10 cm	10 cm	10 cm
d_p	0.543 mm	0.830 mm	0.530 mm
U_{mf}	8.9 cm/s	7.1 cm/s	18.5 cm/s
U	13.2 cm/s 17.6 cm/s 21.6 cm/s 28.8 cm/s	10.8 cm/s 14.4 cm/s 18.0 cm/s 21.6 cm/s	32.2 cm/s 52.8 cm/s

One of the possible reasons for this deviation is that Mori and Wen's correlation was based on experimental data obtained in fluidized beds with L/D<2. The other reason may be the experimental data that Mori and Wen used to develop the correlation are not statistically representative due to the limited number of bubbles measured, which was about 10 to 20 for each operating condition. In this study, the number of bubbles measured is from 244 to 841 as shown in Table 4.1. In addition, the portion of bubbles at the top and bottom of the frame was not taken into account in the image processing method in this study. This also contributed to that the bubble size from the image processing is smaller than that from the correlation at the top and bottom of the frame. The discrepancy also indicates that Mori and Wen's correlation gives too much weight on the effect of bed height on bubble size at the region L/D>2. Therefore, the correlation and the image processing method should be modified in future work.

5.2. Bubble Volume Fraction

Bubble volume fraction is another parameter obtained using the image processing software package developed in this study. As mentioned in Chapter 4, the bubble volume fraction is defined as the ratio of the total bubble geometric volume to the fluidized bed volume Equation (4.11). The bubble volume is assumed to be the sphere volume having the same equivalent diameter as the bubble measured in the image frames.

5.2.1. Analysis of Bubble Volume Fraction

Individual values of bubble volume fraction were obtained for each frame during the image processing. As previously noted, the interval between frames is 33 ms. Detailed original results from the image processing are shown in Figures C.1 to C.4. Averaging of each data set was carried out over the time period considered. As shown in Figure 5.2.1, for the NPE-air system at the bottom section of the bed, the averaged bubble volume fraction is 0.0032, 0.019 and 0.059 at superficial gas velocities of 17.6 cm/s, 21.6 cm/s and 28.8 cm/s, respectively. For the same system at top section of the bed, the bubble volume fraction is 0.0031, 0.013 and 0.062 at superficial gas velocities of 13.2 cm/s, 17.6 cm/s and 21.6 cm/s. With the increase in superficial gas velocity, bubble volume fraction increases at both bottom and top sections of the fluidized bed for the NPE-air system. The bubble volume fraction at the top section of the bed is always higher than that at bottom section of the bed, since bubbles become larger and larger when they are rising from the bottom to the top of the bed. Although the bubble occurrence frequency (in section 5.3) is lower at the top section at superficial gas velocity of 17.6 cm/s the averaged bubble diameter is 2.81 cm, which is much larger than that at the bottom section, 1.96 cm. Therefore, the bubble volume fraction at the top section is higher than that at the bottom section.

For the WPE-air system at the top section, the original image processing results of bubble volume fractions are presented in Figure C.3. The averaged bubble volume fraction is 0.0042, 0.025 and 0.067 at superficial gas velocities of 14.4 cm/s, 18.0 cm/s and 21.6 cm/s, respectively, as shown in Figures 5.2.2 and 5.2.3.

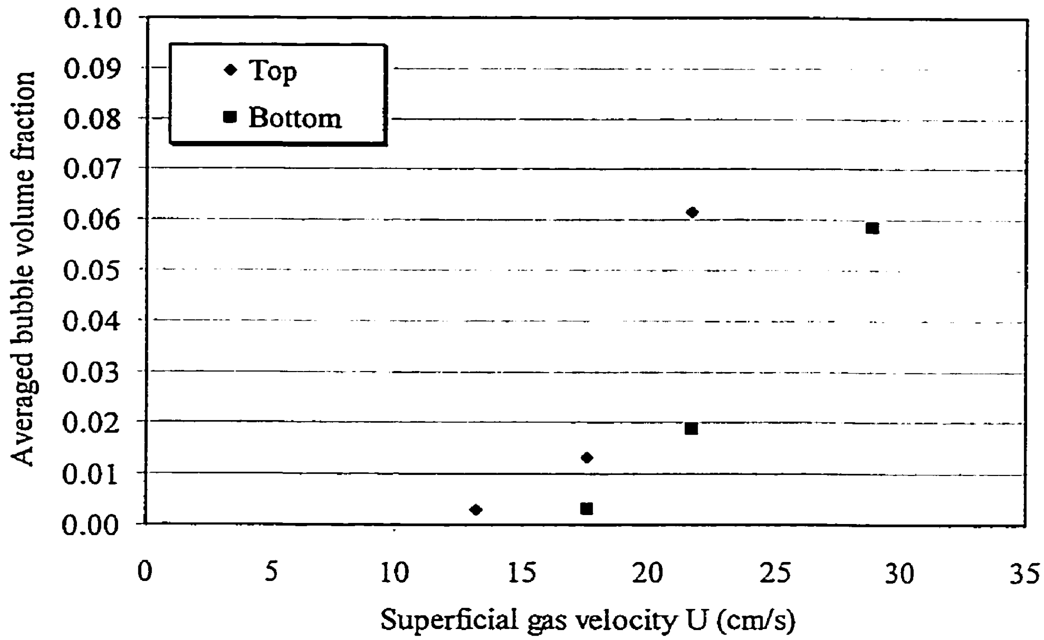

Figure 5.2.1. Comparison of averaged bubble volume fraction for NPE-air system between top and bottom section

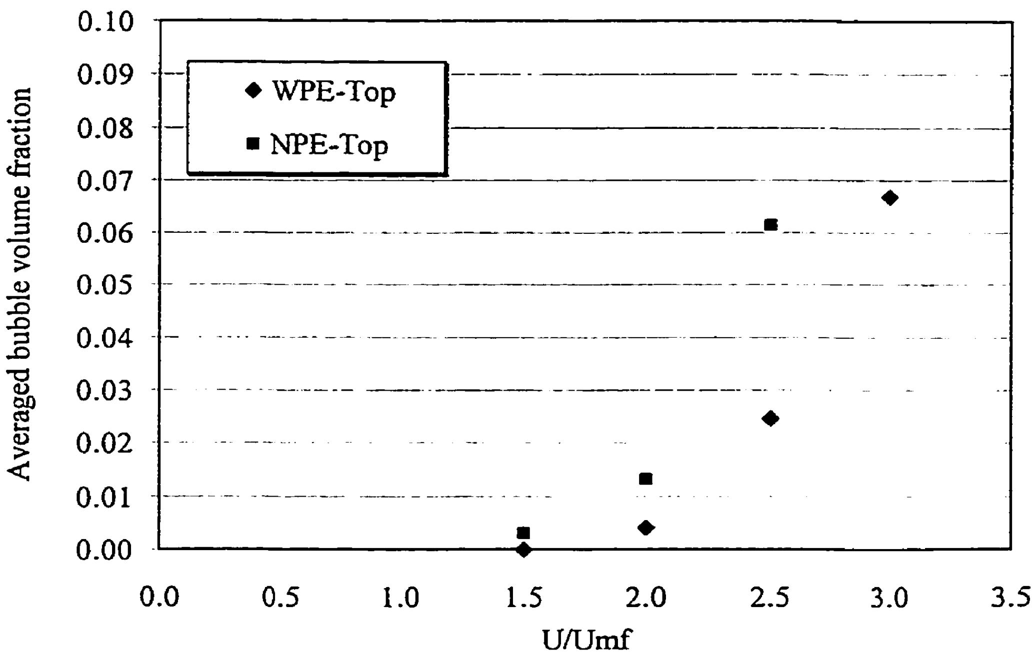

Figure 5.2.2. Comparison of averaged bubble volume fraction versus U/U_{mf} between NPE-air and WPE-air systems -top section of the bed

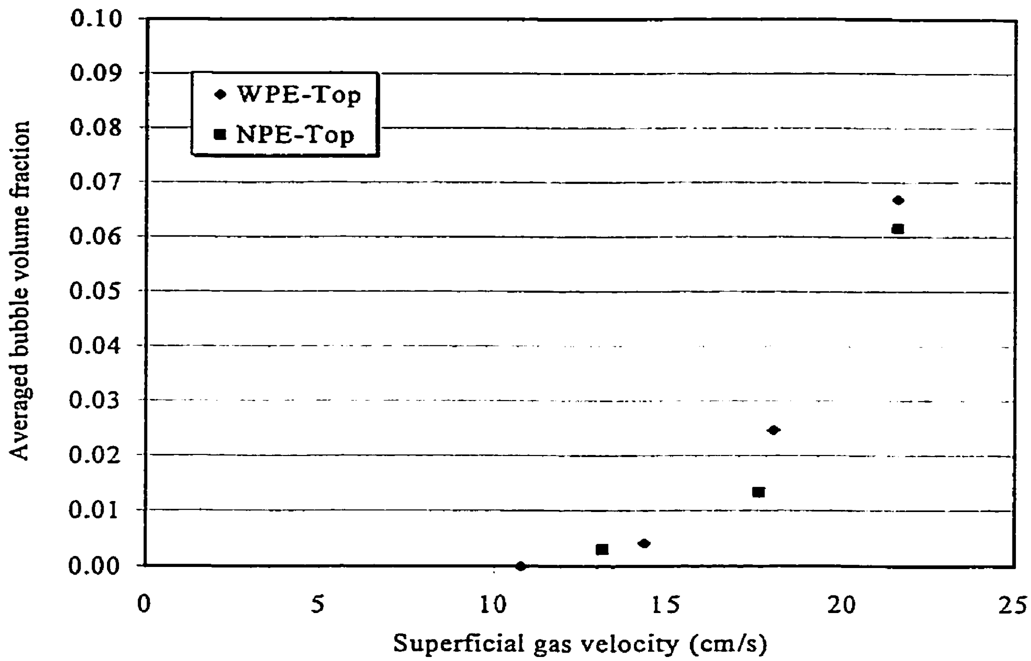

Figure 5.2.3. Comparison of averaged bubble volume fraction versus superficial gas velocity between NPE-air and WPE-air systems -top section of the bed

Referring to Figure 5.2.2, one can see that at same U/U_{mf} bubble volume fraction for the NPE-air system is higher than that for the WPE-air system. In Figure 5.2.3, one can note that at the same superficial gas velocity, bubble volume fraction is, however, close for the two systems.

For the NS-air system, the image processing results are shown in Figure C.4. Figures 5.2.4 and 5.2.5 show comparisons of bubble volume fraction between the NPE-air and the NS-air system. In Figure 5.2.4, it is seen that the bubble volume fraction for the NS-air system is higher than that for the NPE-air system. In Figure 5.2.5, the two data sets are further away from each other due to the significant difference in U_{mf} for the two systems. For the NS-air system bubbles were observed just above the distributor while there were no bubbles observed at the region close to the distributor for the NPE-air system. This explains the higher observed bubble volume fraction for NS-air system as compared to the NPE-air system for the same U/U_{mf}.

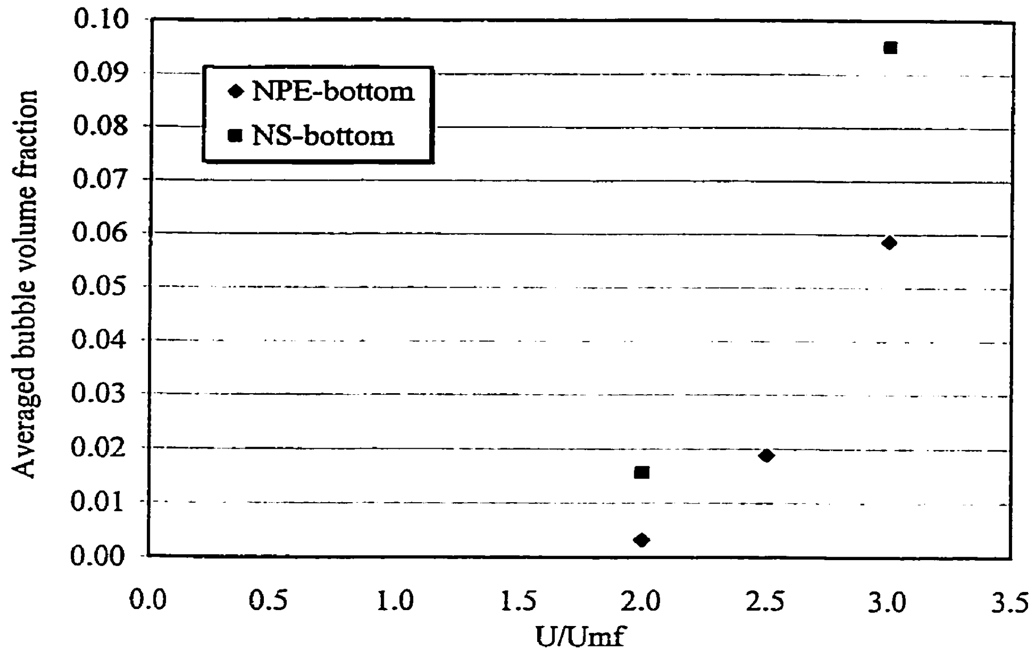

Figure 5.2.4. Comparison of averaged bubble volume fraction versus U/U_{mf} between NPE-air and NS-air systems -bottom section of the bed

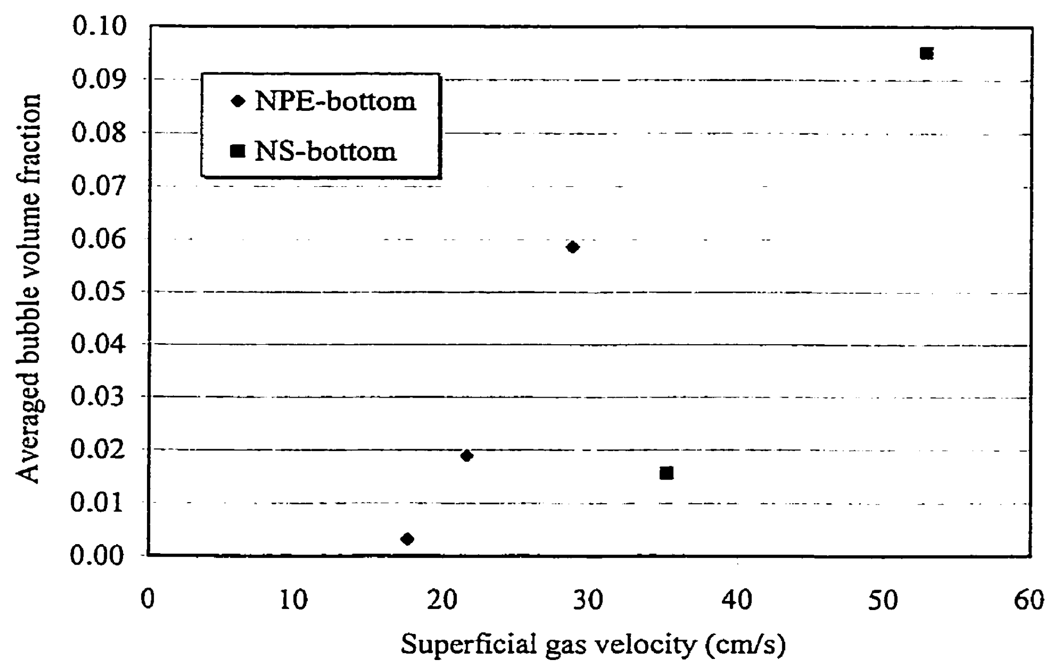

Figure 5.2.5. Comparison of averaged bubble volume fraction versus superficial gas velocity between NPE-air and NS-air systems -bottom section of the bed

5.2.2. Verification of the Image Processing Method

As mentioned before, the images processed in this work are two-dimensional while the fluidized bed is cylindrical or three-dimensional. In the current image processing work it was assumed that bubble overlapping is negligible. Some artifacts might be introduced by this assumption. In order to validate the present image processing method bubble volume in the fluidized bed is calculated by two methods. One is by bubble volume fraction data obtained from the image processing, while the other one is by fluidized bed expansion. The data for NPE-air system at superficial gas velocity of 17.6 cm/s and 21.6 cm/s were chosen for the verification.

It is known that the bursting region at the top of the bed has very low emulsion phase density. The reason is that in that region most large bubbles burst into small bubbles as indicated in Figures 5.1.2 and 5.1.3, for example. In the current image processing, part of the bursting region was included in the calculation of bubble volume fraction. Therefore, the bubble volume fraction value obtained from image processing must be lower than the real value.

In order to remove the effect of bursting region on the calculation of bubble volume and bed expansion volume, 37 cm and 39 cm were taken as the fluidized bed heights at superficial gas velocities of 17.6 cm/s and 21.6 cm/s, respectively. These two values of bed heights are considered below the bursting region by referring to Figures 5.1.2 and 5.1.3. Other data for the calculation of the volumes are listed in Table 5.2. At A superficial gas velocity of 17.6 cm/s, the calculated bubble volume is 24.0 cm^3 while the bed expansion volume is 39.3 cm^3. At a superficial gas velocity of 21.6 cm/s, the calculated bubble volume is 123.1 cm^3 while the bed expansion volume is 196.2 cm^3. The deviation is 39% for the former case and 37% for the latter case. The detailed calculations are shown in Appendix C.

If two-phase theory (Toomey and Johnstone, 1952) is true the bubble volume should be equal to the bed expansion volume. Kunii and Levenspiel stated in their book that two-phase theory does not fit experimental findings well (Kunii and Levenspiel, 1991). The emulsion phase does not maintain the same density as that at minimum fluidization velocity. This was also observed in this study. Emulsion phase density decreases with the increase in the bed height as discussed in Chapter 4. Therefore, it is assumed that the difference between the calculated bubble volume and bed expansion volume is caused by the change in emulsion phase density.

If the emulsion phase density differences are taken into account, about 25% of the gas goes to emulsion phase for Geldart B particle fluidized beds (Kunii and Levenspiel, 1991), the deviation would be reduced to 12-14%. This 12-14% deviation may be caused by bubble overlapping and other artificial errors introduced in the experiments and image processing. However, a more accurate verification should be conducted based on experimentally measured emulsion phase voidage or density data in addition to the data obtained in this work. This is also recommended as a part of future work.

Table 5.2. Calculation of bubble volume and bed expansion volume for NPE-air system (Fluidized bed height is 36.5 cm at U_{mf})

	U=17.6 cm/s	U=21.6 cm/s
Bubble volume fraction at bottom	0.0032	0.0188
Bubble volume fraction at top	0.0133	0.0616
Averaged	0.00825	0.0402
Fluidized bed height below bursting region	37 cm	39 cm
Fluidized bed volume	2904 cm^3	3061 cm^3
Bubble volume in the bed V_{bubble}	24.0 cm^3	123.1 cm^3
Bed expansion volume V_{bed}	39.3 cm^3	196.2 cm^3
V_{bubble}/V_{bed}	0.61	0.63

5.3. Analysis of Bubble Occurrence Frequency

It was mentioned in Chapter 4 that the image processing software developed in this study sequentially and automatically measures bubble size and velocity, while it counts new bubble occurrence frequency as well. Bubbles coming from the bottom of each image frame are considered as new bubbles in the current bubble image processing. The bubble occurrence frequency (Equation (4.9)) is defined as the total number of new bubbles counted for all the frames in one data set divided by the time period during which the frames are counted. Figures 5.3.1 5.3.2, 5.3.4 and 5.3.7 show the original results of bubble frequency measurements from image processing. Since the number of new bubbles, N, is an accumulated number, when the software is just initiated to number the new bubbles, N is small and changes dramatically with time. Therefore, the bubble occurrence frequency also varies dramatically. After 2 to 3 seconds the bubble occurrence frequency becomes relatively stable with time.

For the NPE-air system at the bottom section of the bed, the averaged bubble occurrence frequency is 9.0/s, 9.5/s and 10.3/s at superficial gas velocities of 17.6 cm/s, 21.6 cm/s and 28.8 cm/s, respectively. For the NPE-air system at the top section of the bed, the averaged bubble occurrence frequency is 4.8/s, 5.8/s and 9.7/s at superficial gas velocities of 13.2 cm/s, 17.6 cm/s and 21.6 cm/s, respectively. These data are shown in Figure 5.3.3. From the figure, one can see that with an increase in superficial gas velocity bubble occurrence frequency increases for both bottom and top sections. At a superficial gas velocity of 17.6 cm/s ($2.0\times U_{mf}$), the bubble occurrence frequency at the bottom section of the bed is higher than that at top section due to the fact that more small bubbles are formed at the bottom of the bed. Some of them coalesce into large bubbles while they are rising along the bed height. When superficial gas velocity increases to 21.6 cm/s ($2.5\times U_{mf}$), the bubble occurrence frequency converges for the top and bottom sections. The reason may be that at higher gas velocity more large bubbles break up or less coalescence than at lower superficial gas velocity. Therefore, the top section bubble occurrence frequency is not lower than that for the bottom section.

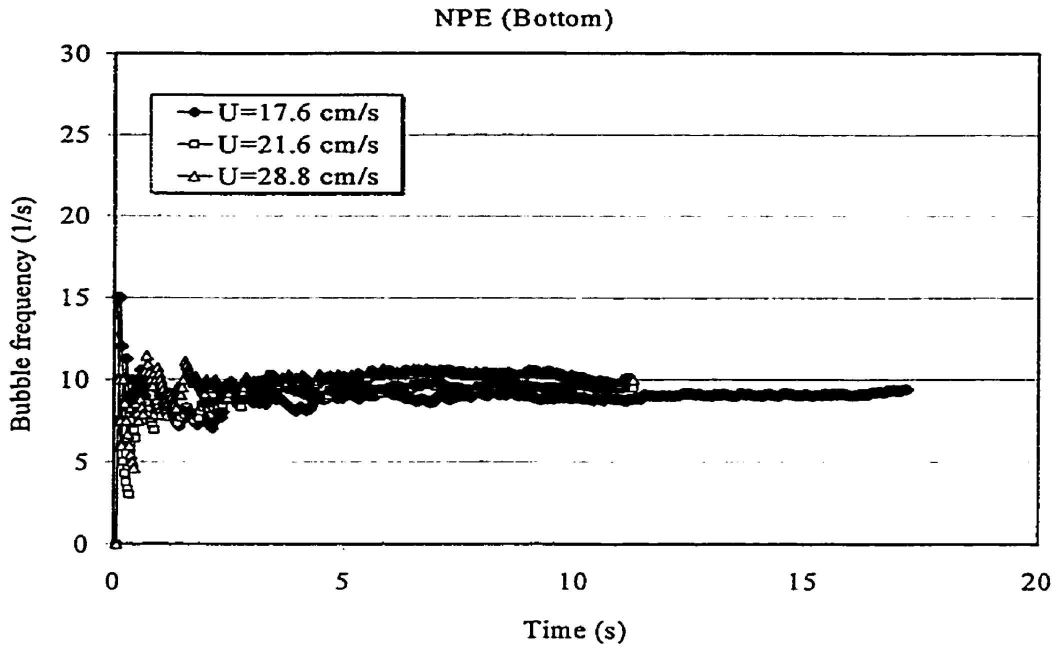

Figure 5.3.1. Image processing results for bubble occurrence frequency for NPE-air system at three superficial gas velocities –bottom section of the bed

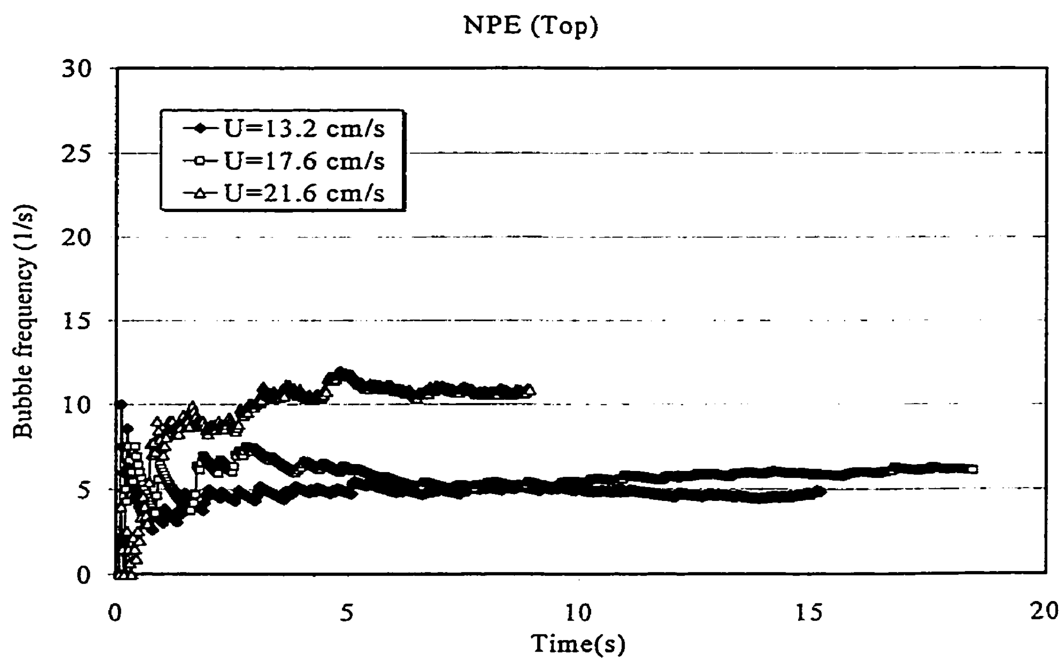

Figure 5.3.2. Image processing results for bubble occurrence frequency for NPE-air system at three superficial gas velocities –top section of the bed

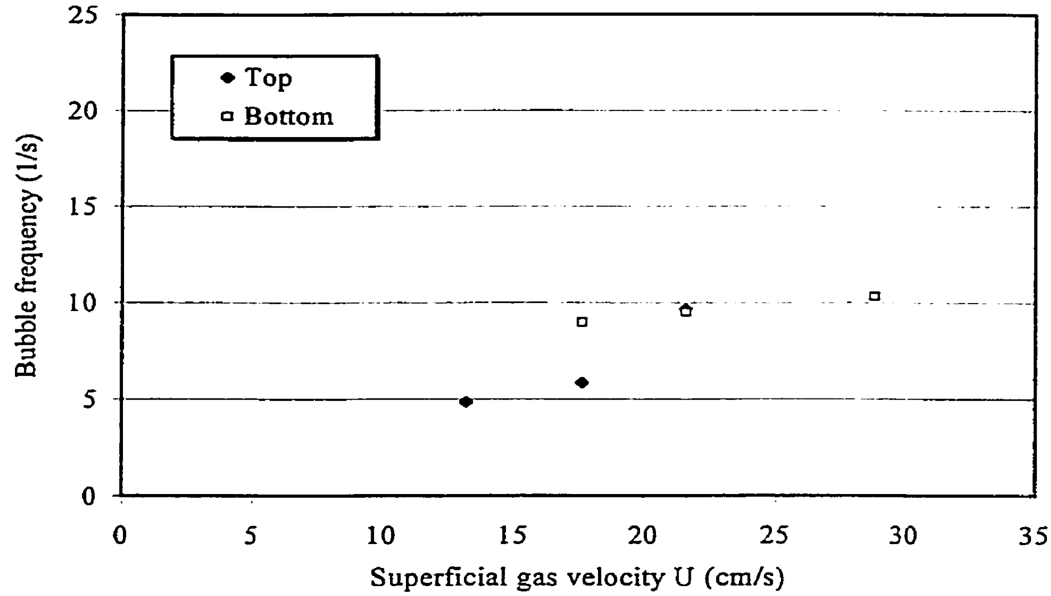

Figure 5.3.3. Comparison of averaged bubble occurrence frequency between top and bottom sections for the NPE-air system

For the WPE-air system at the top section of the bed, the averaged bubble occurrence frequency is 10.2/s, 12.5/s and 12.8/s at superficial gas velocities of 14.4 cm/s, 18.0 cm/s and 21.6 cm/s, respectively. Comparing bubble occurrence frequency data between NPE-air and WPE-air systems, one can note that with an increase in U/U_{mf} or superficial gas velocity, bubble occurrence frequency increases for both NPE-air and WPE-air systems as shown in Figures 5.3.5 and 5.3.6. Moreover, bubble occurrence frequency for the WPE-air system is higher than that for the NPE-air system. The wide particle size distribution in the WPE-air system may cause more bubble break-up than the narrow particle size distribution in the NPE-air system.

For the NS-air system, the averaged bubble occurrence frequency is 10.3/s and 12.3/s at superficial gas velocities of 35.2 cm/s and 52.8 cm/s, respectively, as shown in Figures 5.3.8 and 5.3.9. The trends of the increase in bubble occurrence frequency with U/U_{mf} or superficial gas velocities are similar for the NPE-air and the NS-air system at the bottom section of the fluidized beds, where bubble flow has not been fully developed and there is not much coalescence and break-up.

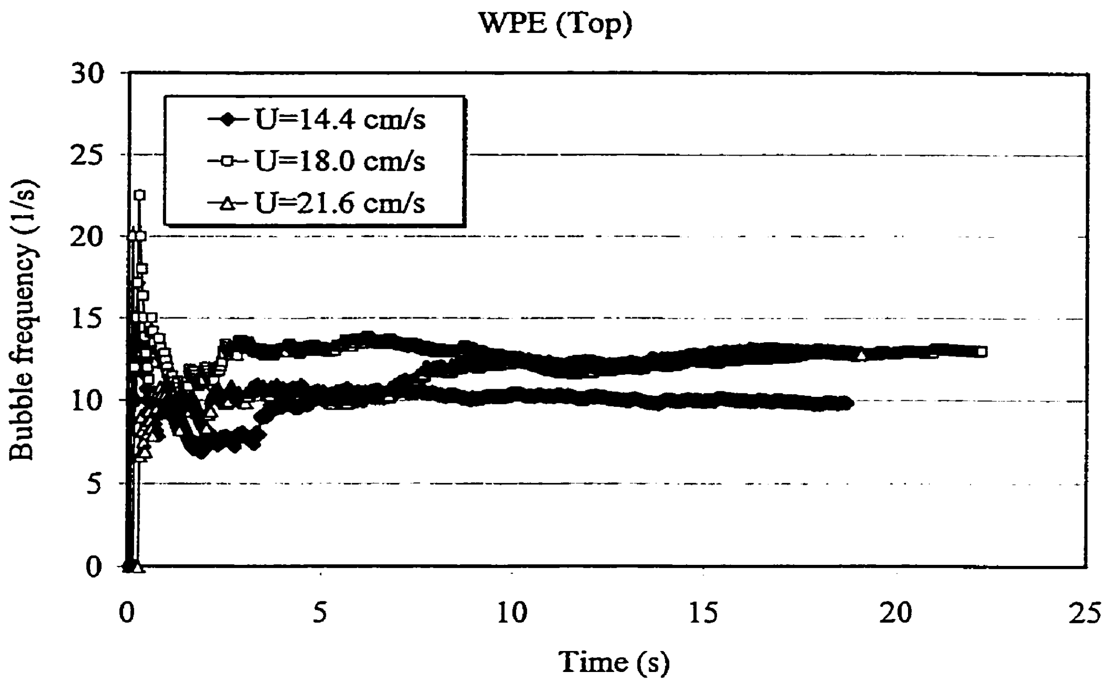

Figure 5.3.4. Image processing results for bubble occurrence frequency for WPE-air system at three superficial gas velocities –top section of the bed

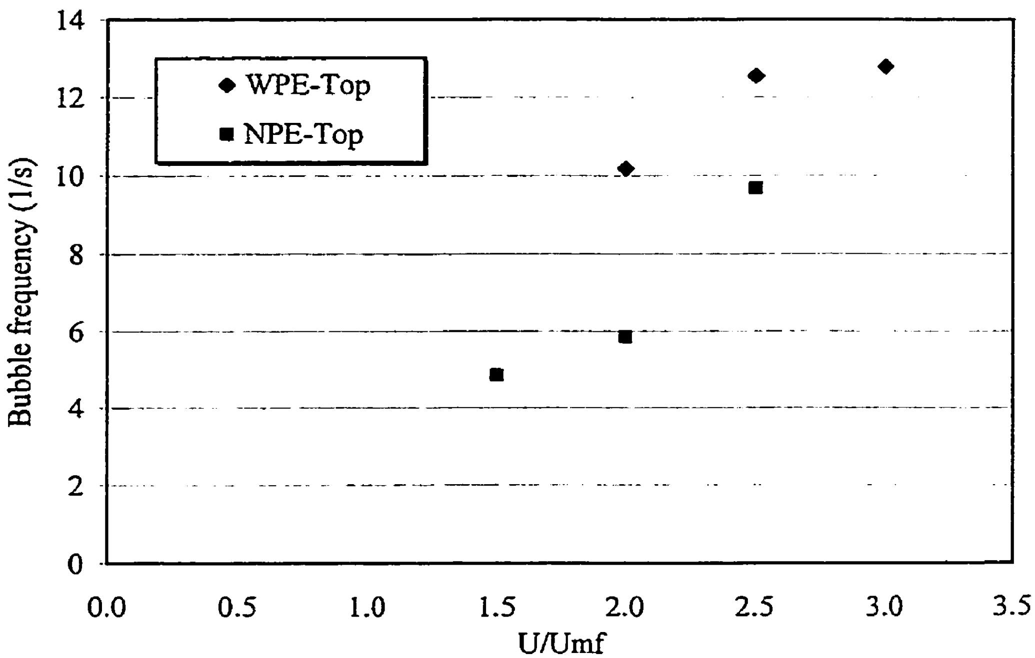

Figure 5.3.5. Comparison of averaged bubble occurrence frequency versus U/U_{mf}, between WPE-air and NPE-air systems -top section of the bed

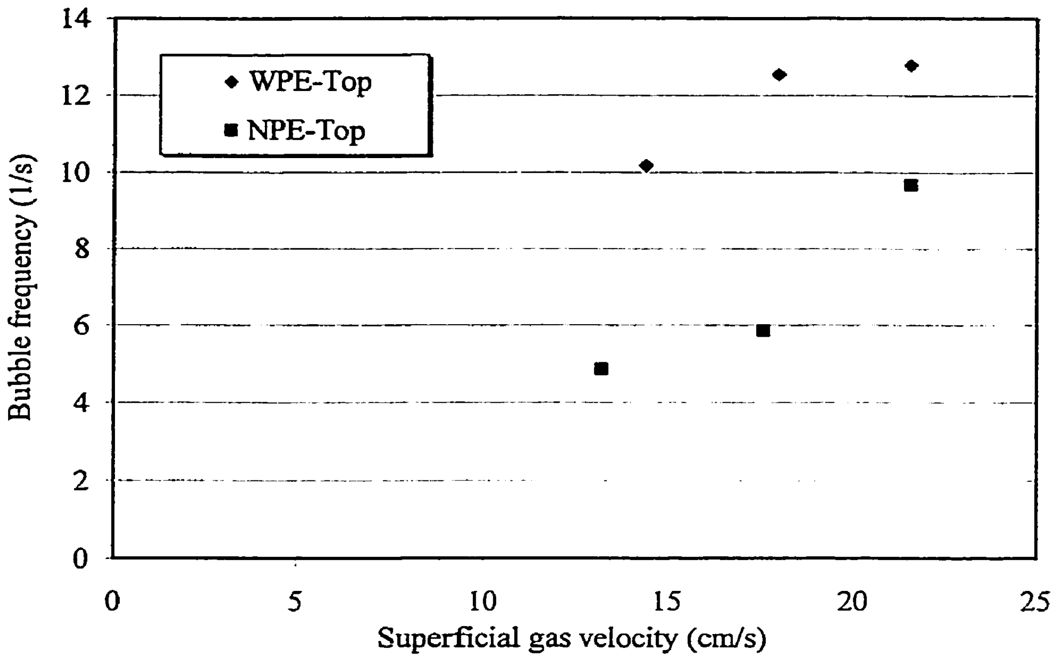

Figure 5.3.6 Comparison of averaged bubble occurrence frequency versus superficial gas velocity, between WPE-air and NPE-air systems -top section of the bed

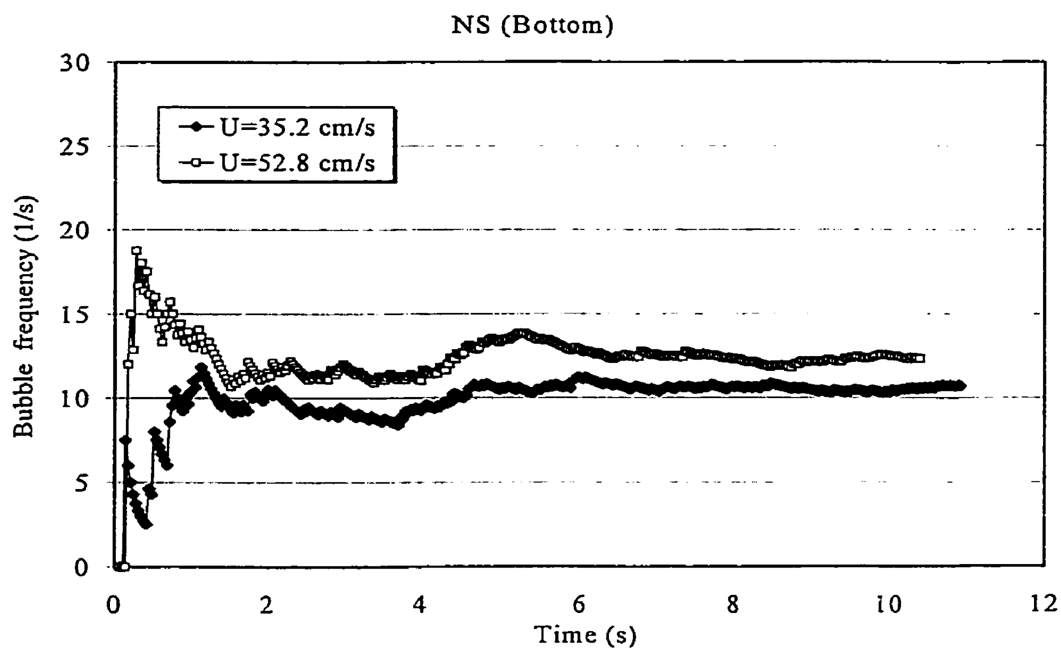

Figure 5.3.7. Image processing results for bubble occurrence frequency for NS-air system at two superficial gas velocities –bottom section of the bed

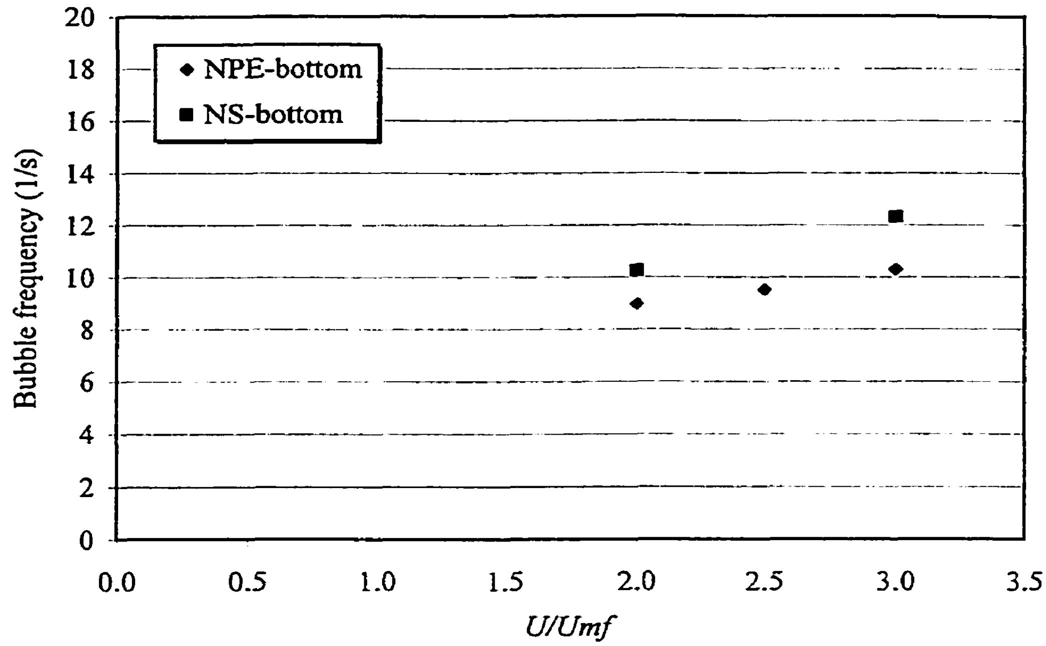

Figure 5.3.8. Comparison of averaged bubble occurrence frequency versus U/U_{mf}, between NS-air and NPE-air systems -bottom section of the bed

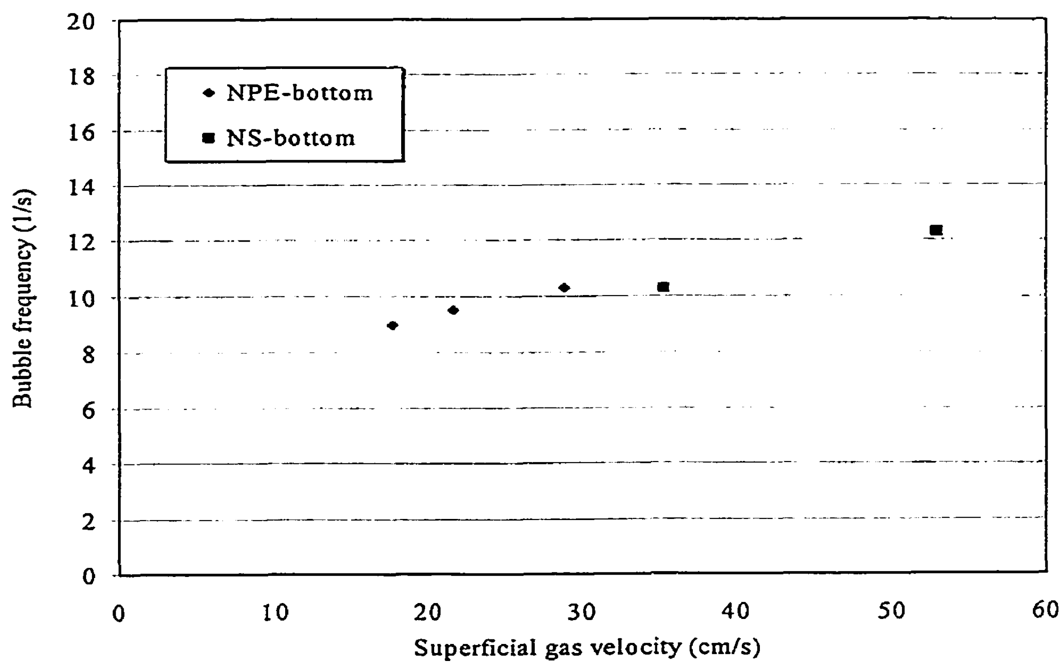

Figure 5.3.9. Comparison of averaged bubble occurrence frequency versus superficial gas velocity, between NS-air and NPE-air systems -bottom section of the bed

5.4. Analysis of Bubble Velocity from Image Processing and Correlations

5.4.1. Analysis of Bubble Velocity from Image Processing

As mentioned in section 5.1, for the NPE-air system, eight sets of images were recorded on videotape. No bubbles were observed in the images taken at the bottom section at superficial gas velocity of 13.2 cm/s (1.5×U_{mf}). Slugging occurred at superficial gas velocity of 28.8 cm/s (3.0×U_{mf}). Therefore, no further processing work was performed for the images of the bottom section of the bed at a superficial gas velocity of 13.2 cm/s and for the images of the top section at superficial gas velocity 28.8 cm/s. However, the image processing of the bottom section of the bed at superficial gas velocity of 28.8 cm/s was performed to study the fluid dynamics of bubble flow at this situation.

Figure D.1 (Appendix D) shows the original results of bubble vertical velocities from image processing for the NPE-air system at the bottom section of the bed at superficial gas velocities of 17.6 cm/s, 21.6 cm/s and 28.8 cm/s. Figure 5.4.1 illustrates the distribution of the bubble vertical velocities for the same conditions. At a superficial gas velocity of 17.6 cm/s, bubble vertical velocities range mainly from 15 to 45 cm/s, while at superficial gas velocities of 21.6 cm/s and 28.8 cm/s, bubble vertical velocities range mainly from 25 to 55 cm/s. Figures 5.4.2 to 5.4.4 present the averaged bubble vertical velocities (diamond points) along the bed height for the three superficial gas velocities. The bubble vertical velocities increase slightly with the increase in height in the bed at each superficial gas velocity.

Figure D.2 (Appendix D) shows the original results of bubble vertical velocity from image processing for the NPE-air top section at the same superficial gas velocities mentioned above. Figure 5.4.5 illustrates the distribution of the bubble vertical velocities for the three superficial gas velocities. With the increase in superficial gas velocity

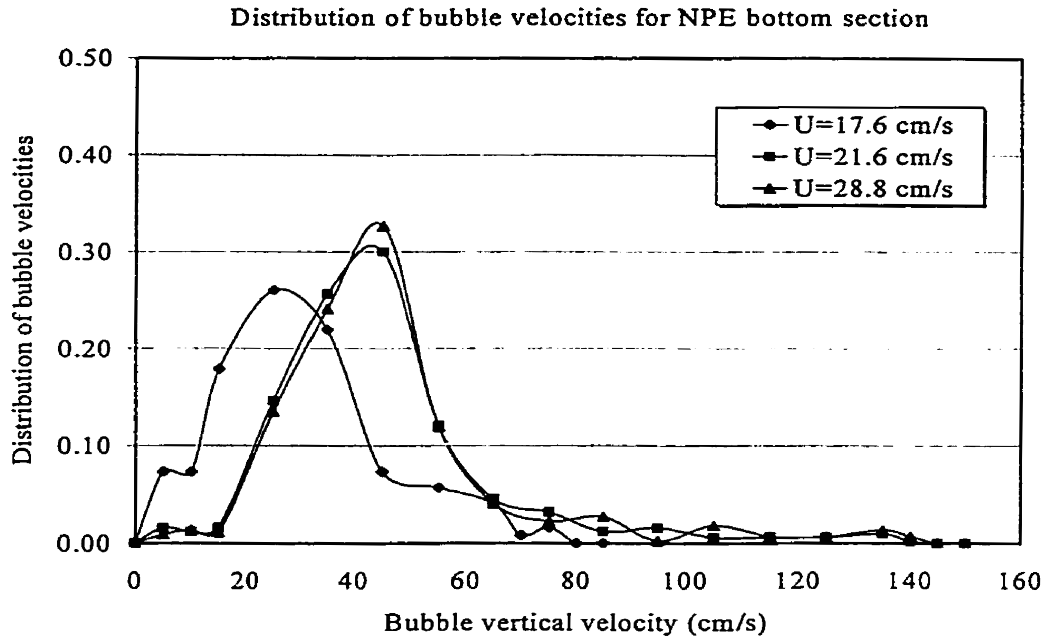

Figure 5.4.1. Distribution of bubble vertical velocities for NPE-air system at the three superficial gas velocities-bottom section of the bed

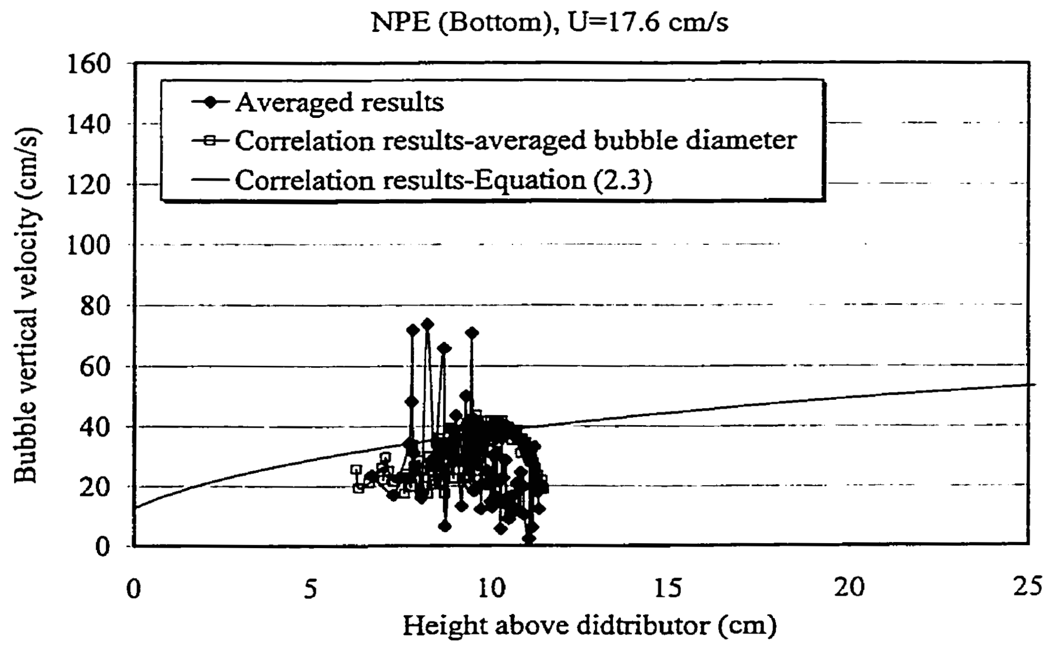

Figure 5.4.2. Averaged bubble vertical velocities for NPE-air system at U=17.6 cm/s-bottom section of the bed

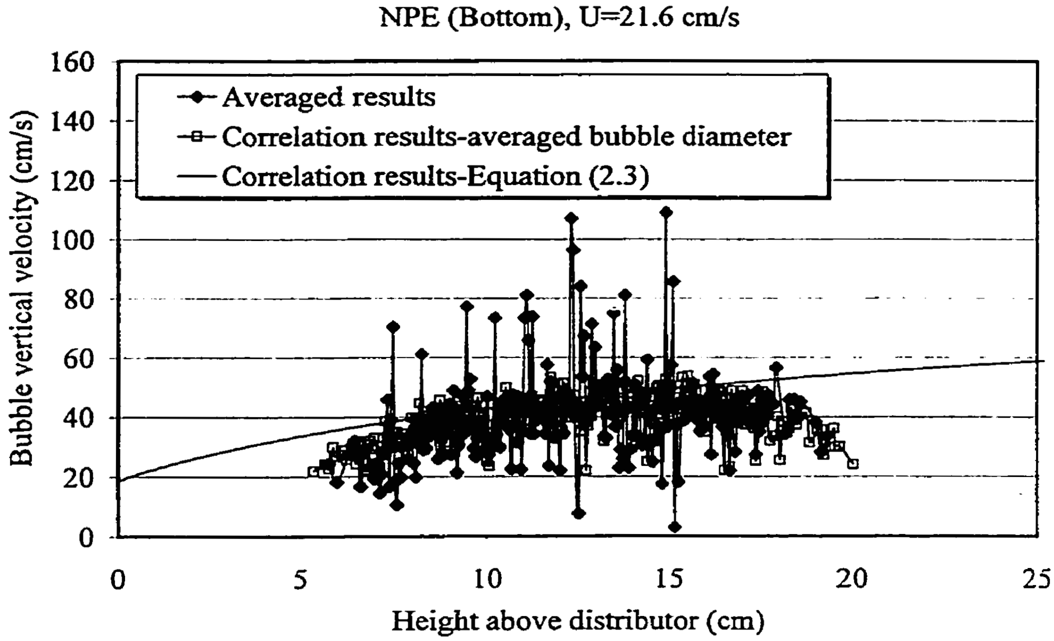

Figure 5.4.3. Averaged bubble vertical velocities for NPE-air system at U=21.6 cm/s-bottom section of the bed

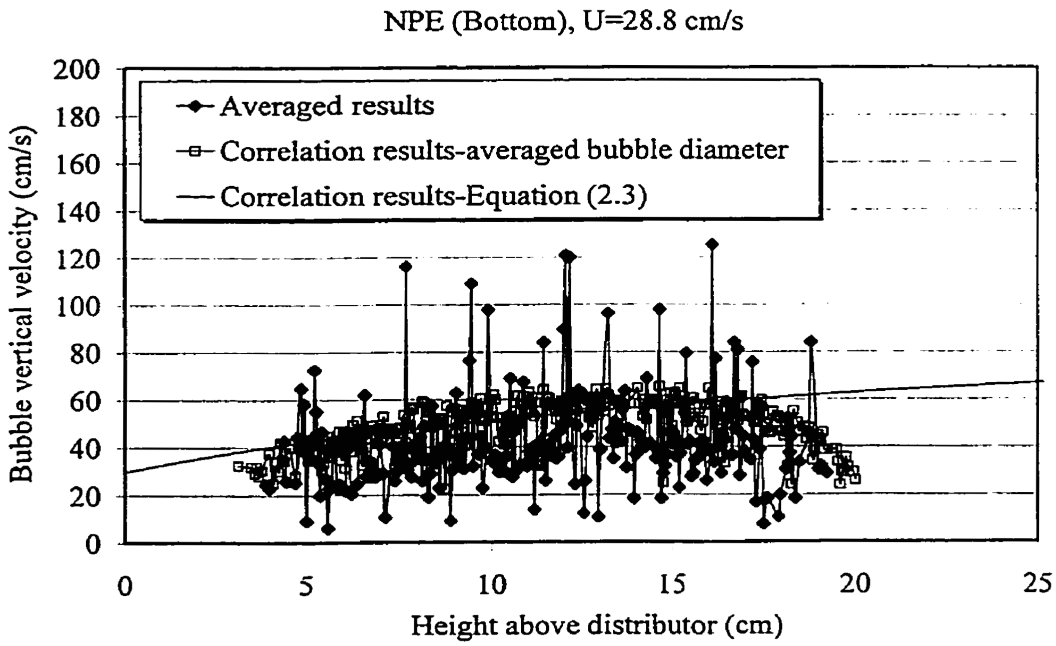

Figure 5.4.4. Averaged bubble vertical velocities for NPE-air system at U=28.8 cm/s-bottom section of the bed

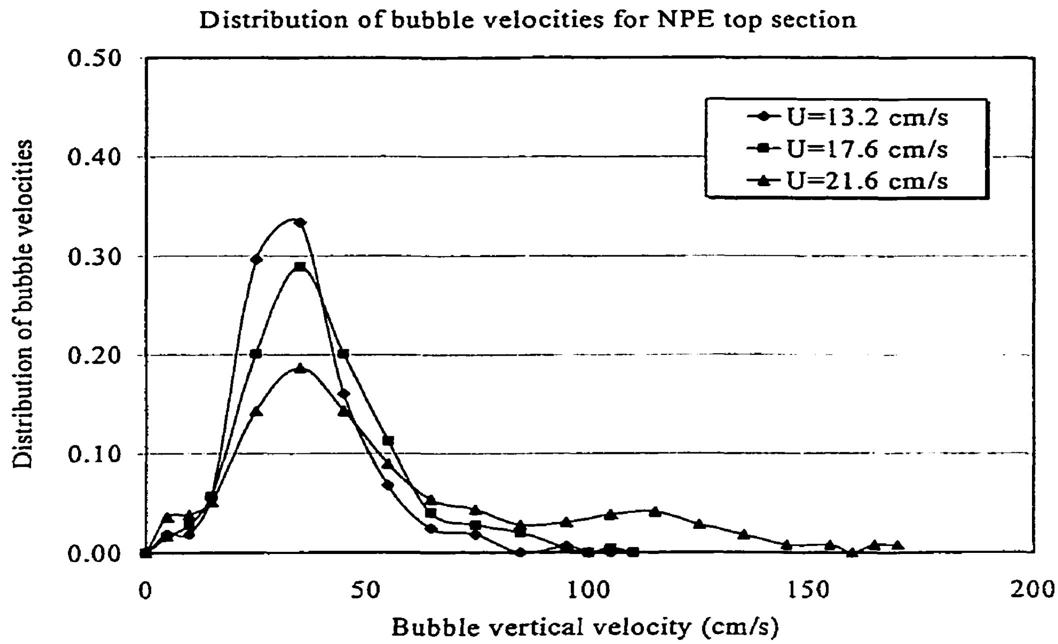

Figure 5.4.5. Distribution of bubble vertical velocities for NPE-air system at the three superficial gas velocities -top section of the bed

bubble vertical velocities increase slightly as shown in Figure D.2. From Figure 5.4.5 one can see that the values of bubble vertical velocities are mainly in the range from 15 to 55 cm/s at lower superficial gas velocity of 13.2 cm/s. However, at higher superficial gas velocities of 21.6 cm/s the percentage in this range is smaller, while the percentage above 55 cm/s is larger. Figures 5.4.6 to 5.4.8 show the averaged bubble vertical velocities along the bed height for the three superficial gas velocities. From these figures, similar trends can be observed. With an increase in superficial gas velocity averaged bubble vertical velocities do not change much and that the bubble vertical velocities increase along the bed height above the distributor for certain superficial gas velocity. It is also clear that at the same superficial gas velocity, bubble vertical velocities increase slightly from the bottom to the top of the fluidized bed.

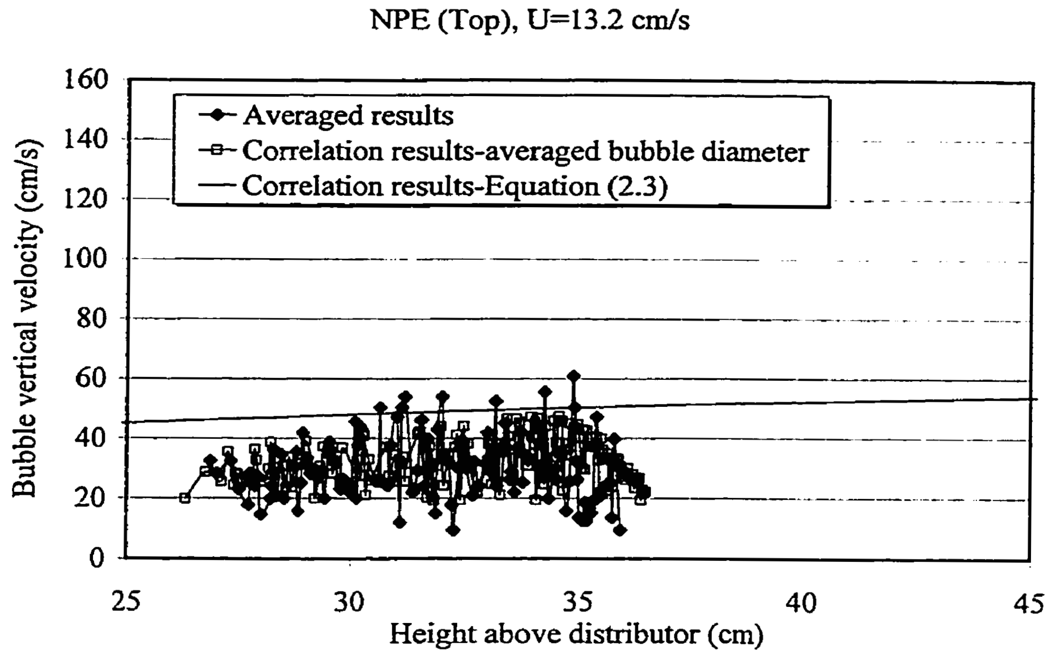

Figure 5.4.6. Averaged bubble vertical velocities for NPE-air system at U=13.2 cm/s –top section of the bed

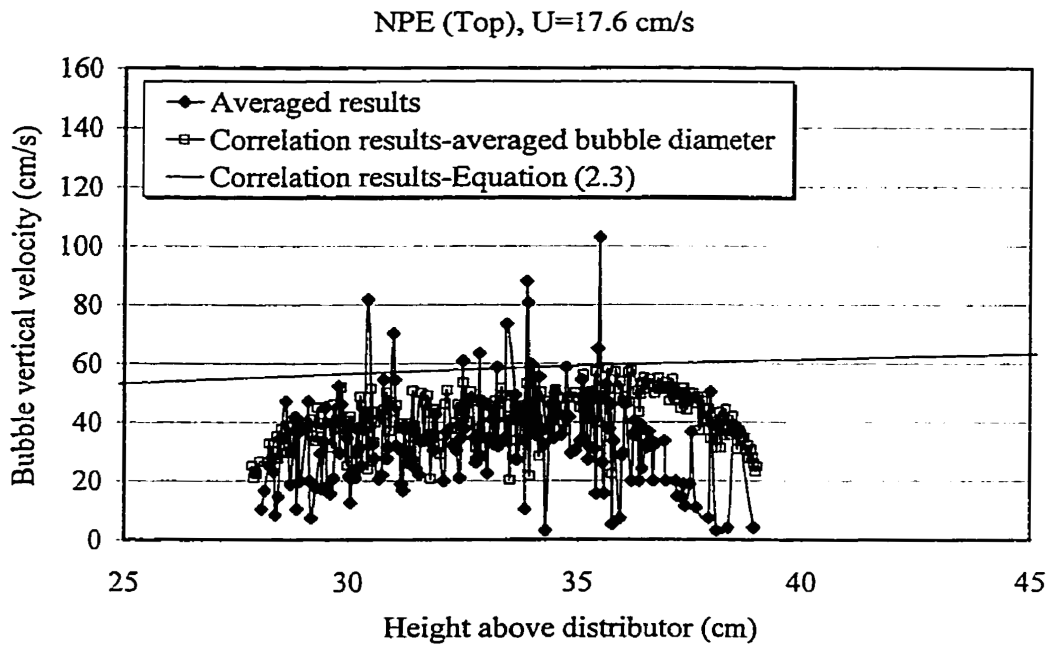

Figure 5.4.7. Averaged bubble vertical velocities for NPE-air system at U=17.6 cm/s –top section of the bed

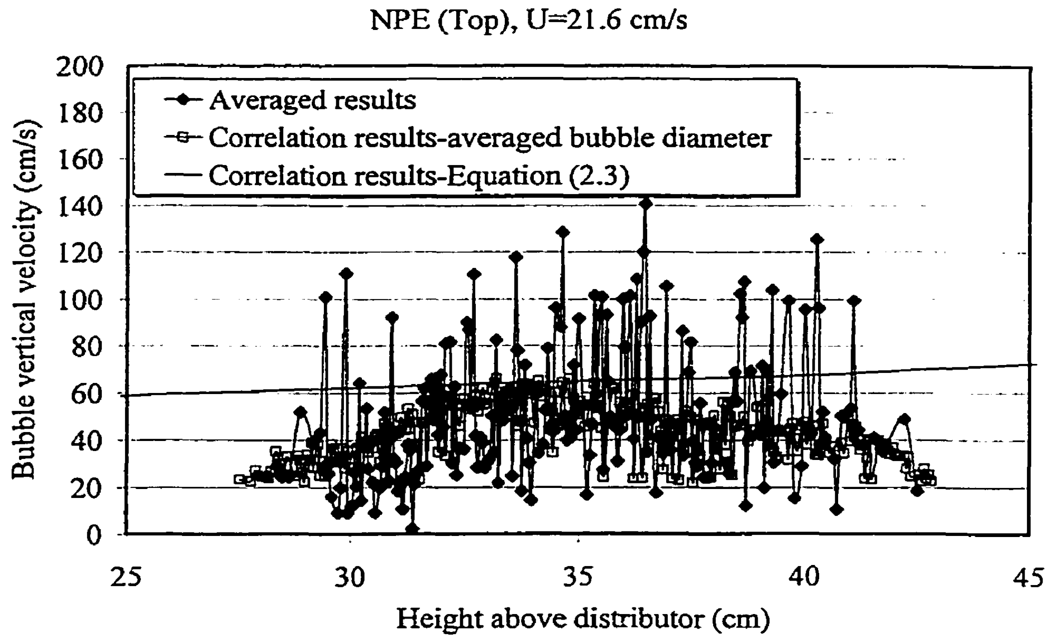

Figure 5.4.8. Averaged bubble vertical velocities for NPE-air system at U=21.6 cm/s –top section of the bed

As mentioned before, for the WPE-air system, eight sets of images were recorded, of which four sets images taken at the bottom of the bed at superficial gas velocities of 10.8 cm/s, 14.4 cm/s, 18.0 cm/s and 21.6 cm/s were not processed since no bubbles were observed in the images.

Figure D.3 (Appendix D) shows the original results of bubble vertical velocity from image processing versus the bed height above the distributor for the WPE-air system (top section of the bed) at three different superficial gas velocities. With an increase in superficial gas velocity bubble vertical velocities increase slightly. Figure 5.4.9 displays the distribution of the bubble vertical velocities for the three superficial gas velocities. From the figure one can see similar distributions to those for the NPE-air system at the top section of the bed. The values of bubble vertical velocities mainly fall into the range from 15 to 75 cm/s at lower superficial gas velocity of 14.4 cm/s. However, at higher superficial gas velocity there are more points with bubble vertical velocities above 75 cm/s. In Figures 5.4.10 to 5.4.12 the diamond points are the averaged bubble vertical velocities from image processing while the square points are those predicted from correlation that will be discussed later. Similarly, with an increase in superficial gas velocity, bubble vertical velocities increase slightly and the bubble vertical velocities increase slightly along the bed height for a certain superficial gas velocity.

One may recall that for the NS-air system, four sets of images were recorded, of which two sets taken at the top section of the bed at superficial gas velocities of 35.2 cm/s and 52.8 cm/s, were not processed due to the slugging observed in the images.

The original results for bubble vertical velocity obtained from image processing for the NS-air system at the bottom section of the bed are shown in Figure D.4 (Appendix D) at the two superficial gas velocities investigated in this study. Figure 5.4.13 presents the distribution of the bubble vertical velocities for the same conditions. The trends are very similar to those discussed above. In Figures 5.4.14 to 5.4.15 the diamond points present the averaged bubble vertical velocities obtained from image processing. Those predicted by correlations are also shown.

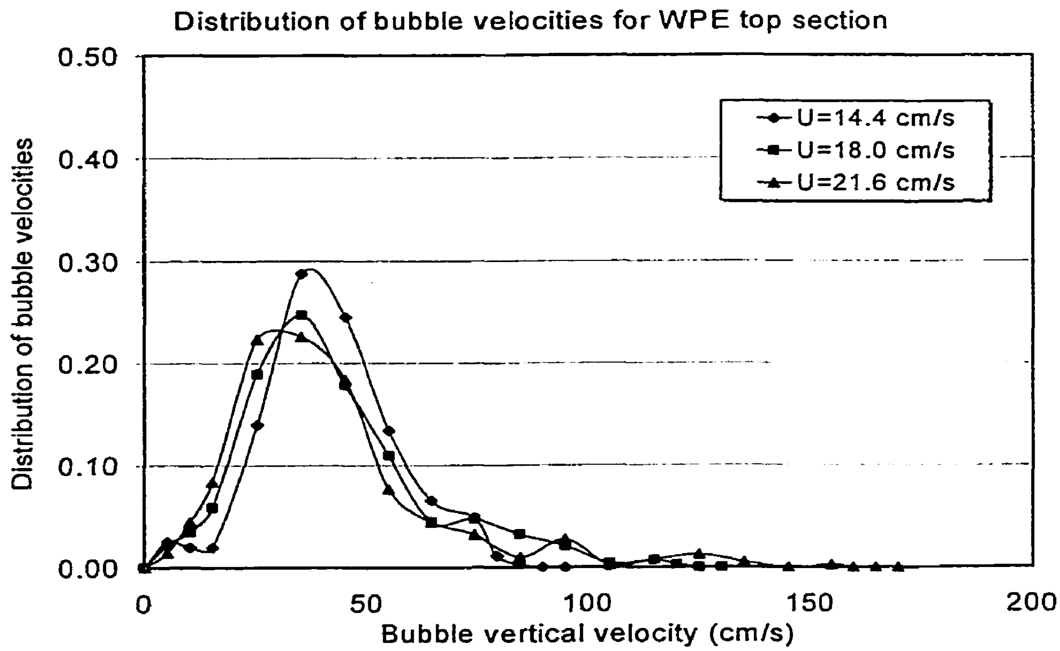

Figure 5.4.9. Distribution of bubble vertical velocities for WPE-air system at the three superficial gas velocities -top section of the bed

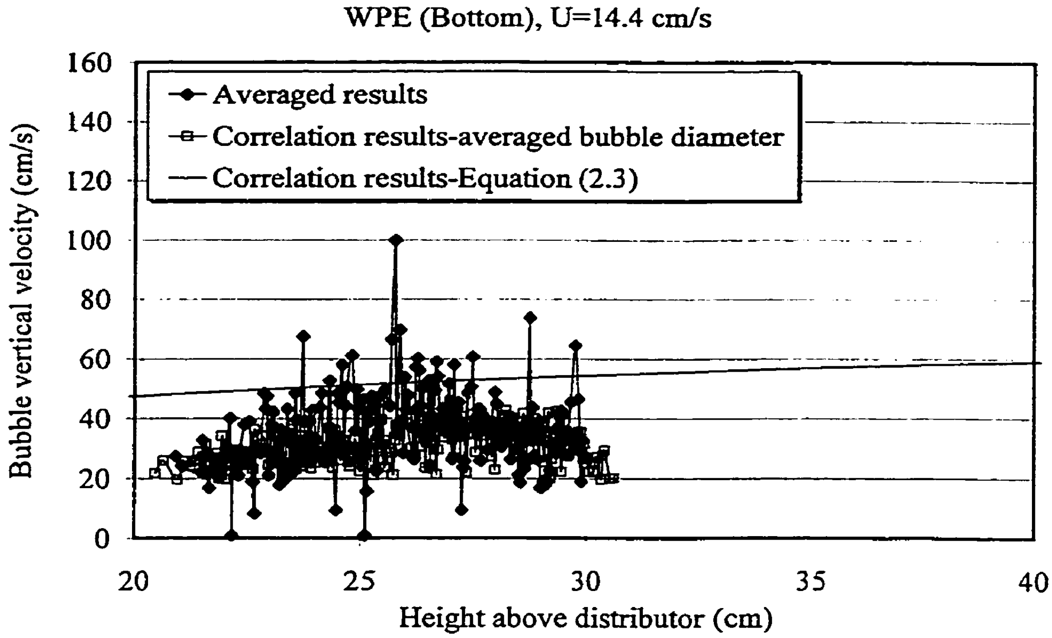

Figure 5.4.10. Averaged bubble vertical velocities for WPE-air system at U=14.4 cm/s – top section of the bed

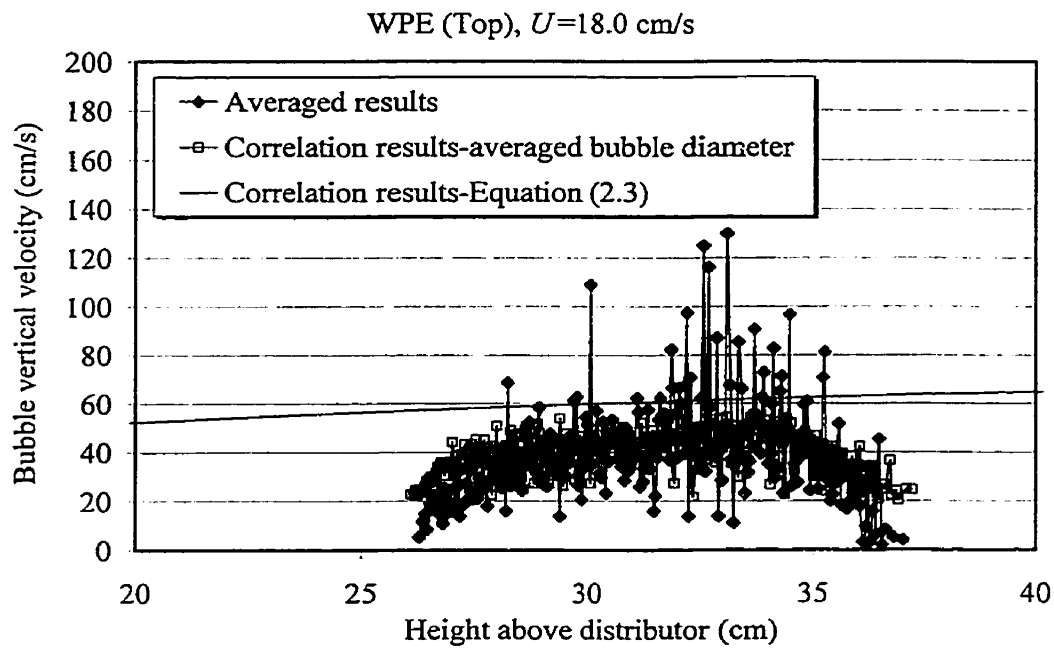

Figure 5.4.11. Averaged bubble vertical velocities for WPE-air system at U=18.0 cm/s – top section of the bed

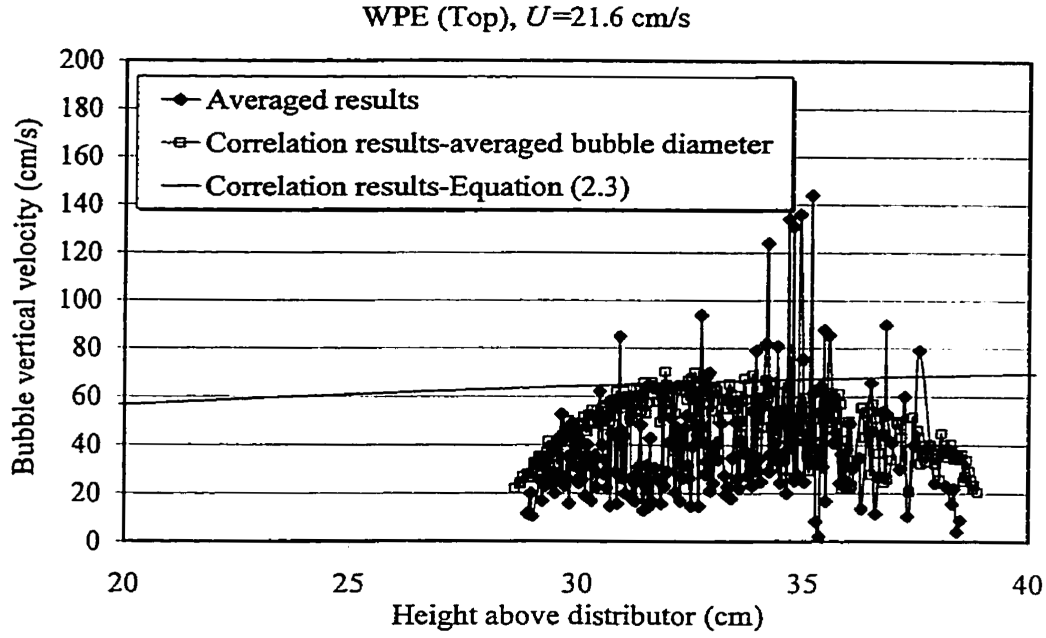

Figure 5.4.12. Averaged bubble vertical velocities for WPE-air system at U=21.6 cm/s-top section of the bed

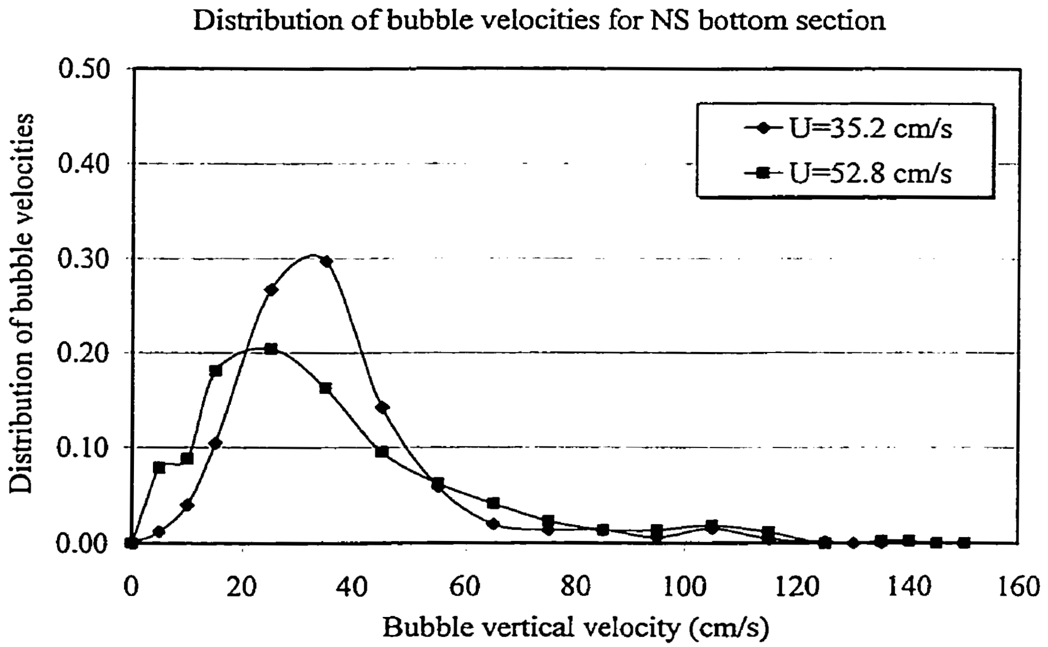

Figure 5.4.13. Distribution of bubble vertical velocities for NS-air system at the three superficial gas velocities -bottom section of the bed

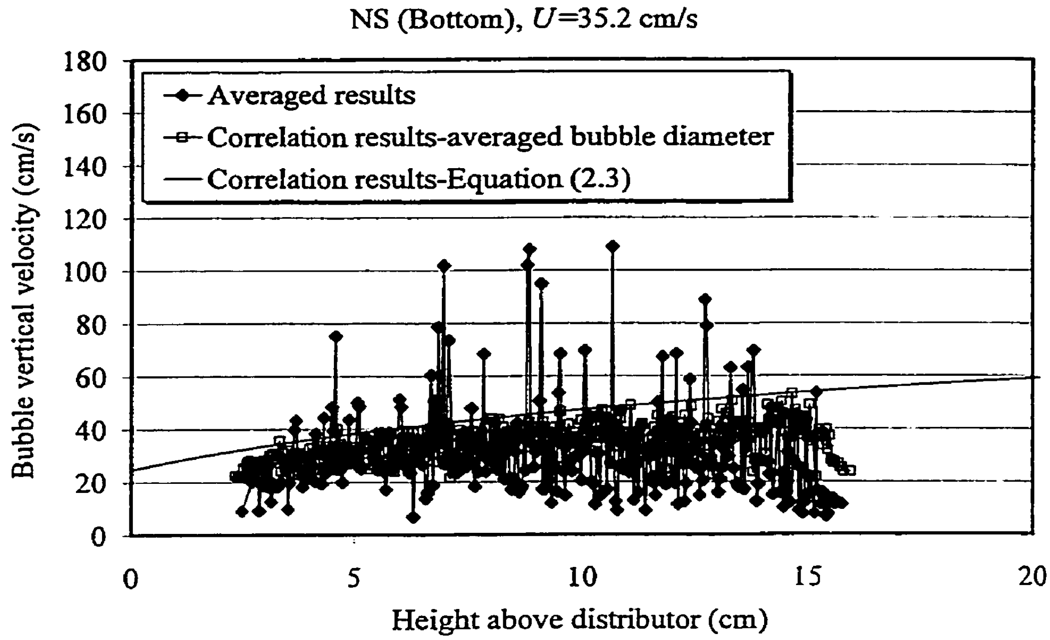

Figure 5.4.14. Averaged bubble vertical velocities for NS-air system at U=35.2 cm/s – bottom section of the bed

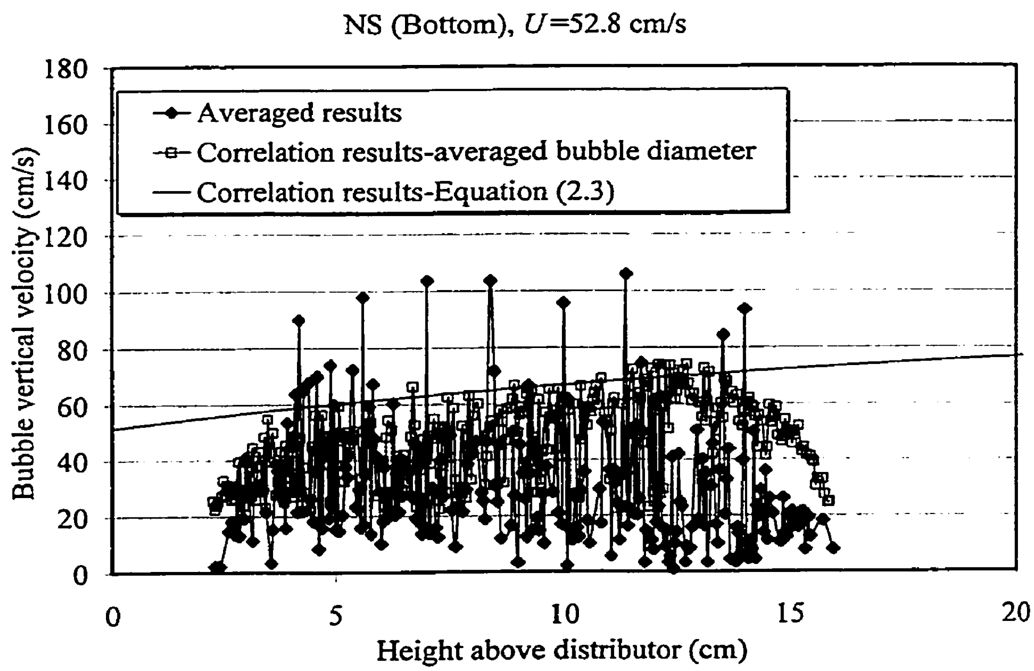

Figure 5.4.15. Averaged bubble vertical velocities for NS-air system at U=52.8 cm/s – bottom section of the bed

From the discussion above, a general conclusion can be reached for the three systems studied in this work. Bubble rising velocity increases slightly with an increase in superficial gas velocity and with the bed height. This increase is consistent with and can be explained by the changing patterns in bubble size as discussed in the previous section. Generally, it is accepted that larger bubbles in fluidized beds lead to higher rising velocities (Kunii and Levenspiel, 1991). One should, however, be aware of that this is true only in the time and population averaged points of view since fluidization is a very complicated process in which bubbles have a very wide distribution in their size and shape, and bubbles are in a dynamic state locally.

Figures 5.4.16, 5.4.17, 5.4.18 and 5.4.19 show bubble horizontal velocities versus the bed height at different operating conditions. Positive horizontal velocity indicates that the bubble moves to the right in the image frame and negative horizontal velocity to the left. All the bubble horizontal velocities fluctuate around zero along the height above the distributor. At higher superficial gas velocities, the degree of fluctuation is slightly higher than that at lower superficial gas velocities. It can be assumed that bubbles in fluidized beds move randomly in the horizontal/radial direction, which is favorable to the gas phase mixing in the beds. It should be noted that the horizontal velocity measured in this study is a projection of the radial velocity of the bubble, due to the fact that the current imaging system is 2-D in nature. Another type of imaging system is needed in order to obtain 3-D velocity data.

The difference in bubble flow dynamics between top section and bottom section of the fluidized bed was also investigated in this study. The difference is illustrated in Figure 5.4.20, which was obtained by averaging all the population of bubble vertical velocity data at both top and bottom sections for the NPE-air system at each superficial gas velocity. From the figure it is clear that bubble vertical velocity at the top section of the bed is higher than that at the bottom section of the bed. The reason is that the bubble size at the top section is slightly larger than that at bottom section.

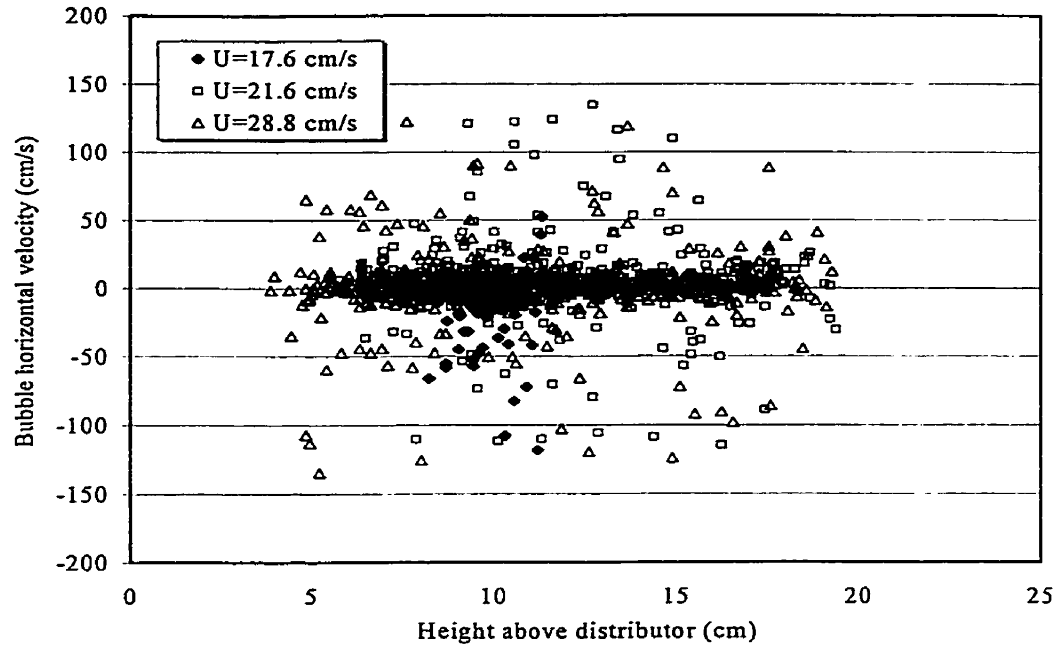

Figure 5.4.16. Image processing results for bubble horizontal velocity for NPE-air system at three superficial gas velocities-bottom section of the bed

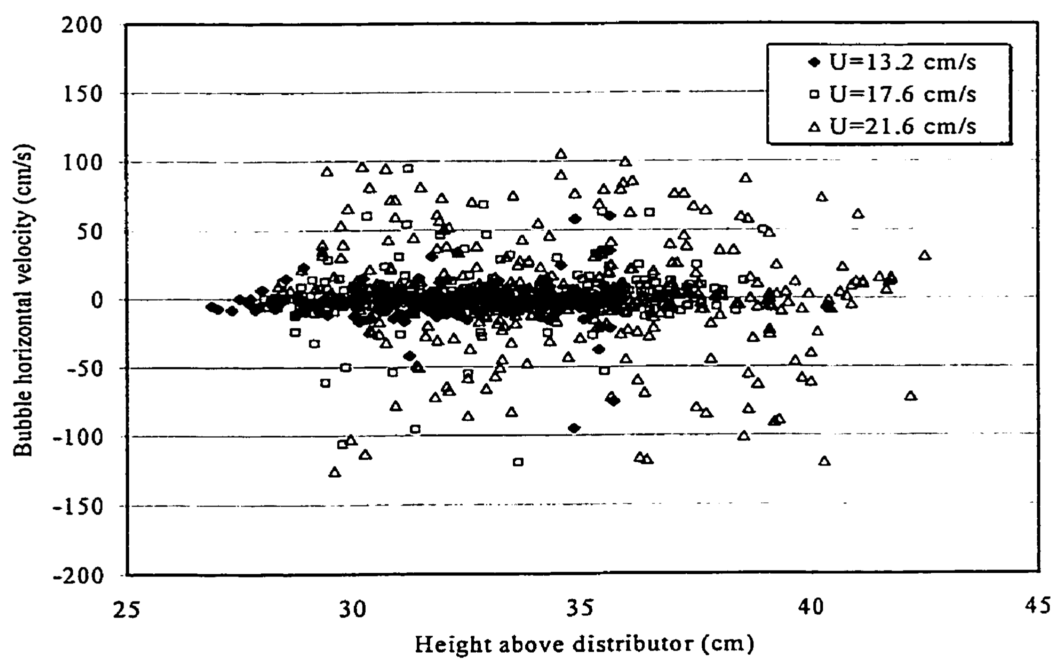

Figure 5.4.17. Image processing results for bubble horizontal velocity for NPE-air system at three superficial gas velocities –top section of the bed

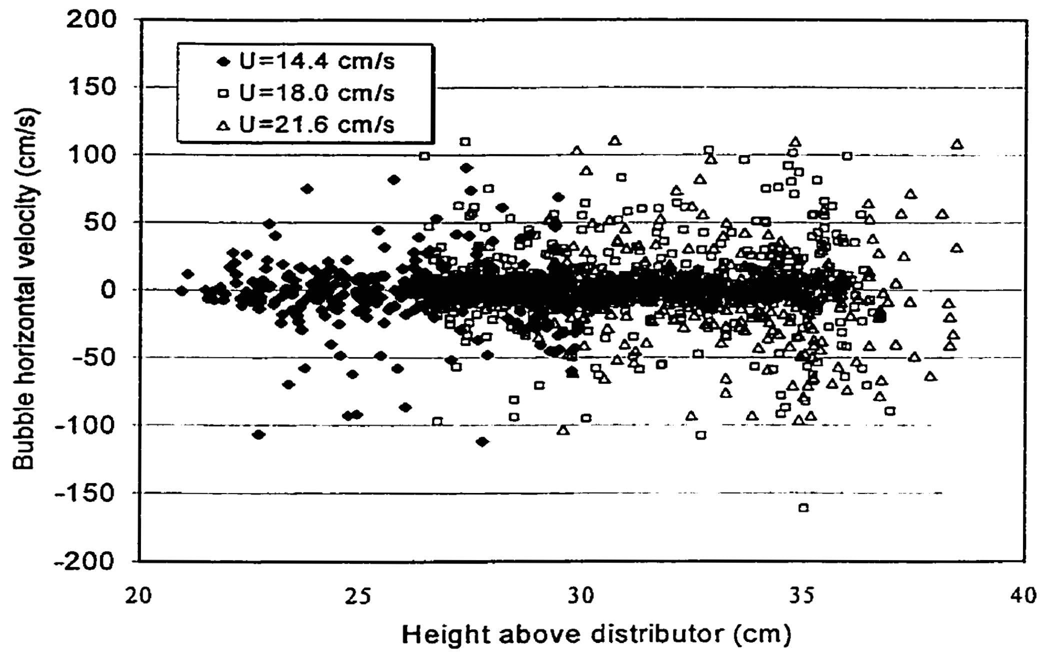

Figure 5.4.18. Image processing results for bubble horizontal velocity for WPE-air system at three superficial gas velocities –top section of the bed

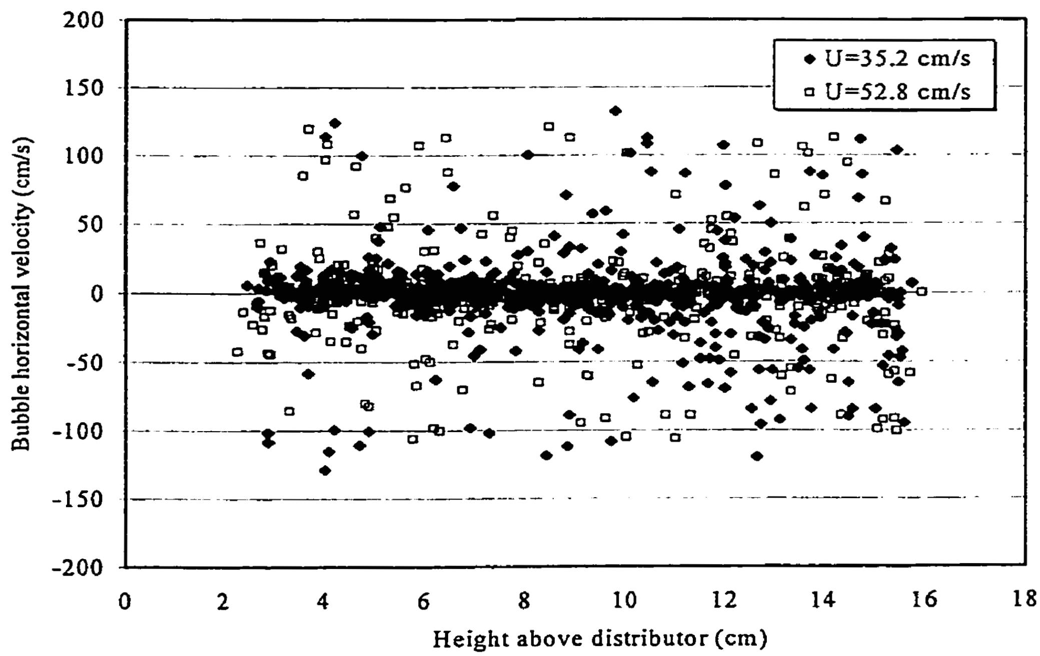

Figure 5.4.19. Image processing results for bubble horizontal velocity for NS-air system at two superficial gas velocities –bottom section of the bed

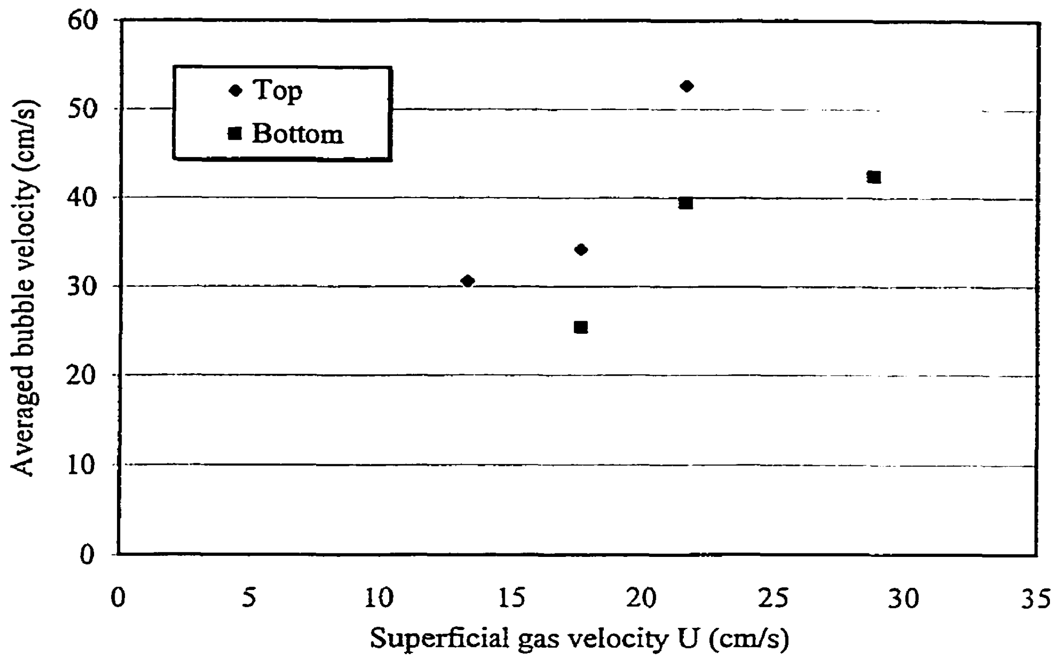

Figure 5.4.20. Averaged bubble vertical velocity for NPE-air system –comparison between top and bottom sections

Study of bubble flow dynamics in fluidized beds of polyethylene particles has not been reported in open literature so far. In order to investigate the difference in bubble flow dynamics between sand and polyethylene particles, comparisons were performed as shown in Figures 5.4.21 and 5.4.22. Figure 5.4.21 is for averaged bubble vertical velocities over the whole population of each image set versus U/U_{mf}. From this figure one can see that with an increase in superficial gas velocity averaged bubble vertical velocity increases for the NPE-air system while it remains almost constant for the NS-air system. It is also noted from Figures 5.4.21 that at the same U/U_{mf}, the bubble vertical velocity in the NPE-air system is slightly lower than that in the NS-air system at $2.0\times U_{mf}$, and is higher than that in NS-air system at $3.0\times U_{mf}$. The possible reason is that the two systems have very different bubble flow patterns at the bottom section of the bed, which will be discussed in section 5.4.2. Figure 5.4.22 shows the averaged bubble vertical velocity versus superficial gas velocity. Since the NS-air system and the NPE-air system have different U_{mf} the two data sets are further away from each other. The trends, however, are similar to those observed in Figure 5.4.21.

Figures 5.4.23 and 5.4.24 present a comparison of averaged bubble vertical velocity between the NPE-air and WPE-air systems. The averaged bubble vertical velocity increases when the value of U/U_{mf} increases for the NPE-air system, while it increases slightly for the WPE-air system. Figure 5.4.24 shows similar trends to those in Figure 5.4.23 since for NPE and WPE particles the minimum fluidization velocities are close to each other. As noted in Figure 5.4.23 and 5.4.24, the difference in bubble vertical velocity for the two systems is significant at higher U/U_{mf} while the difference is small at lower U/U_{mf}. Due to the limited number of points, experimental data at more different superficial gas velocities are needed before such a general conclusion is reached.

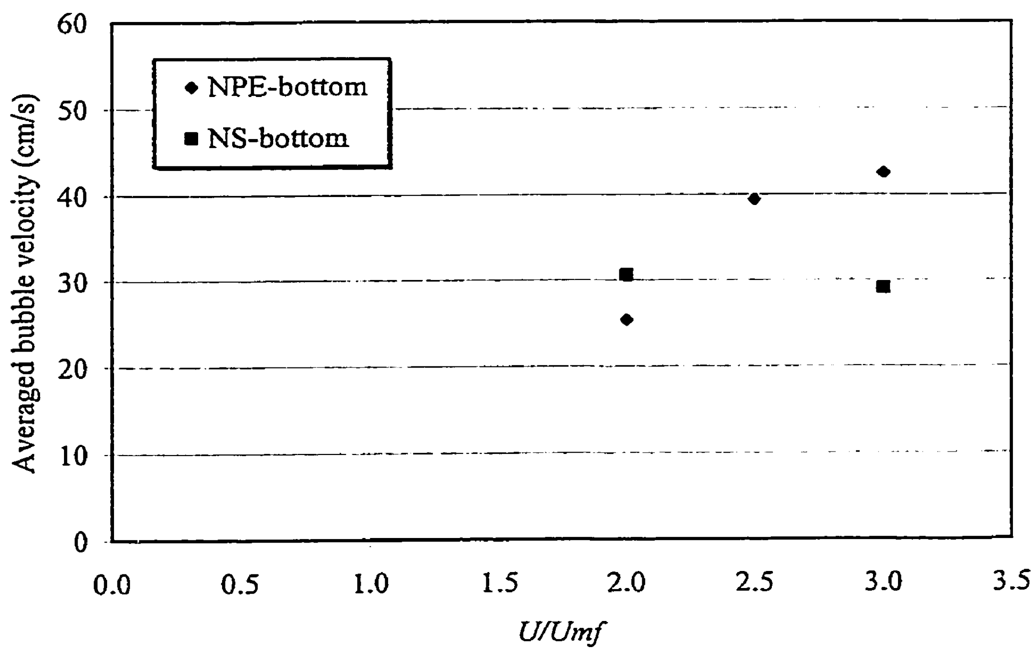

Figure 5.4.21. Averaged bubble vertical velocity versus U/U_{mf} for NPE-air and NS-air systems- bottom section of the bed

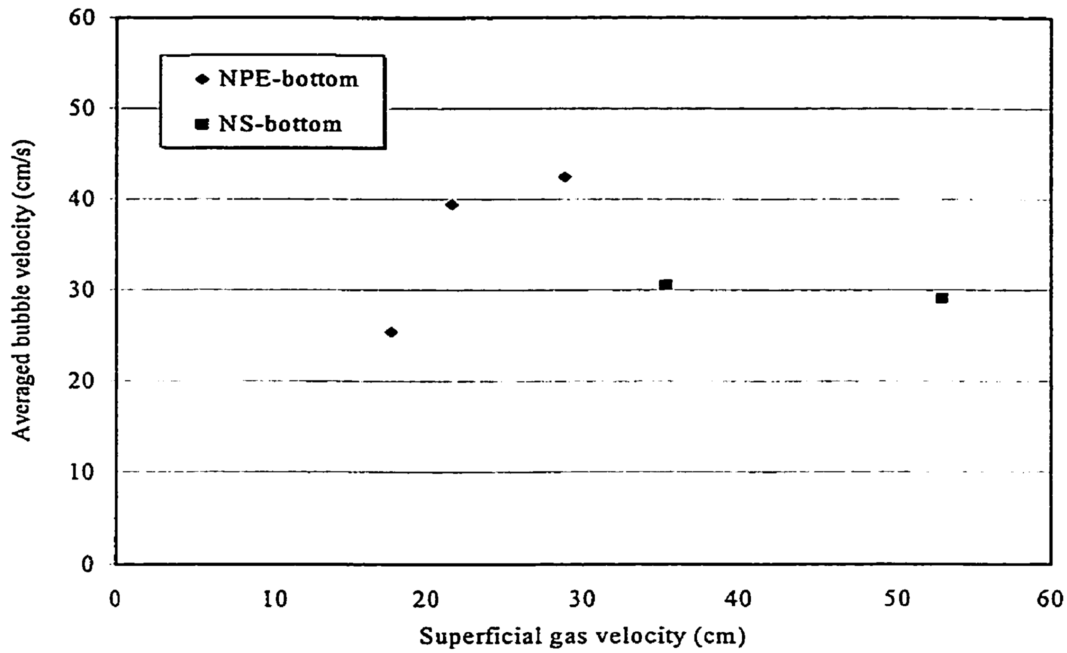

Figure 5.4.22. Averaged bubble vertical velocity versus superficial gas velocities for NPE-air and NS-air systems- bottom section of the bed

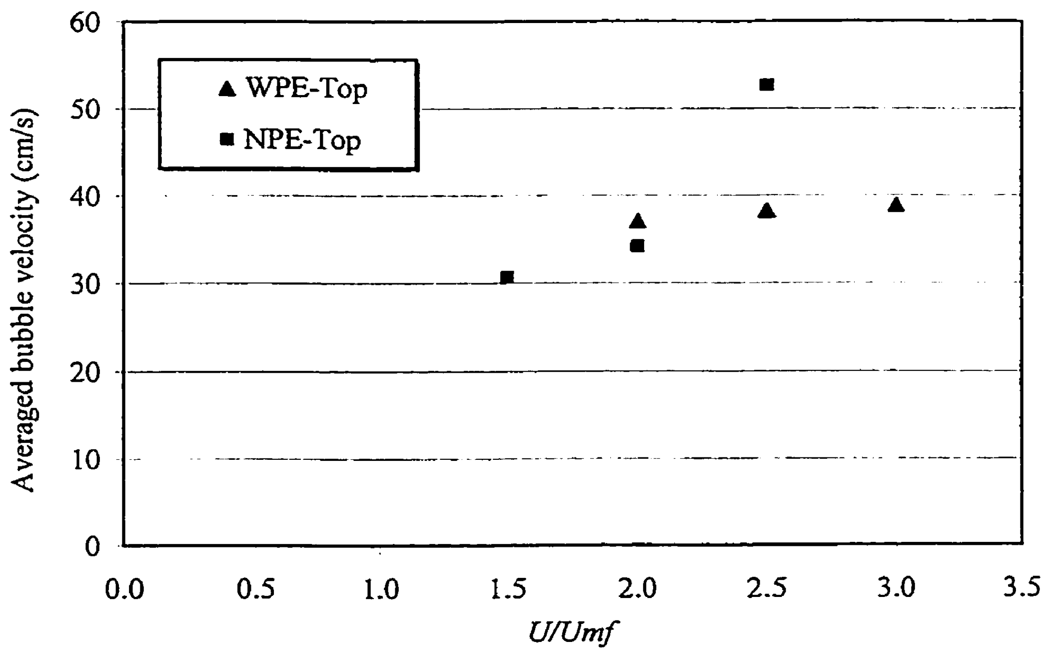

Figure 5.4.23. Averaged bubble vertical velocity versus U/U_{mf} for NPE-air and WPE-air systems- top section of the bed

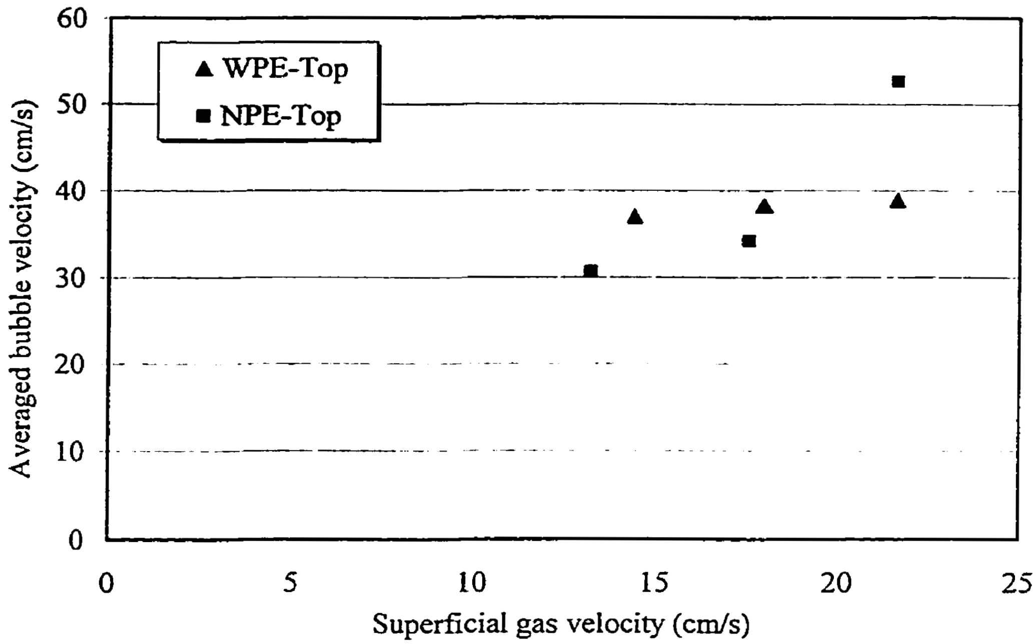

Figure 5.4.24. Averaged bubble vertical velocity versus superficial gas velocities for NPE-air and WPE-air systems- top section of the bed

5.4.2. Prediction of Bubble Rising Velocity by Correlations

Correlations for predicting bubble rising velocities in fluidized beds have been reviewed in Chapter 2. Several correlations have been proposed by Davidson and Harrison (1963), Werther (Kunii and Levenspiel, 1991) and Kunii and Levenspiel (1991). Davidson and Harrison's correlation is based on simple two-phase theory which does not fit experimental findings well (Kunii and Levenspiel 1991). In order to come up with an equation for bubble rising velocity that covers the whole range of particle sizes from Geldart A to D, Werther (Kunii and Levenspiel, 1991) proposed his bubble rising velocity correlations. It is considered that Werther's correlations are complicated compared to others. If there are no other correlations available, for example for Geldart D particles, his correlations can be used to provide an estimation of bubble rising velocities. Kunii and Levenspiel's correlations, Equations (2.16) and (2.17) are more suitable for Geldart B particles and therefore employed to predict bubble rising velocity for the systems investigated in this study. Comparisons were then performed for all the data sets studied in the current work. In Equations (2.16) and (2.17), d_b is bubble diameter in fluidized beds. To calculate bubble rising velocity along bed height, bubble diameter values at the corresponding axial position have to be evaluated first.

There are two ways to obtain bubble diameter values in the current work. One is to predict them by the correlations and the other one is to use the image processing results, both of which have been discussed in section 5.1. Therefore, prediction of bubble rising velocity was performed with the bubble diameters obtained in both ways. By using the bubble diameters predicted from correlation Equation (2.3), the bubble rising velocities were obtained along the bed height and shown as solid lines in Figures 5.4.2 to 5.4.4, 5.4.6 to 5.4.8, 5.4.10 to 5.4.12 and 5.4.14 to 5.4.15. For the bottom sections (Figures 5.4.2 to 5.4.4 and 5.4.14 to 5.4.15), the predicted bubble rising velocities are slightly higher than those obtained from image processing. For the top sections (Figures 5.4.6 to 5.4.8 and 5.4.10 to 5.4.12), the predicted ones are higher than measured ones. This discrepancy is probably caused by the over prediction of bubble diameter discussed in section 5.1.

By using time-averaged bubble diameters obtained from image processing in this work, the bubble rising velocities predicted by equations (2.16) and (2.17) are shown as scattered points in Figures 5.4.2 to 5.4.4, 5.4.6 to 5.4.8, 5.4.10 to 5.4.12 and 5.4.14 to 5.4.15. Time-averaged data are global indicator correlating to operating parameters, which is useful to compare with literature. From these figures, one can see that the predicted values of bubble rising velocities are close to those obtained from image processing, though the points representing the results from image processing seem more scattered than these predicted ones. The relative deviation is around 10 % between averaged image processing results and averaged correlation results for all image sets. This indicates that once the bubble diameter values are properly estimated or measured from experiments, Kunii and Levenspiel's correlation can provide good prediction of bubble rising velocities for Geldart B particles.

5.5. Bubble Flow Patterns

As discussed earlier, both vertical velocity and horizontal velocity of every single bubble tracked were obtained by image processing in this study. It would be of interest to know the flow patterns (the magnitude and direction) of all the bubbles counted in one case, that is a time averaged bubble flow patterns. The bubble flow patterns for all the cases studied are represented as vector plots shown in Figures 5.5.1 to 5.5.9 by using TECPLOT software. The vertical coordinate in these figures refers to the height above the distributor plate. The arrow starts at bubble center. It is the image processing software developed in this work that makes it possible to get bubble vertical and horizontal velocity information and therefore the bubble flow patterns from hundreds of images at various conditions and for different systems. This kind display of bubble flow patterns in gas fluidized beds have not been reported in the open literature to the best of our knowledge. For a gas-liquid system, liquid flow patterns in bubble columns have been reported (for example, Chen *et al.*, 1998).

In the vector plots, Figures 5.5.1, 5.5.2 and 5.5.3, for the NPE-air bottom section, there is no bubble at the region close to the distributor at all three superficial gas velocities. One reason is that the original images were taken for the bottom section at 2 cm above the porous plate distributor, therefore the region from 0 to 2 cm above the distributor was not included in this study. At U=17.6 cm/s, no bubbles are observed in the region from 2 cm to 6.6 cm above the distributor as seen in Figure 5.5.1. At U=21.6 cm/s and U=28.8 cm/s, the region without bubbles is from 2 cm to 5.6 cm and from 2 cm to 3.6 cm, respectively, as shown in Figures 5.5.2 and 5.5.3. The height of the region without bubbles narrows down with the increase in superficial gas velocities. The reason may be that after the gas passes through the porous plate distributor tiny bubbles are formed. Some distance is needed for the tiny bubbles to coalesce into large enough bubbles to be above the threshold established in this study. Increased gas velocity increases the number of tiny bubbles, leading to more coalescence and therefore shorter distance for the formation of large bubbles.

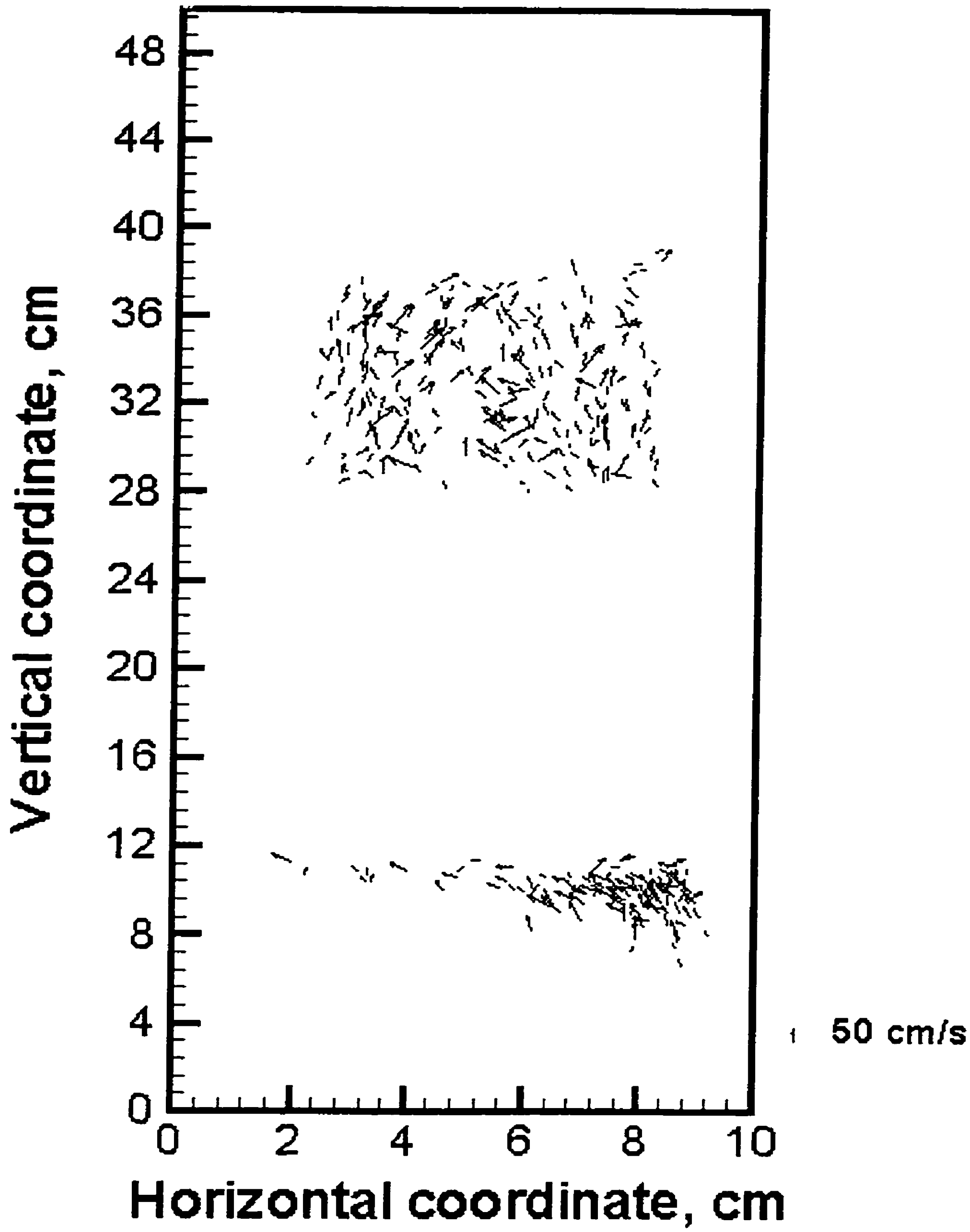

Figure 5.5.1. Bubble velocity vector plot for NPE-air system at U=17.6 cm/s

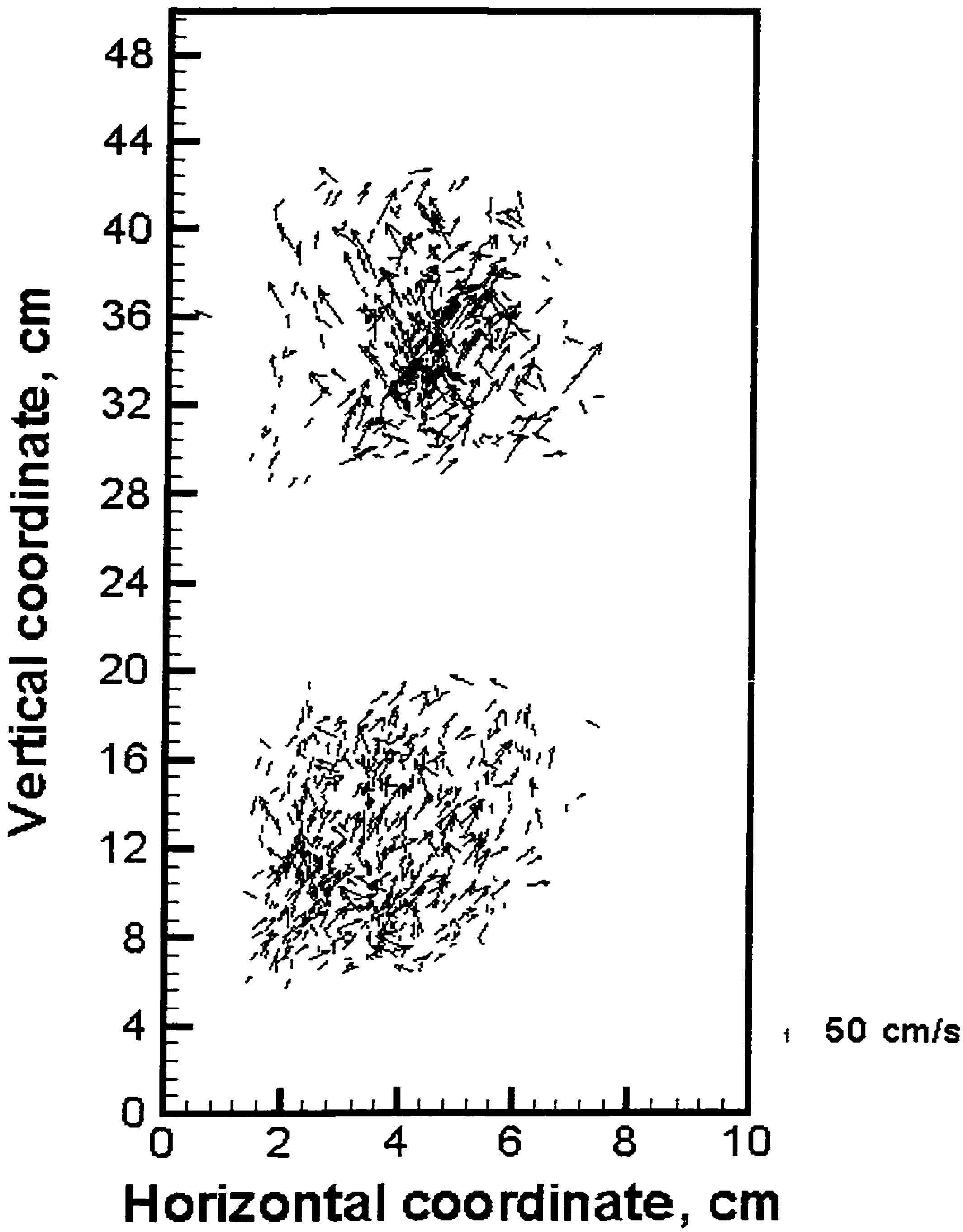

Figure 5.5.2. Bubble velocity vector plot for NPE-air system U=21.6 cm/s

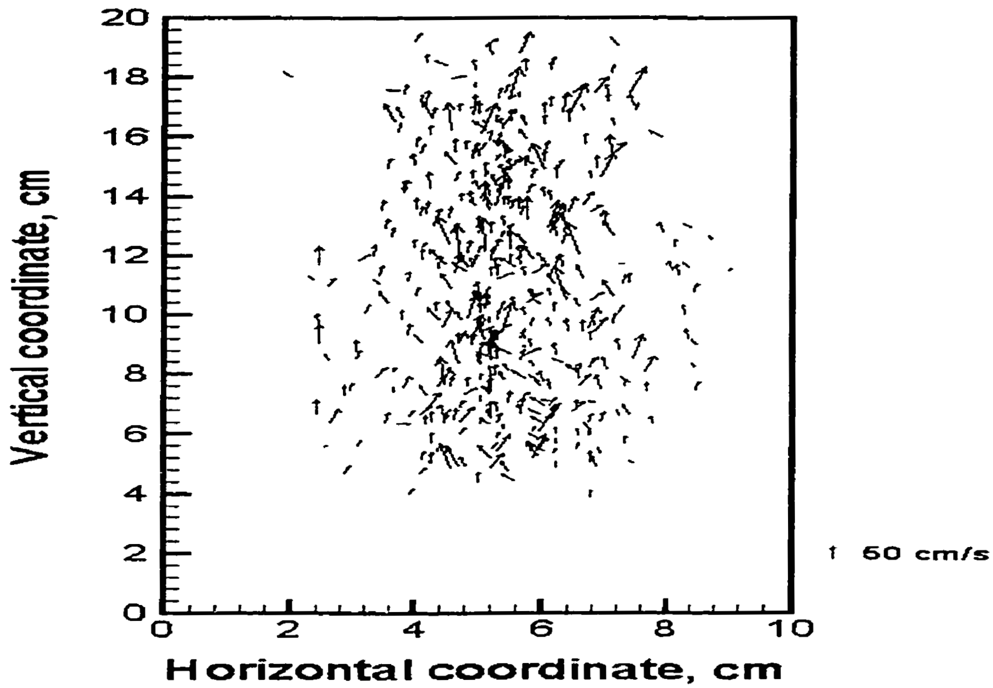

Figure 5.5.3. Bubble velocity vector plot for NPE-air system at U=28.8 cm/s –bottom section of the bed

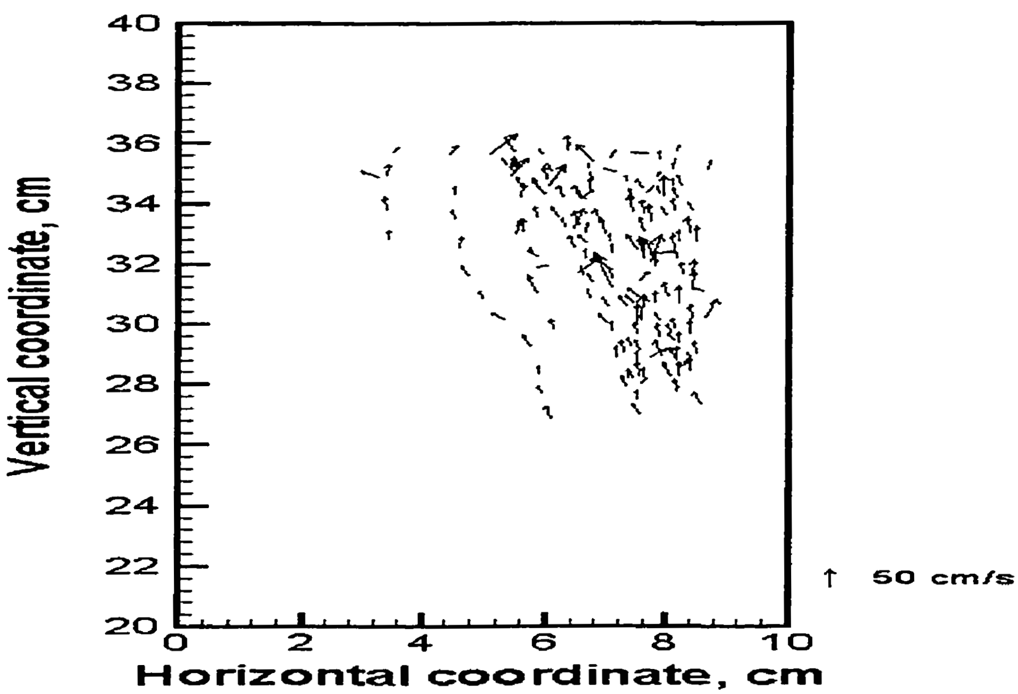

Figure 5.5.4. Bubble velocity vector plot for NPE-air system at U=13.2 cm/s –top section of the bed

It may be noted in Figures 5.5.1 and 5.5.2 that bubbles are not uniformly distributed around the center line of the bed at the bottom section. Instead there are more bubbles in the right-hand-side of the bed in Figure 5.5.1 and in the left-hand-side in Figure 5.5.2. Since the experiments for the two conditions were performed at different times, the images were taken for the opposite direction of the column to the X-ray camera at the two times. However, the asymmetric distribution of the bubbles still implies that at low superficial gas velocities the gas distribution just above the distributor is not symmetric. At U=28.8 cm/s, bubbles are uniformly distributed around the center of the bed, indicating an improved gas distribution across the distributor. The asymmetric distribution of air flow across the distributor is possibly attributable to improper distributor design or/and improper installation of the distributor.

The bubble flow patterns for NPE-air system at the top section of the bed are shown in Figures 5.5.1 to 5.5.2 and 5.5.4 at different superficial gas velocities. As discussed in the previous chapter, the top of the original images in these cases was 2 cm below the averaged bed surface. At the top section bubbles in the bed are considered fully developed. At a superficial gas velocity of 13.2 cm/s, the distribution of the bubbles is still not symmetric around the bed center line as shown in Figure 5.5.4, which indicates the presence of asymmetric gas flow distribution throughout the bed. At superficial gas velocity of 17.6 cm/s and 21.6 cm/s, bubble flow becomes almost symmetric around the bed center line as shown in Figures 5.5.1 and 5.5.2, respectively. Better gas distribution is expected in these cases.

It is also noted from the vector plots that the bubble flow is away from the wall of the column. It is different from those in the WPE-air and NS-air systems that will be discussed shortly. In order to give an idea of bubble flow pattern in the entire fluidized bed, the velocity vectors for the top and bottom section were plotted together as shown in Figures 5.5.1 and 5.5.2 for NPE-air system at superficial gas velocities of 17.6 cm/s and 21.6 cm/s, respectively. Unfortunately, no images were taken in the middle section of the bed and therefore no bubble velocity vectors are shown in this section. It is recommended as a part of future work.

The bubble velocity vector plots for the WPE-air system at top section of the bed are shown in Figures 5.5.5 to 5.5.7. As mentioned in the previous chapter, at the four superficial gas velocities of 10.8 cm/s, 14.4 cm/s 18.0 cm/s and 21.6 cm/s, no bubbles were observed at the bottom section which is close to the distributor. The original images were also taken and recorded at the top section of the bed, which is 2 cm below the averaged bed surface. In the top section of the bed bubbles are considered as fully developed. At superficial gas velocity of 10.8 cm/s, since very few bubbles were observed even at the top section and therefore a vector plot was not made for this condition. As seen in Figure 5.5.5, the bubble flow is fully developed and the bubble distribution is uniform and symmetric around the center line of the column. The similar patterns can be observed in Figures 5.5.6 and 5.5.7.

Comparing Figure 5.5.5 with Figure 5.5.6, one can note that the fluidized bed expands by about 6.0 cm when the superficial gas velocity increases by 3.6 cm/s from 14.4 cm/s to 18.0 cm/s. However, the expansion is only 2.0 cm when the superficial gas velocity increases by 3.6 cm/s from 18.0 cm/s to 21.6 cm/s, as one compares Figure 5.5.6 to Figure 5.5.7. The difference indicates that the bed expansion is not a linear relationship with superficial gas velocity. Quantitative information of voidage can be obtained by CT scanning. Compared with the bubble flow pattern in the NPE-air system, the bubble flow in the WPE-air system is closer to the wall of the column. Hence, the gas-solid mixing in the fully developed flow region for WPE-air system is better than that for NPE-air system.

For the NS-air system, the original images were also taken and recorded at 2 cm above the porous plate distributor for the bottom section of the bed. However, different from NPE-air system, bubbles were observed at 2.0 cm above the distributor as shown in Figures 5.5.8 and 5.5.9, indicating that the formation of bubbles in NS-air system occurs much sooner than that in the NPE-air system. This is understandable since the superficial gas velocity used in NS-air system is much higher than that used in NPE-air system. Therefore, much more coalescence of tiny bubbles occurs just above the distributor to form large bubbles.

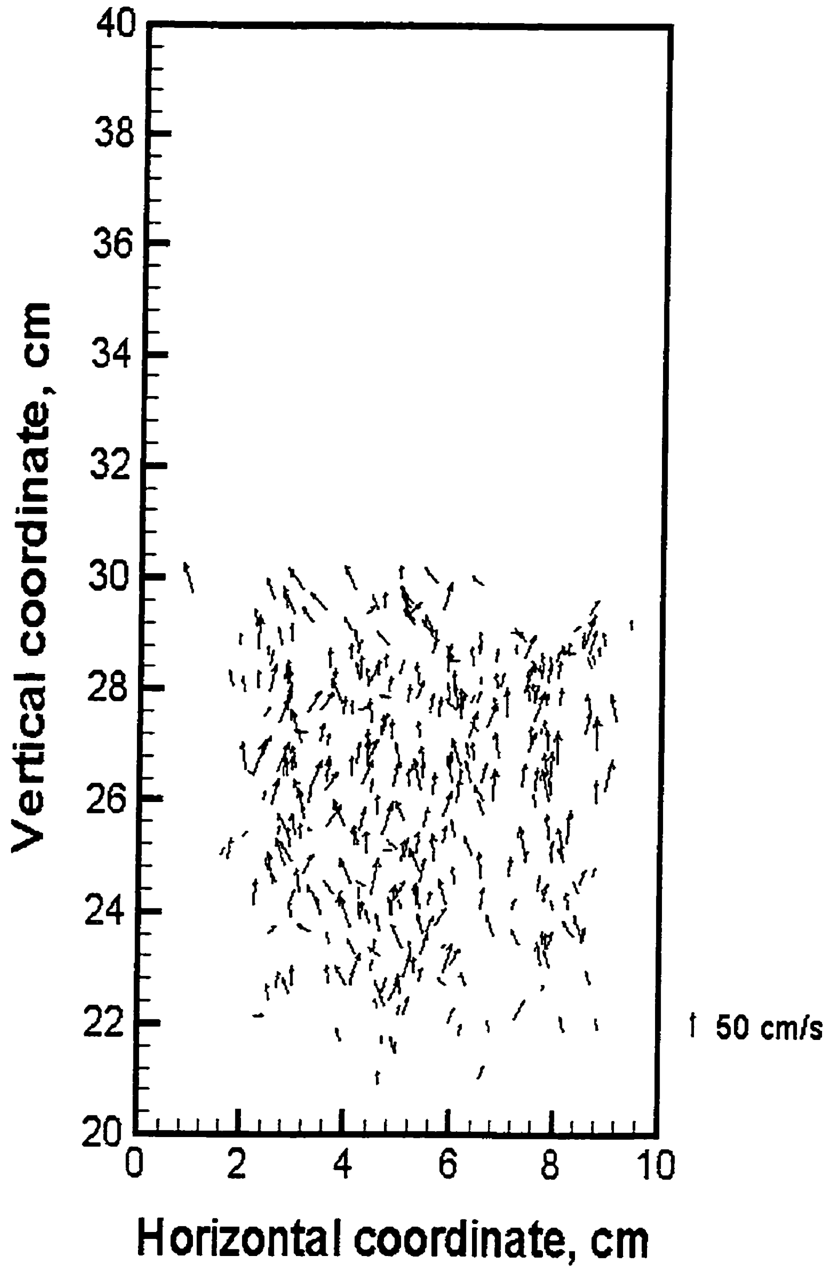

Figure 5.5.5. Bubble velocity vector plot for WPE-air system at U=14.4 cm/s –top section of the bed

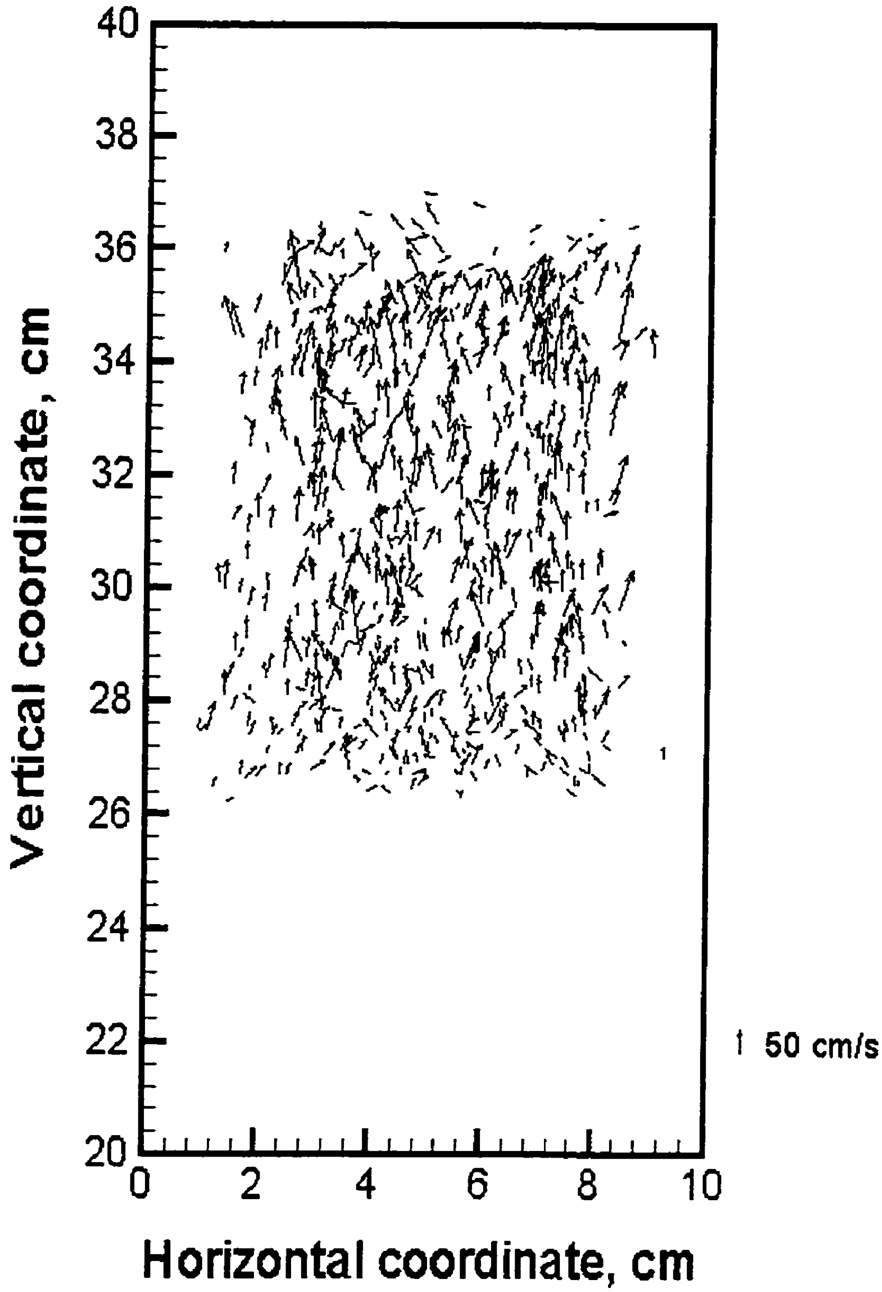

Figure 5.5.6. Bubble velocity vector plot for WPE-air system at U=18.0 cm/s –top section of the bed

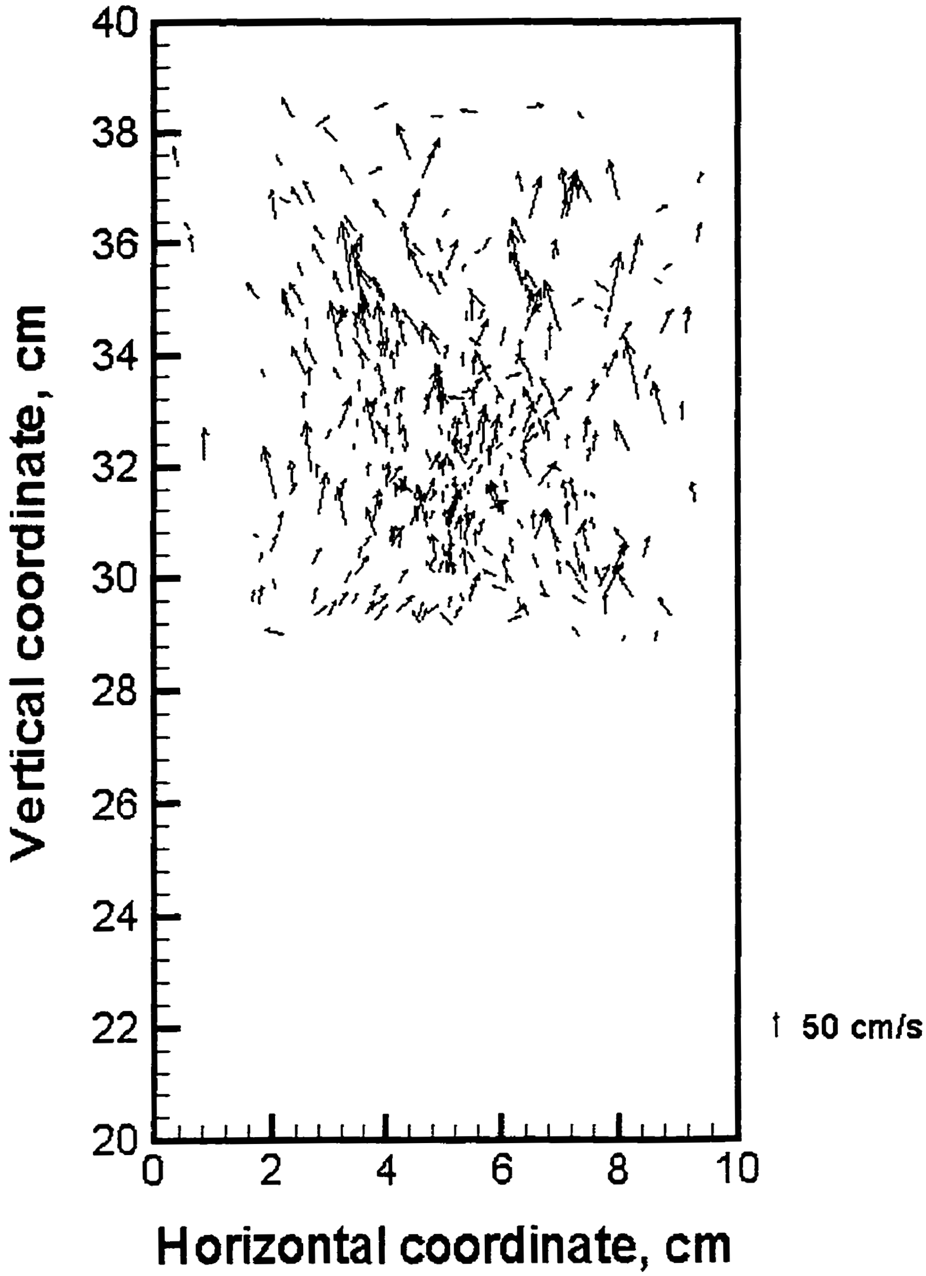

Figure 5.5.7. Bubble velocity vector plot for WPE-air system at U=21.6 cm/s –top section of the bed

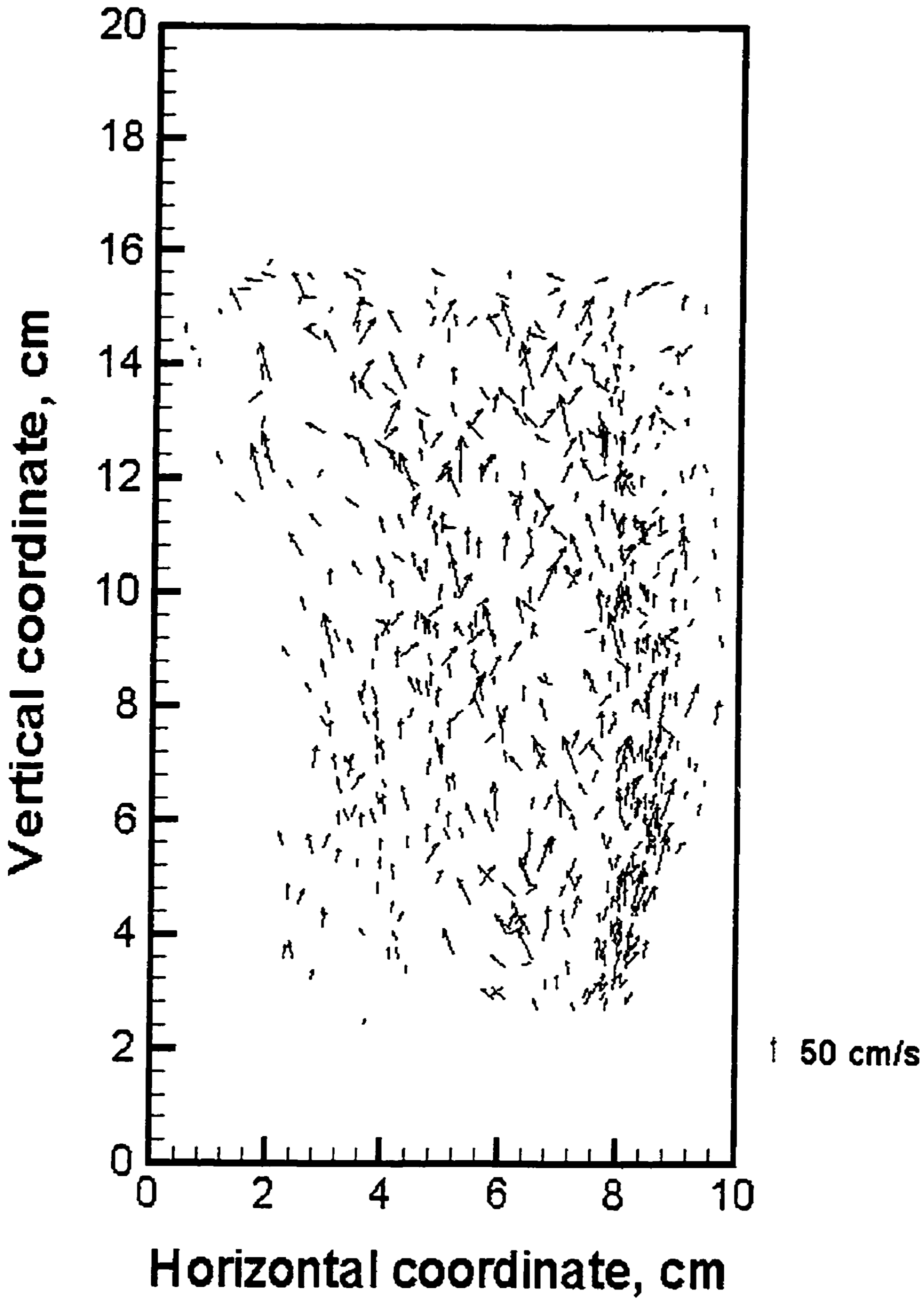

Figure 5.5.8. Bubble velocity vector plot for NS-air system at U=35.2 cm/s –bottom section of the be

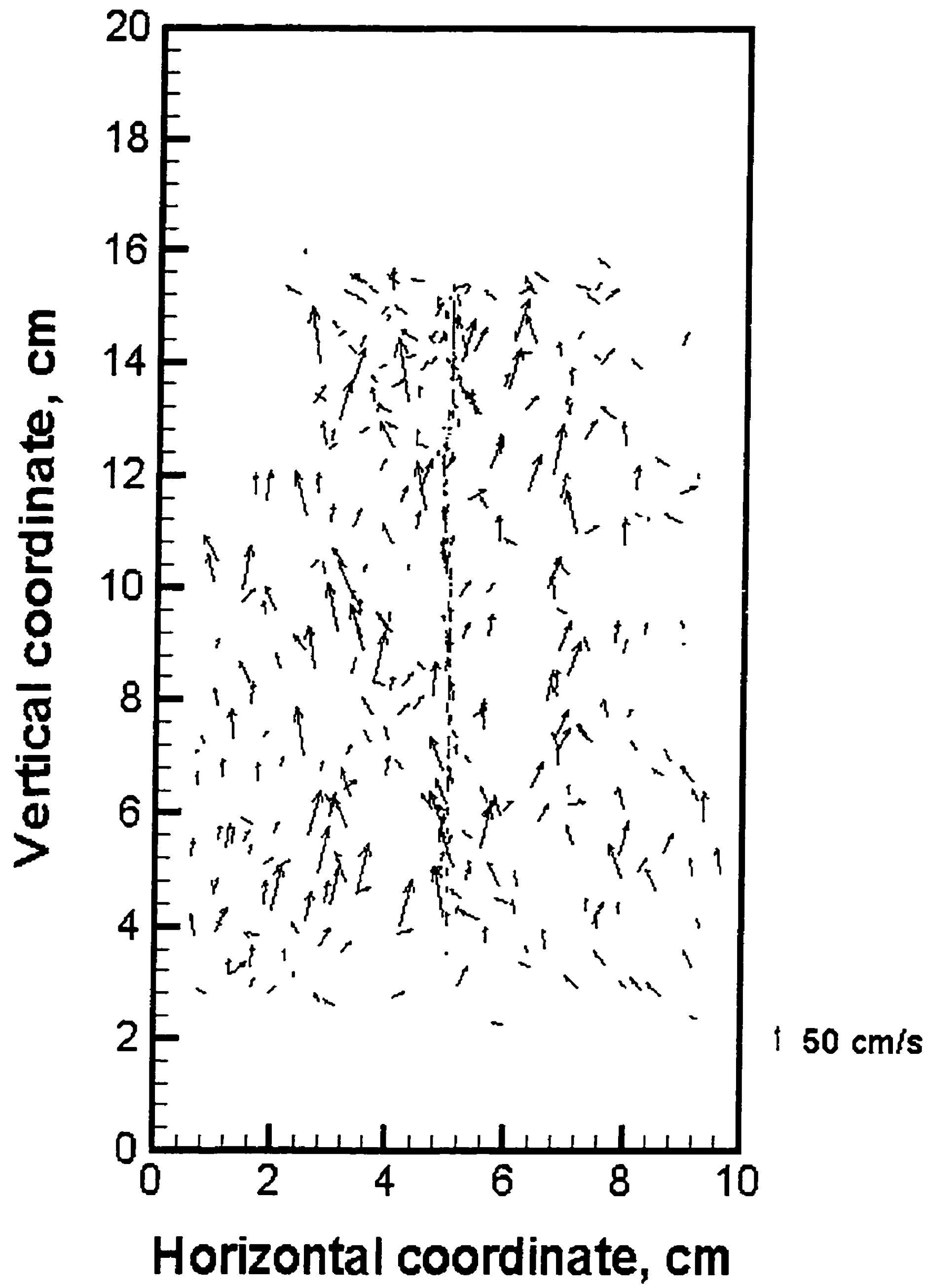

Figure 5.5.9. Bubble velocity vector plot for NS-air system at U=52.8 cm/s –bottom section of the bed

At a superficial gas velocity of 35.2 cm/s ($2.0\times U_{mf}$) bubbles in Figure 5.5.8 are not symmetric around the center line of the column, which means that the air flow above the distributor is not uniform. When the superficial gas velocity is increased to 52.8 cm/s (about $3.0\times U_{mf}$) the bubble flow is much more uniform and symmetric around the center line of the column as shown in Figure 5.5.9. The conclusion is that increased U/U_{mf} can improve the gas phase flow distribution, and thus the mixing in fluidized beds.

It is of interest to note from Figures 5.5.8 and 5.5.9 that the bubble flow is much closer to the wall of the column than the other two systems. This may be attributed to the higher density of the sand particles. More experimental work with a larger diameter column is needed to clarify this interesting phenomenon.

In summary, bubble flow is not uniform and symmetric at low U/U_{mf} due to the distribution of gas flow across the distributor. Increased U/U_{mf} can improve the bubble flow distribution in the beds. The bubble flow in the NPE-air system is mainly around the center line of the bed while it is more uniformly distributed in the whole cross-section of the bed for NS-air system.

CHAPTER 6
CONCLUSIONS

Fluidized bed reactors are the preferred reactors for several processes in the chemical industry. Bubble size, velocity, flow pattern, occurrence frequency and volume fractions are important parameters for modeling and design of fluidized bed reactors. Many experimental techniques and methods have been developed to study these parameters since the widespread introduction of fluidized beds. However, in the previous studies, bubble dynamic properties in 2-D or 3-D fluidized beds were obtained by analyzing very limited number of bubbles due to the fact that data analysis and image processing were mostly performed manually. It is questionable whether the bubble dynamic properties obtained this way are statistically representative. Bubble flow information with good statistics is needed to provide reliable fundamental data in the study of fluidized beds. The focus of the present work is on investigating bubble size, velocity, flow pattern, occurrence frequency and volume fraction in 3-D fluidized beds with NPE-air, WPE-air and NS-air systems to provide statistically representative information on bubble dynamics. To reach these goals, an image processing software package was developed for online image processing to extract bubble dynamic information from the images recorded with an X-ray imaging system. In what follows, the principal accomplishments and findings of this research work are summarized. Following this, recommendations for future work are made.

6.1. Principal Accomplishments and Results

6.1.1. Experimental Work

The particles used in this study include narrow size distribution polyethylene (NPE), wide size distribution polyethylene (WPE) and narrow size distribution sand (NS). They all belong to the Geldart B group. Studies of bubble flow dynamics with polyethylene particles have not been reported in the open literature so far. The experimental set-up consists of a fluidized bed column and an X-ray imaging system. The experiments were carried out in a 10 cm diameter column with a fixed settled bed height of 30 cm (L/D=3).

In order to determine the superficial gas velocities to be used for the imaging experiments, minimum fluidization measurements were conducted for the three gas-solid systems. The minimum fluidization velocity is 8.9 cm/s for the NPE-air system, 7.1 cm/s for the WPE-air system bed and 18.5 cm/s for the NS-air system. X-ray imaging experiments were then performed for the three systems using GE MPX-100 a medical fluoroscopy system at superficial gas velocities ranging from $1.5\times U_{mf}$ to $3.0\times U_{mf}$. The images were recorded on videotapes for image processing.

6.1.2. Image Processing

An image processing software package was developed to process thousands of image frames digitized at a temporal resolution of 30 frames/s from videotapes. This image processing software package can track and mark bubbles from one frame to the next sequentially and automatically. Four steps are needed to conduct the image processing:

- rotating and cropping;
- image enhancement-subtracting image background;
- image segmentation and representation-smoothing, filtering and thresholding;
- bubble marking and tracking.

In total, 12 image data sets were processed. Bubble diameter, bubble vertical and horizontal velocity, bubble occurrence frequency and bubble volume fractions were extracted from the image processing work for the three gas-solid systems at different operating conditions.

6.1.3. Analysis of Results

6.1.3.1. Bubble Size

Analysis of image processing results for bubble size indicates that with an increase in the bed height above distributor and superficial gas velocity bubble diameter increases, which is consistent with what is expected. Comparisons indicate that the bubble diameter for the NPE-air system is close to that for the NS-air system at the same value of U/U_{mf}, while the averaged bubble diameter for the NPE-air system is larger than that for the

WPE-air system at the same value of U/U_{mf}. One possible reason is that the larger particles in the WPE particles favor splitting of large bubbles in the bed. Therefore, it can be concluded that wider particle size distribution would result in smaller bubbles in fluidized beds, which is desired in fluidization operations.

The correlation proposed by Mori and Wen (1975) was used to predict bubble diameters in this study. For the bottom section of the bed, the predicted bubble diameter is slightly higher than the averaged bubble diameter obtained from image processing, while the predicted one is much higher than the one from image processing the top section of the bed. As mentioned in Chapter 5, one reason for this deviation is that Mori and Wen's correlation was based on experimental data obtained in fluidized beds with $L/D<2$. Another reason may be the experimental data that Mori and Wen used to develop the correlation is not statistically representative due to the limited number (10 to 20 for each operating condition) of bubbles counted. In addition, the portion of bubbles at the top and bottom of the frame was not taken into account in the image processing method in this study. This also contributed to that the bubble size from the image processing is smaller than that from the correlation at the top and bottom of the frame. Therefore, the correlation and the image processing method should be modified in future work.

6.1.3.2. Bubble Volume Fraction and Verification of the Imaging Method

Bubble volume fraction is defined as the ratio of the total bubble geometric volume in one frame to the fluidized bed volume. With an increase in the bed height above the distributor bubble volume fraction increases. Comparisons indicate that at same U/U_{mf} bubble volume fraction for the NPE-air system is higher than that for the WPE-air system, while the bubble volume fraction for the NS-air system is slightly higher than that for the NPE-air system.

The images processed in this work are two-dimensional while the fluidized bed is three-dimensional. In the current image processing work it was assumed that bubble overlapping is negligible. In order to validate the present image processing method, bubble volume in the fluidized bed was calculated by two methods. One is by bubble volume fraction data obtained from the image processing while the other one is by fluidized bed expansion. The data for the NPE-air system at superficial gas velocities of 17.6 cm/s and 21.6 cm/s were chosen for the verification. The bubble volume fraction obtained from image processing is 37-39% less than that obtained from bed expansion with decreased emulsion density not taken into account. According to Kunii and Levenspiel (1991), about 25% of gas for Geldart B particles in L/D >2 fluidized beds goes to emulsion phase. Therefore, the deviation would be reduced to 12-14%.

6.1.3.3. Bubble Occurrence Frequency

Bubble occurrence frequency is defined as the total number of new bubbles counted for all the frames in one data set divided by the time period during which the frames are counted. At low superficial gas velocity, bubble occurrence frequency at the bottom section is higher than that at the top section since more small bubbles are formed at the bottom of the bed. Some of them then coalesce into large bubbles while they are rising. At high superficial gas velocity, bubble occurrence frequencies becomes close to each other between top and bottom section due to the fact more large bubbles break up into small bubbles. With an increase in U/U_{mf} or superficial gas velocity, bubble occurrence frequency increases for both NPE-air and WPE-air systems. Moreover, bubble occurrence frequency for the WPE-air system is higher than that for the NPE-air system. The wide particle size distribution causes more bubble break-up than the narrow particle size distribution. The trends of the increase in bubble occurrence frequency with U/U_{mf} or superficial gas velocities are similar for NPE-air and NS-air systems at the bottom section of the fluidized bed, where bubble flow is not fully developed and there is not much coalescence and break-up.

6.1.3.4. Bubble Velocity and Flow Patterns

Bubble rising velocity increases slightly with increasing superficial gas velocity and fluidized bed height for all the three systems. The time averaged bubble vertical velocity increases when the value of U/U_{mf} increases for the NPE-air system, while it increases slightly for the WPE-air system and remains almost constant for the NS-air system. Due to the limited number of points more experimental data are needed before such a general conclusion is reached. As mentioned before, in the present image processing work, not only bubble vertical velocity but also bubble horizontal velocity were obtained at different positions of the two dimensional image frame. Then, bubble velocity vector plots could be generated to describe the bubble flow patterns in the bed for each image data set investigated in this work. Such bubble flow pattern plots have not been found in the open literature. It is observed that the NPE–air system and the WPE-air system have similar bubble flow patterns, different from NS-air system. The bubble flow in the NPE-air system is not close to the wall of the bed while it is more uniformly distributed across the whole cross-section of the bed for the NS-air system. In addition, for the NPE-air system bubbles do not appear in the region close to distributor while there are bubbles observed in this region for NS-air system. It is also found that the bubble flow is not uniform and symmetric at low U/U_{mf} due to the mal-distribution of gas flow across the distributor. Increased U/U_{mf} can improve the bubble flow and thus the gas phase mixing in the beds.

The correlation proposed by Kunii and Levenspiel (1991) was used to predict bubble rising velocity in fluidized beds in this study. To calculate bubble rising velocity as a function of the height above the distributor, bubble diameter values at the corresponding axial position were evaluated in two ways. One is to predict these values by Mori and Wen's correlation, and the other is to use the bubble diameter values obtained from the current image processing work. By using the bubble diameters predicted from the correlation, the predicted bubble rising velocities are higher than those obtained from image processing. By using the bubble diameters obtained from image processing of this work, the predicted values of bubble rising velocities are very close to those obtained from image processing. This indicates that once the bubble diameter values are properly estimated or measured from experiments, Kunii and Levenspiel's correlation can provide good prediction of bubble rising velocities for Geldart B particles.

6.2. Recommendations for Future Work

The X-ray imaging system used is a medical fluoroscopy system (GE MPX-100). The major drawback of this system is the limitation of image size. In addition, it was observed from the blank experiment images using the specific system in the lab that the background of the digital image does not have a uniform intensity distribution. The top part is brighter and the bottom part is darker. This may be caused by the non-uniform distribution of the incident X-ray radiation or the non-uniform response of the image intensifier which converts the X-ray radiation to a light image. Modification of the image intensifier in the X-ray fluoroscopy system may remove the artifacts and make the machine more useful for taking large images. From the bubble velocity vector plots, an asymmetric distribution of air flowing above the distributor was observed. It is possibly attributed to improper distributor design or/and improper installation of the distributor, which needs to be verified. For study of sand-air system, another distributor that can make the pressure drop cross the distributor high enough, should be provided in future work.

With the current X-ray imaging system, the images were not taken at the middle section of the fluidized beds. A specific study for this section is recommended for future work. The computer programs developed in this study for image processing do not take into account the half bubbles at the top and bottom of the images. Estimation of an equivalent diameter for the half bubbles should be made. The bubble tracking and marking program can only track bubbles in about 95% of the frames in an image set, for which modifications also need to be made. More experiments need to be done to verify the conclusions for the three gas-solid systems. Mori and Wen's correlation was used for predicting bubble diameter. However, the comparison indicates that the predicted bubble diameter is higher than that from image processing at bottom section and much higher for the top section of the bed. Modification for this correlation should be done using good statistical bubble information from two to three image sets at the same operating condition. Verification of the present imaging method was made with an estimation of emulsion phase voidage. More accurate verification based on experimentally measured emulsion phase voidage or density data should be conducted.

REFERENCES

Banholzer, W. F., C. L. Spiro, P. G. Kosky and D. H. Maylotte, "Direct Imaging of Time-Averaged Flow Patterns in a Fluidized Reactor Using X-ray Computed Tomography", *Ind. Engng. Chem. Res.*, **26**, 763-781, 1987.

Baumgarten, P. K., and R. L. Pigford, "Density Fluctuations in Fluidized Beds", *AIChE J.*, **6**, 115-123, 1960.

Bloore, P. O. and J. S. M. Botterill, "Similarity in Behavior between Gas Bubbles in Liquid and Fluidized Solid Systems", *Nature*, **190**, 250-251, 1961.

Bradley, J, "XV", Philadelphia, USA, Copyright © 1998.

Chen, J., F. Li, S. Degaleesan, P. Gupta, M. H. Al-Dahhan, M. P. Dudukovic', and B. A. Toseland, "Fluid Dynamic Parameters in Bubble Columns with Internals", *Chem. Eng. Sci.*, **54**, 2187-2197, 1999.

Choi, J. H., J. E. Son, and S. D. Kim, "Bubble size and Frequency in Fluidized Beds", *J. Chem. Eng. Japan.* **21**, 171-178, 1988.

Choi, J. H., J E. Son and S. D. Kim, "Generalized Model for Bubble Size and Frequency in Gas Fluidized Beds", *Ind. Eng. Chem. Res.*, **37**, 2559-2564, 1998.

Clift, R., and J. R. Grace, "Coalescence of Bubbles in Fluidized Beds," *AIChE Symp. Ser.*, **67**, 23 (1971).

Clough, D. E. and A. W. Weimer, "Time-Dependent Behavior of Bubble Volume in Fluidized Beds", *Ind. Engng. Chem. Fundam.*, **24**, 235-241, 1985.

Darton, R. C.; R. D. La Nauze, J. F. Davidson, and D. Harrison, "Bubble Growth due to Coalescence in Fluidized Beds" *Trans. Inst. Chem. Engrs.* **55**, 274-280, 1977.

Davidson, J. F. "Discussion Following Symposium on Fluidization", *Trans. Instn. Chem. Engrs.*, **39**, 230-232, 1961.

Davidson, J. F. and D. Harrison, *Fluidized Particles*, Cambridge University Press, New York, 1963.

Fan, L. T. T. C. Ho, S. Hiraoka and W. P. Walawender, "Pressure Fluctuations in a Fluidized Bed", *AIChE J.*, **27**, 388-396, 1981.

Fan, L. T., T. C. Ho, and W. P. Walawender, "Measurements of the Rise Velocities of Bubbles, Slugs and Pressure Waves in a Gas-Solid Fluidized Bed Using Pressure Fluctuation Signals", *AIChE J.*, **29**, 33-39, 1983.

Gamblin, B., D. Newton, and C. Grant, "X-ray Characterization of the Gas Flow Patterns from FCC regenerator air ring nozzles", 4th International Conference on Circulatinf Fluidized Beds, PA, August 1-5, 595, 1993.

Geldart, D. "The Size and Frequency of Bubbles in Two-and Three Dimentional Gas Fluidized Beds " *Powder Technology*, **4**, 41-55, 1970/1971.

Geldart, D. and J. R. Kelsey, " The Use of Capacitance Probes in Gas Fluidized Beds", *Powder Technology*, **6**, 45-60, 1972.

Geldart, D., "Types of Gas Fluidization", *Powder Technology*, 7, 285-292, 1973.

Gibilaro, L. G., R. Di Felice, P. U. Foscolo,and S. P. Waldram, "Fluidization Quality: a Criterion for Indeterminate Stability", *Chem. Engng. J.*, **37**, 25-33, 1988

Gonzalez, C. Rafael and P. Wintz, "Digital Image Processing", Addison-Wesley Publishing Company, 1977.

Gonzalez, C. Rafael and R. E. Woods, "Digital Image Processing", Addison-Wesley Publishing Company, 1992.

Grohse, E. W., "Analysis of Gas-Fluidized Solids by X-ray Absorption", *AIChE J.*, **1**, 358, 1955.

Gunn, D. J. and H. H. Al-Doori, "The Measurement of Bubble Flows in Fluidized Beds by Electrical Probe", *Int. J. Multiphase Flow*, **11**, 535-551, 1985.

Hailu, L., F. Plaka, R. Clift, and J. F. Davidson, "Measurement of Gas Flow Through a Two-Dimensional Bubble in a Fluidized Bed", *Trans. Instn. Chem. Engrs.*, **71**, 382-389, 1993.

Halow, J. S., G. E. Fasching, and P. Nicoletti, "Preliminary Capacitance Imaging Experiments of a Fluidized Bed", *AIChE Symp. Ser.*, **86**, 41-50, 1990.

Halow, J. S. and P. Nicoletti, "Observations of Fluidized Bed Coalescence Imaging", *Powder Technology*, **69**, 255-277, 1992.

Halow, J. S., G. E. Fasching, P. Nicoletti, and J. L. Spennik, "Observation of a Fluidized bed Using Capacitance Imaging", *Chem. Engng. Sci.*, **48**, 643-659, 1993.

Halow, J. S., "Electrical Capacitance Imaging of Fluidized beds", *Non-Invasive Monitoring of Multiphase Flows*, Chaouki, J., Larachi, F., and Dudukovic, M. P., Eds. Elsevier: Amsterdam, The Netherlands, Chapter 9, 263-274., 1997.

Horio, M. and A. Nonaka, "A Generalized Bubble Diameter Correlation for Gas-Solid Fluidized Beds", *AIChE J.*, **33**, 1865-1872, 1987.

Jackson, R., "The Mechanics of Fluidized Beds, part 1", *Trans. Instn. Chem. Engrs.*, **41**, 13-21, 1963a.

Jackson, R., "The Mechanics of Fluidized Beds, part 2", *Trans. Instn. Chem. Engrs.*, **41**, 22-48, 1963b.

Kantzas, A., "Computation of Holdups in Fluidized and Trickle Beds by Computer-Assisted Tomography", *AIChE J.*, **40** (7), 1254-1261, 1994.

Kantzas, A. and N. Kalogerakis, "Monitoring the Fluidization Characteristics of Polyolefin Resins Using X-ray Computer Assisted Tomography Scanning", *Chem. Engng. Sci.*, **51**, 1979-1990, 1996.

Kantzas, A.,I. Wright, and N. Kalogerakis, "Quantification of Channeling in Polyethylene Resin Fluid Beds Using X-ray Computer Assisted Tomography (CAT)", *Chem. Engng. Sci.*, **52**, 2023-2035, 1997.

Kantzas, A., I. Wright, A. Bhargava, F. Li, and K. Hamilton, "Measurement of Hydrodynamic Data of Gas Phase Polymerization Reactors Using Non-Intrusive Methods", accepted for publication in *Catalysis today*, 2000.

Kunii, D. and O. Levenspiel, "Fluidization Engineering", Butterworths, Boston, MA, 1991.

Lanneau, K. P., " Gas-Solids Contacting in Fluidized Beds", *Trans. Instu Chem. Engrs*, **38**, 125-143, 1960.

Li, F., I. Wright, K. Hamilton, C. Hyndman, and A. Kantzas, "X-ray Imaging of Bubble in Fluidized Beds" presented at the 49th Canadian Chemical Engineering Conference, Saskatoon, Saskacthewan, 3-6 Oct., 1999.

Littman, H. and G. A. Homolka, "Bubble Rise Velocities in Two-Dimensional Gas Fluidized Beds from Pressure Measurements", *Chem. Engng. Prog. Symp. Ser.*, **66**, 37-46, 1970.

Lirag, R. and H. Littman, "Statistical Study of Pressure Fluctuation in a Fluidized Bed", *AIChE. Synp. Ser.*, **67**, 11-22, 1971.

Luevisutthichat, W., A. Tsutsumi, and K. Yoshida, "Bubble Characteristics in Multi-Phase Flow Systems: Bubble Size and Size Distribution", *J. Chem. Eng. of Japan*, **30**, 461-466, 1997.

Morse, R. D. and C. O. Ballou, "The Uniformity of Fluidization, Its Measurement and Use", *Chem. Engng Prog.* **47**, 199-211, 1951.

Mori, S and C. Y. Wen, "Estimation of Bubble Diameter in Gaseous Fluidized Beds" *AIChE J.* **21**, 109-115, 1975.

Mudde, R. F., H. B. M. Schulte, H. E. A. Van den Akker, "Analysis of a Bubbling 2-D Gas-Fluidized Bed Using Image Processing", *Powder Technology*, **81**, 149-159, 1994.

Murray, J. D., "On the Mechanics of Fluidization, Part 1", *Fluid Mech.*, **21**, 465-493, 1965a.

Murray, J. D., "On the Mechanics of Fluidization, Part 2", *Fluid Mech.*, **22**, 57-53, 1965b.

Musmarra, D., S. Vaccaro, M. Filla, and L. Massimilla, "Propagation Characteristics of Pressure Disturbance by Gas Jets in Fluidized Beds", *Int. J. Multiphase Flow*, **18**, 965-976, 1992

Okhi, K. and T. Shirai, "Particle Velocity in a Fluidized Bed", in *Fluidization Technology* (Edited by Keairns, D. L.), 95-119, Hemisphere, New York, 1976.

Orcutt, J. C. and B. H. Carpenter, "Bubble Coalescences and the Simulation of Mass Transport and Chemical Reaction in Gas Fluidized Beds", *Chem. Engng. Sci.*, **26**, 1049-1064, 1971.

Ormiston, R. M., F. R. G. Mitchell, J. F. Davidson, "The Velocities of Slugs in Fluidized Beds", *Trans. Instn. Chem. Engrs.*, **43**, 209-216, 1965.

Put, M., A. Francesconi, and W. Goosens, "Determination of the Bubble Size Distribution in Gas-Solid Fluidized Beds", in *Proc. Int. Conf. On Fluidization and Its Applications*, Toulouse, France, 223-229, 1973.

Romero, J. B. and D. W. Smith, "Flash X-ray Analysis of Fluidized Beds", *AIChE J.*, **11**, 595-600, 1965.

Rowe, P. N., "Experimental Properties of Bubbles", in *Fluidization*, Chapter 4 (Edited by Davidson, J. F. and Harrison, D.). Academic Press, London, 1971.

Rowe, P. N. and D. J. Everett, "Fluidized Bed Bubbles Viewed by X-rays", *Trans. Inst. Chem. Eng.*, **50**, 42-60, 1972a, b, c.

Rowe, P. N. and B. A. Partridge, "An X-ray Study of Bubbles in Fluidized Beds", *Trans. Instn. Chem. Engrs.*, **43**, 157-165, 1965.

Rowe, P. N. and C. Yocono, "The Bubbling Behaviors of Fine Powders When Fluidized", *Chem. Engng. Sci.*, **31**, 1179-1192, 1976.

Rowe, P. N., "Prediction of Bubble Size in a Gas Fluidized Bed", *Chem. Eng. Sci.*, **31**, 285-288, 1976.

Rowe, P. N. and H. Masson, "Interaction of Bubbles with Probes in Gas Fluidized Beds", *Trans. Inst. Chem. Engrs*, **59**, 177-185, 1981.

Rowe, P. N. And B. A. Partridge, "An X-Ray Study of Bubble in Fluidized Beds", *Institution of Chemical Engineers*, **75**, s116-s134, 1997.

Rose, P. N., L. Santoro, and J. G. Yates, "The Division of Gas Between Bubble and Interstitial Phase in Fluidized Beds of Fine Powders", *Chem. Engng. Sci.*, **33**, 133, 1978.

Roy, R., J. F. Davidson, and V. G. Tuponogov, "The Velocity of Sound in Fluidized Beds", *Chem. Engng. Sci.,* **45**, 3233-3245, 1990.

Seville, J. P. K., J. P. E. Morgan, and R. Clift, "Tomographic Determination of the Voidage Structure of Gas Fluidized Beds", *Trans. Instn. Chem. Engrs.*, **43**, T271-296, 1986.

Silver, D., and X. Wang, "Processing of Visualization", IEEE Computer Society, October 27-November 1, San Francisco, CA, 1996.

Simons, S. J. R. and R. A. Williams, "Particle Size Measurement Using Non-Invasive Dielectric Sensors", *Powder Technology.*, **73**, 85-90, 1992.

Simons, S. J. R., J. P. K. Seville, R. Clift, W. B. Gilboy, and M. E. Hosseini-Ashrafi, "Application of Gamma-ray Tomography to Gas Fluidized Beds, in Tomographic Techniques for Process Design and Operation." Chapter 3.1, (Edited by M. S. Beck, E. Campogrande, M. Morris, R. A. Williams and R. C. Waterfall), Computational Methanics Publications, Southampton, 1993.

Taylor, P. A., M. H. Lorenz, and M. R. Sweet, "Spectral Analysis of Pressure Noise in a Fluidized Bed", In *Proc. Int. Conf., on Fluidization and its Application*, Soc. De Cheme Industrielle, Toulouse, 90-98, 1973.

Toei, R., R. M. Matsuno, and K. Yamamoto, "Deformation and Splittings of a Bubble in a Two Dimensional Fluidized Bed: Experimental Results," *J. Chem. Eng. Japan*, **7**, 447 (1974a).

Toomey, R. D. and H. F. Johnstone, "Gaseous Fluidization of Solid Particles", *Chem. Engng. Prog.*, **48**, 220-236, 1952.

Weimer, A. W., D. C. Gyure, and D. E. Clough, "Application of a Gamma-Radiation Density Gauge for Determining Hydrodynamic Properties of Fluidized Beds", *Powder Technology*, **44**, 179-194, 1985.

Weinstein, H., H. J. Feindt, L. Chen and R. A. Graff, " The Measurement of Turbulence Quantities in a High Velocity Fluidized bed", In *Fluidization* (Edited by Potter, O. E. and Nicklin, D. J.) 305-302, Engineering foundation, New York, 1992.

Werther, J. and O. Molerus, "The Local Structure of Gas Fluidized Beds 1. A Statistically Based Measuring System" *Int. J. Multiphase Flow*, **1**, 103-122, 1973a.

Werther, J. and O. Molerus, "The Local Structure of Gas Fluidized Beds 2. The Spatial Distribution of Bubbles" *Int. J. Multiphase Flow,* **1**, 123-138, 1973b.

Werther, J., J. F. Davidson, D. L. Keairns, "Influence of the Distributor Design on Bubble Characteristics in Large Diameter Gas Fluidized Beds" In Fluidization, Eds.; Cambridge University press, London and New York, 7-12, 1978.

Whitehead, A. B. and A. D. Young, "Fluidization in Large Scale Equipment", *in Proc. Int. Symp. on Fluidization*, 294-302, Netherlands University Press, Amsterdam, 1967.

Winter, O., "Density and Pressure Fluctuation in Gas Fluidized Beds" *AIChE J.*, **14**, 426-434, 1968.

Wright, I., "Determination of Fluidization Properties of Polyethylene Resins", Thesis of Master of Engineering, University of Calgary, 1999.

Yasui, G. and L. N. Johanson, "Characteristics of Gas Pockets in Fluidized Beds", *AIChE J.*, **4**, 445-452, 1958.

Yates, J. G. and D. J. Cheesman, "Voidage Variations in the Regions Surrounding a Rising Bubble in a Fluidized Bed", *AIChE Symp. Ser.*, **88**, 34-39, 1992.

Yates, J. G., D. J. Cheesman, and Y. A. Sergeev, "Experimental Observations of Voidage Distribution around Bubbles in a Fluidized Beds", *Chem. Engng. Sci.*, **49**, 1885-1895, 1994.

Yate, J. G., "Experimental Observations of Voidage in Gas Fluidized Beds", in *Non-Invasive Monitoring of Multiphase Flows*, Chaouki, J., Larachi, F., and Dudukovic, M. P., Eds., Elsevier: Amsterdam, The Netherlands, Chapter 4, 141, 1997.

Yoshida, K., K. Nakajima, N. Hamataui, and F. Shimizu, "Size Distribution of Bubbles in Gas Fluidized Beds", in *Fluidization* (Edited by Davidson, J. F. and Brereton, D. L.), 13-18, Cambridge University Press, U. K., 1978.

APPENDIX A

Table A.1. X-ray imaging experiments

Solids	Superficial Gas Velocities Cm/s	Number Of Frames	Number of bubbles	Fluidized bed height (cm)
NS-bottom	U=35.2 $\cong 2.0\times U_{mf}$	328	805	
NS-bottom	U=52.8 $\cong 3.0\times U_{mf}$	312	551	
NS-top	U=35.2 $\cong 2.0\times U_{mf}$	Slugging		
NS-top	U=52.8 $\cong 3.0\times U_{mf}$	Slugging		
NPE-bottom	U=17.6 $\cong 1.5.0\times U_{mf}$	No bubbles		
NPE-bottom	U=17.6 $\cong 2.0\times U_{mf}$	517	500	41
NPE-bottom	U=21.6 $\cong 2.5\times U_{mf}$	339	570	45
NPE-bottom	U=28.8 $\cong 3.0\times U_{mf}$	339	550	47
NPE-top	U=13.2 $\cong 1.5\times U_{mf}$	457	244	39
NPE-top	U=17.6 $\cong 2.0\times U_{mf}$	553	513	41
NPE-top	U=21.6 $\cong 2.5\times U_{mf}$	293	647	45
NPE-top	U=21.6 $\cong 3.0\times U_{mf}$	Slugging		
WPE-bottom	U=10.8 $\cong 1.5\times U_{mf}$	No bubbles		32
WPE-bottom	U=14.4 $\cong 2.0\times U_{mf}$	No bubbles		33
WPE-bottom	U=18.0 $\cong 2.5\times U_{mf}$	No bubbles		40
WPE-bottom	U=18.0 $\cong 3.0\times U_{mf}$	No bubbles		42
WPE-top	U=10.8 $\cong 1.5\times U_{mf}$	493	4	32
WPE-top	U=14.4 $\cong 2.0\times U_{mf}$	561	449	33
WPE-top	U=18.0 $\cong 2.5\times U_{mf}$	667	841	40
WPE-top	U=18.0 $\cong 3.0\times U_{mf}$	572	541	42

APPENDIX B

Bubble size is one of the important image processing results in this study. As discussed in Chapter 4, the number of pixels was counted for each bubble in image frames at a speed of 30 frames/s by using the software developed in this work. The number of pixels was then converted to bubble diameter by assuming that the bubbles are spherical. The original image processing results of bubble size are shown in Figures B.1 (NPE bottom section), B.2 (NPE top section), B.3 (WPE top section) and B.4 (NS bottom section) as scattered points. It should be noted that in these figures there are solid lines crossing the graphs. These solid lines are the results of bubble size predicted with the correlation proposed by Mori and Wen (1975) which is discussed in section 5.1.2.

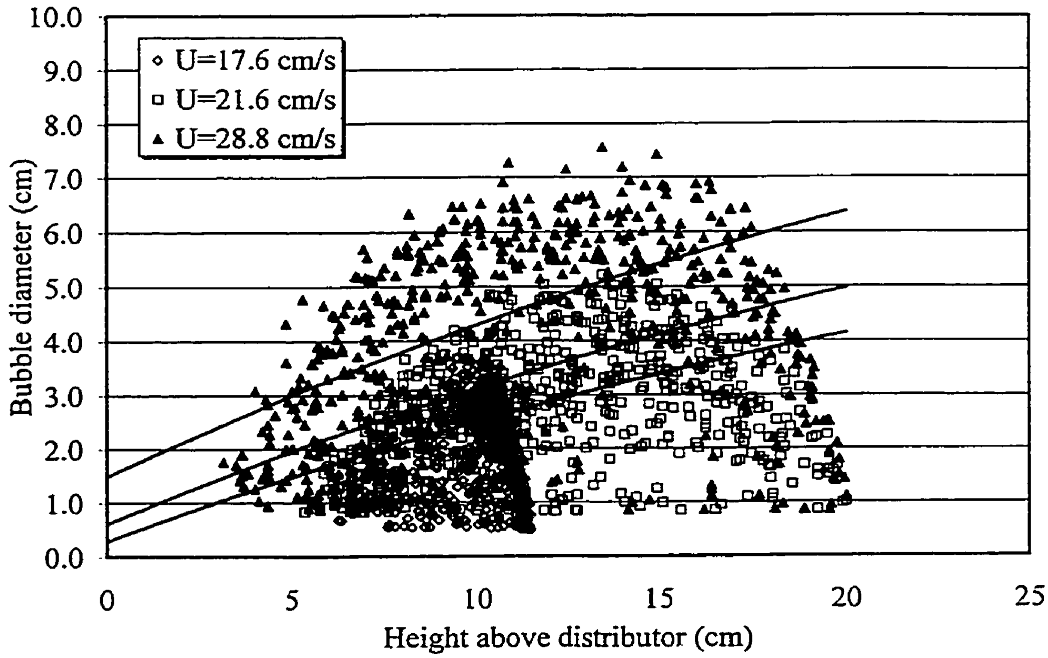

Figure B.1. Image processing results of bubble size for NPE-air system at three different superficial gas velocities-bottom section of the bed

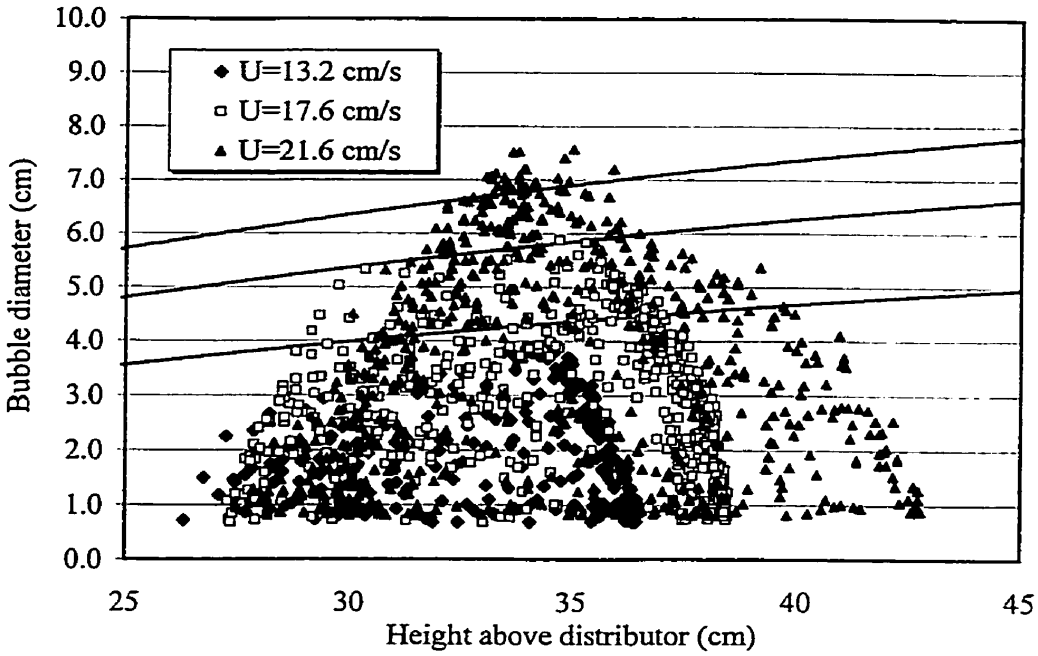

Figure B.2. Image processing results of bubble size for NPE-air system at three different superficial gas velocities-top section of the bed

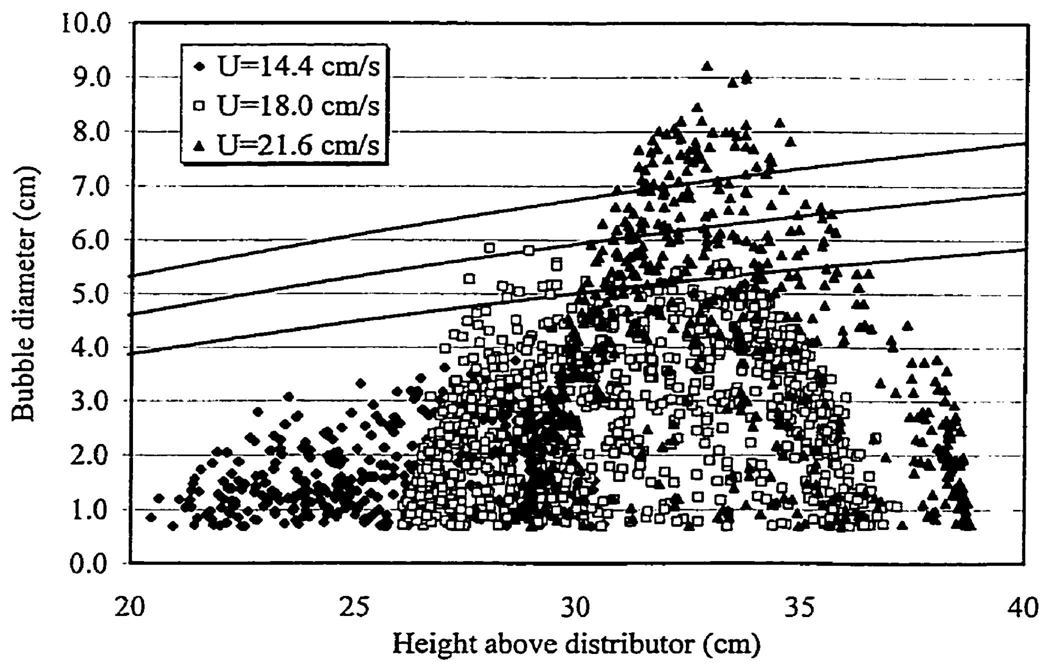

Figure B.3. Image processing results of bubble size for WPE-air system at three different superficial gas velocities-top section of the bed

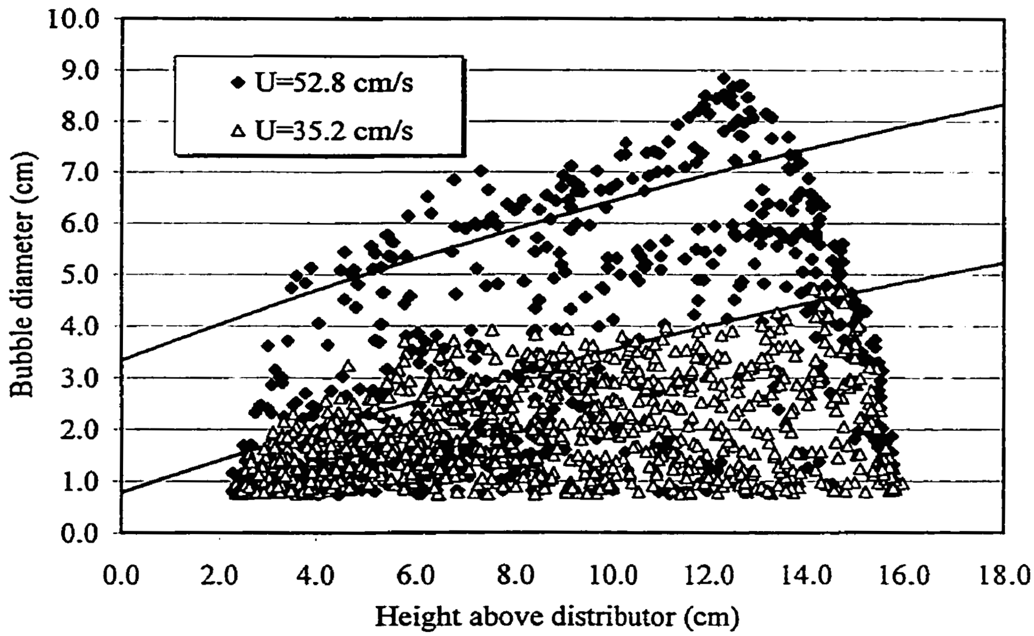

Figure B.4. Image processing results of bubble size for NS-air system at two different superficial gas velocities-bottom section of the bed

APPENDIX C

1. Original Results of Bubble Volume Fraction

Bubble volume fraction is another parameter obtained using the image processing software developed in this study. As mentioned in Chapter 4, the bubble volume fraction is defined as the ratio of the total bubble geometric volume to the fluidized bed volume. Individual values of bubble volume fraction were obtained for each frame during the image processing. The original results from the image processing are shown in Figures C.1 to C.4.

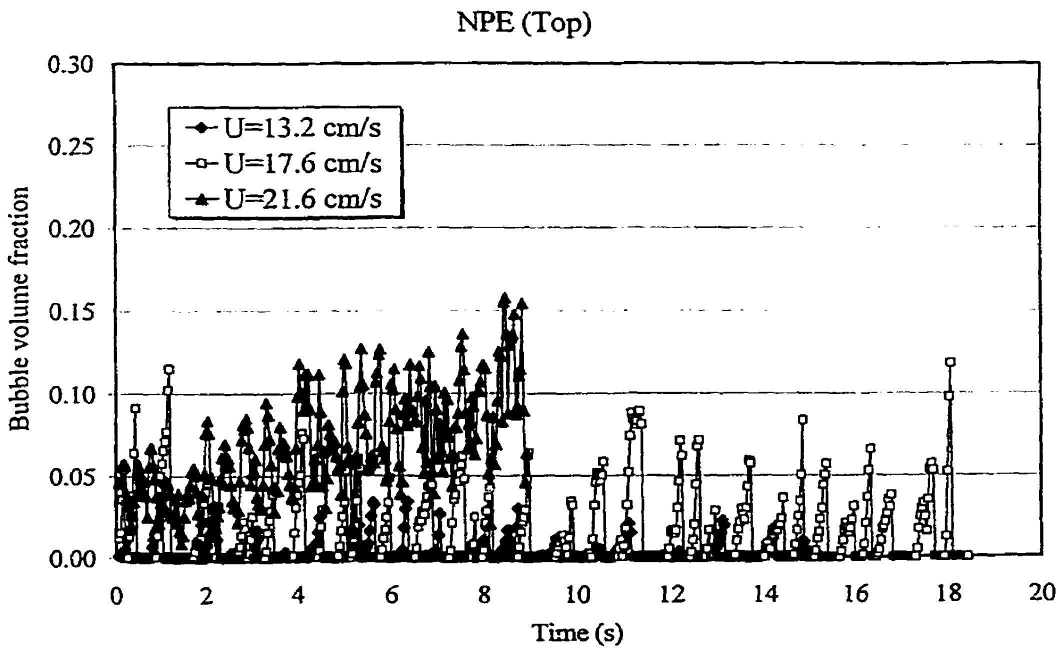

Figure C.1. Original results from image processing for bubble volume fraction for NPE-air system at three superficial gas velocities –top section of the be

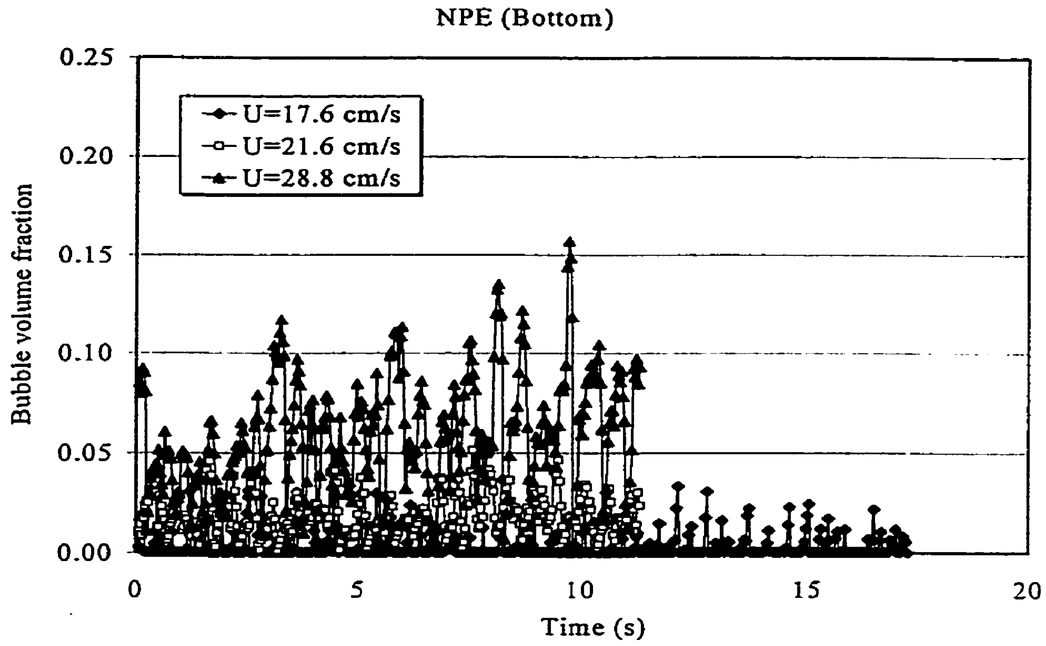

Figure C.2. Original results from image processing for bubble volume fraction for NPE-air system at three superficial gas velocities –bottom section of the bed

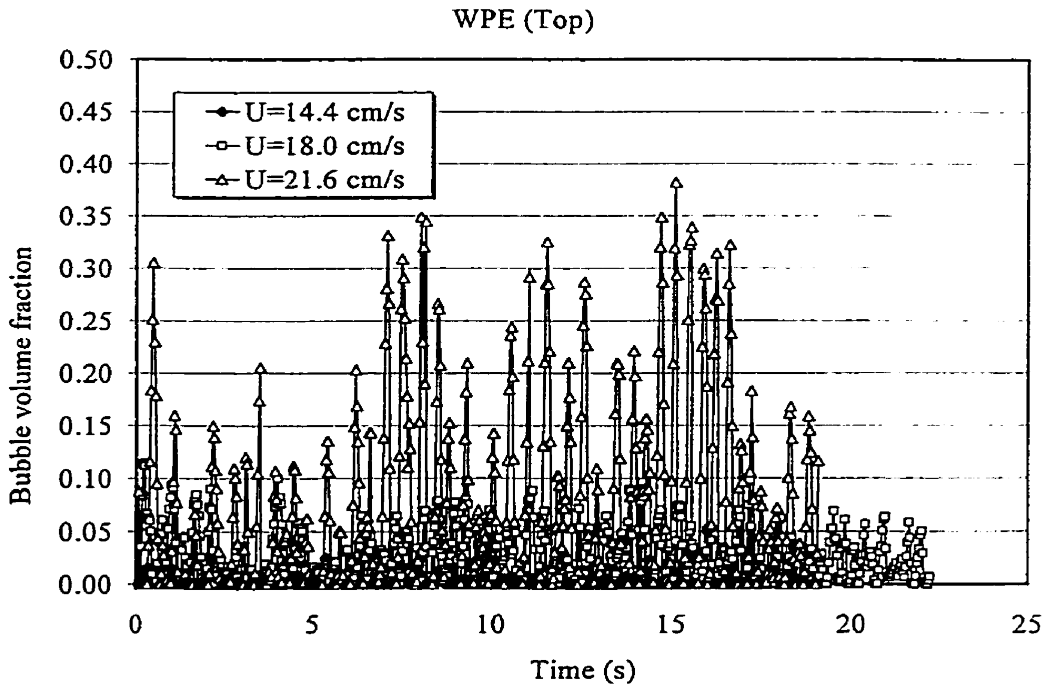

Figure C.3. Original results from image processing for bubble volume fraction for WPE-air system at three superficial gas velocities –top section of the bed

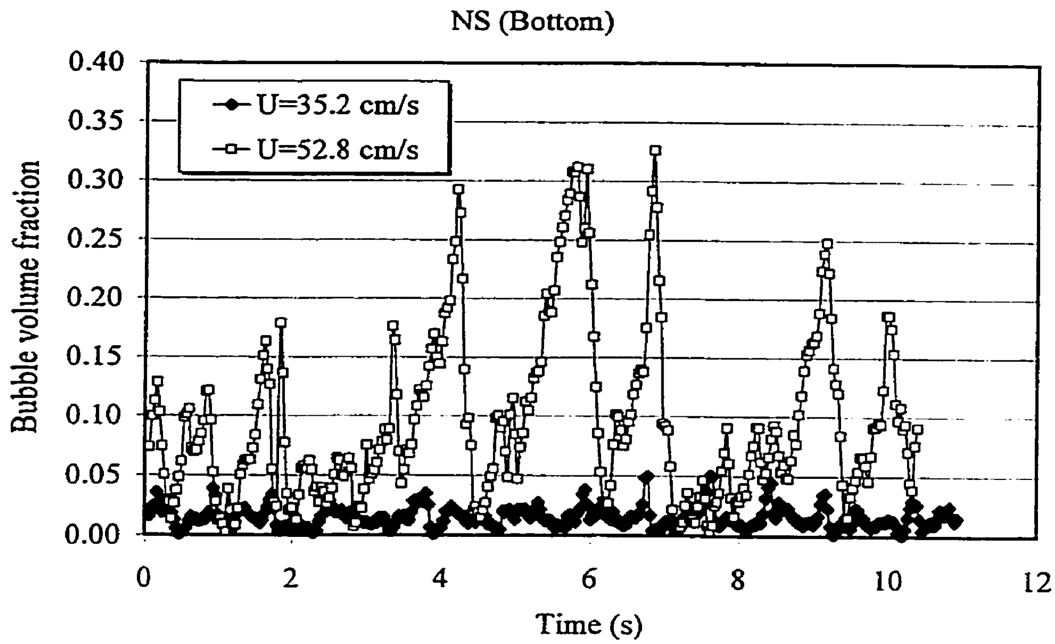

Figure C.4. Original results from image processing for bubble volume fraction for WPE-air system at three superficial gas velocities –top section of the bed

2. Sample calculations for Verification of the Image Processing Method

For NPE-air system, at U=21.6 cm/s, the following calculations were performed for verification of the image processing method.

Bubble volume fraction at bottom section of the bed = 0.0188

Bubble volume fraction at top section of the bed = 0.0616

The averaged bubble volume fraction = (0.0188+0.0616)/2 = 0.0402

The fluidized bed height below bursting region = 39 cm

The fluidized bed volume = $3.14 \times 5^2 \times 39 = 3061$ cm^3

The bubble volume in the bed: $V_{bubble} = 3061 \times 0.0402 = 123.1$ cm^3

At minimum fluidization velocity the fluidized bed height is 36.5 cm.

The bed expansion volume: $V_{bed} = 3.14 \times 5^2 \times 39 - 3.14 \times 5^2 \times 36.5 = 196.2$ cm^3

$V_{bubble} / V_{bed} = 0.63$

APPENDIX D

Bubble velocity is an important factor in determining the behaviors of a gas-solid fluidized bed. In the current research work, not only the vertical velocities but also the horizontal velocities of bubbles in fluidized beds were determined by using the image processing software developed in this study. The original image processing results for bubble vertical velocities are shown in Figures D.1 to D4 for NPE-air bottom section, NPE-air top section, WPE-air top section and NS-air bottom section, respectively. It may be noted that in these figures there are solid lines crossing the graphs from left to right. These solid lines show the results from bubble velocity correlation proposed by Kunii and Levenspiel (1991). The bubble diameter values used for the bubble velocity prediction were obtained from the bubble diameter correlation by Mori and Wen (1975) as shown in Equations (2.3) to (2.5).

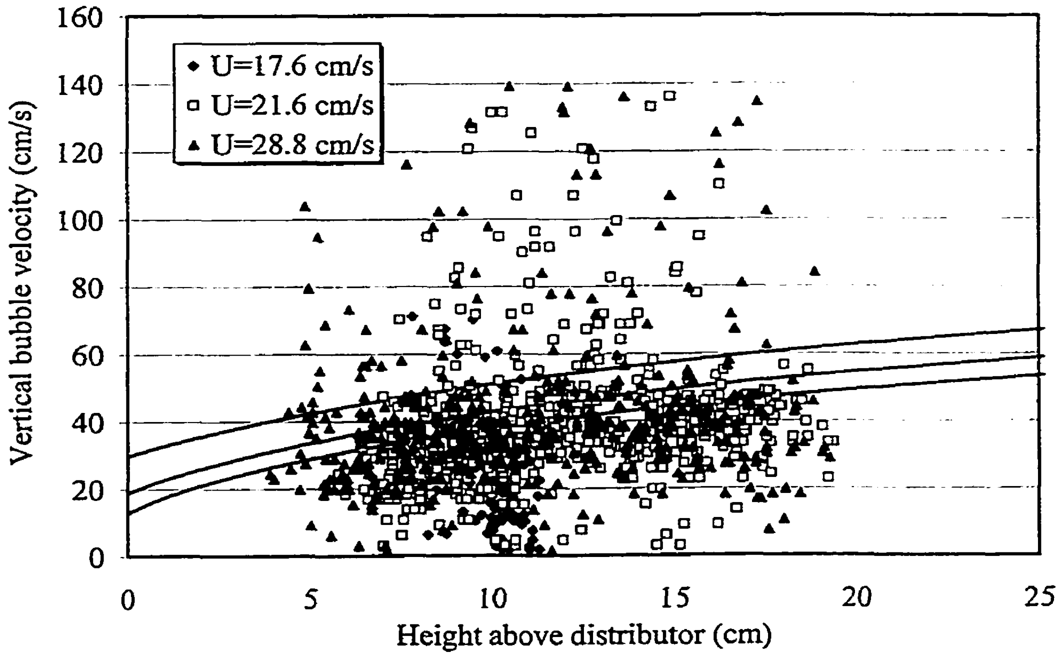

Figure D.1. Image processing results for bubble vertical velocity for NPE-air system at three superficial gas velocities-bottom section of the bed

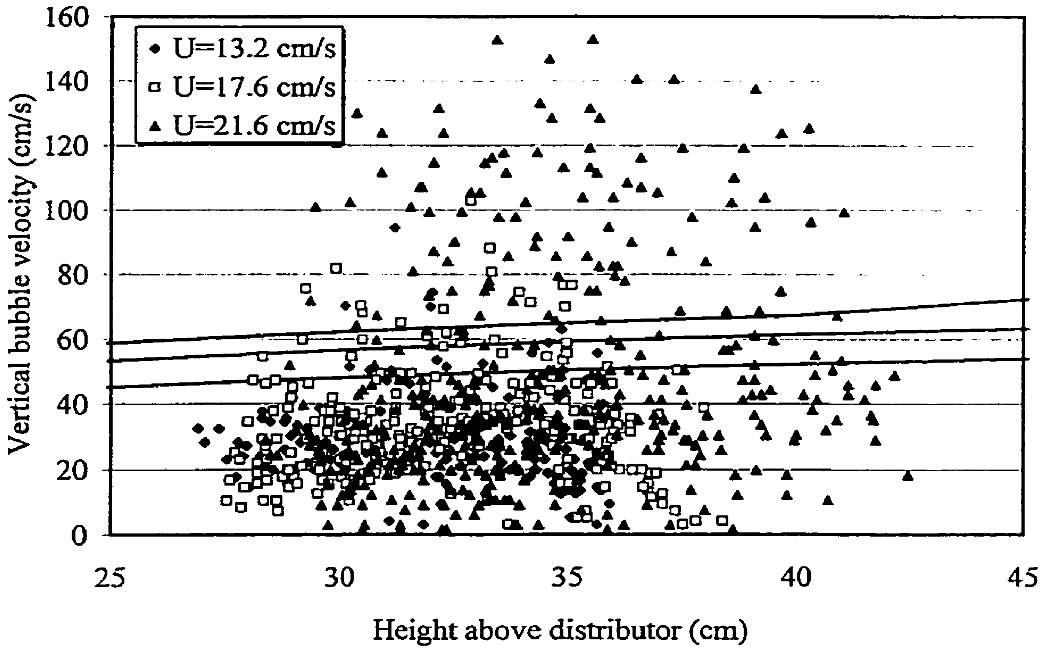

Figure D.2. Image processing results for bubble vertical velocity for NPE-air system at three superficial gas velocities-top section of the bed

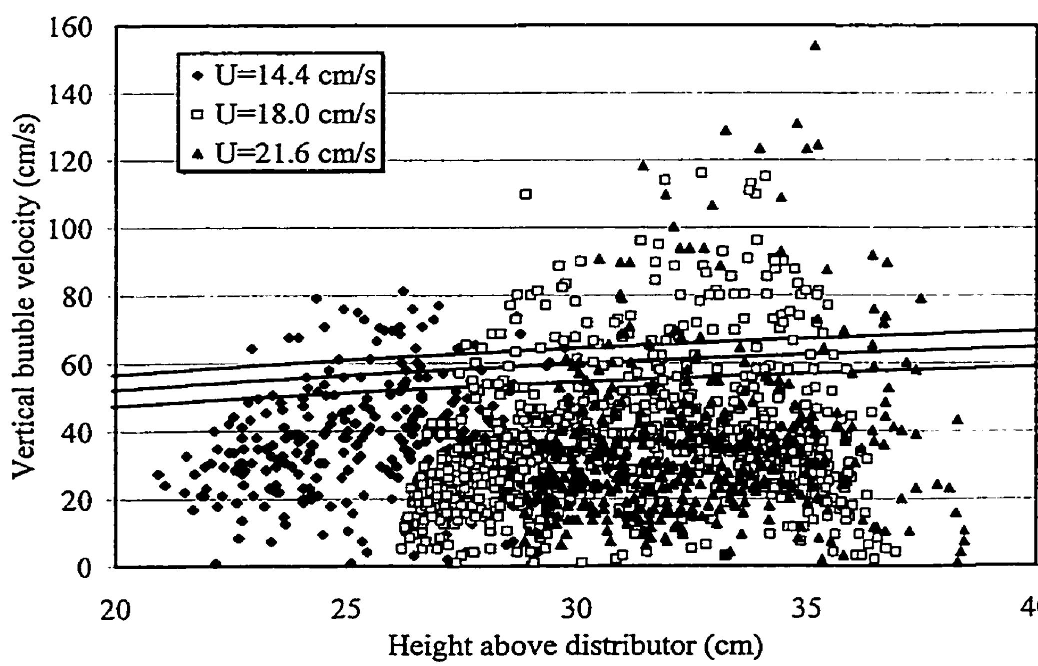

Figure D.3. Image processing results for bubble vertical velocity for WPE-air system at three superficial gas velocities –top section of the bed

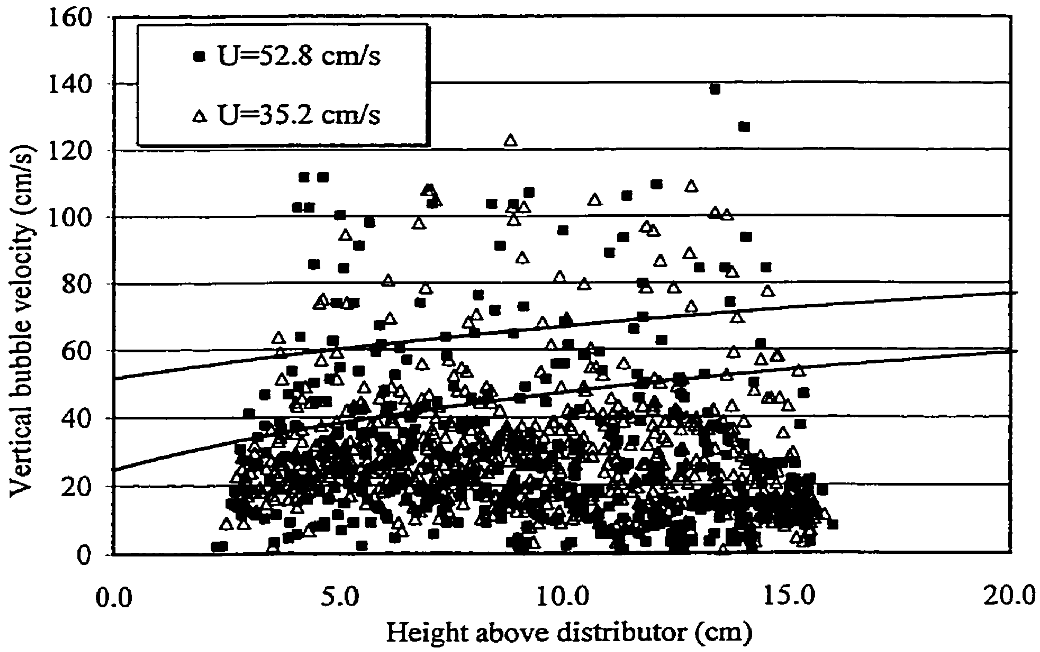

Figure D.4. Image processing results for bubble vertical velocity for NS-air system at two superficial gas velocities –bottom section of the bed